

Marquette University

e-Publications@Marquette

Master's Theses (2009 -)

Dissertations, Theses, and Professional
Projects

Synthesis and Evaluation of Small Molecule Inhibitors of Pyruvate Carboxylase

Daniel John Burkett
Marquette University

Follow this and additional works at: https://epublications.marquette.edu/theses_open



Part of the [Chemistry Commons](#)

Recommended Citation

Burkett, Daniel John, "Synthesis and Evaluation of Small Molecule Inhibitors of Pyruvate Carboxylase" (2020). *Master's Theses (2009 -)*. 604.
https://epublications.marquette.edu/theses_open/604

SYNTHESIS AND EVALUATION OF SMALL MOLECULE
INHIBITORS OF PYRUVATE CARBOXYLASE

by

Daniel John Burkett

A Thesis submitted to the Faculty of the Graduate School, Marquette University, in
Partial Fulfillment of the Requirements for the Degree of Master of Science.

Milwaukee, Wisconsin

August 2020

ABSTRACT
SYNTHESIS AND EVALUATION OF SMALL MOLECULE
INHIBITORS OF PYRUVATE CARBOXYLASE

Daniel John Burkett

Marquette University, 2020

Through structure-based drug design (SBDD), a series of small molecules have been synthesized and evaluated for inhibitory activity against the pyruvate carboxylase (PC) enzyme via two biological assays. The α -hydroxycinnamic acid scaffold was identified as the most privileged scaffold for inhibition of PC. Analogues of phenylpyruvic acid were generated and evaluated, leading to the discovery of inhibitors with single digit micromolar (μM) IC_{50} values. The most potent inhibitors identified were evaluated for inhibitory activity against other metalloproteins, and 2-hydroxy-3-(quinolone-2-yl)propenoic acid did not significantly inhibit human carbonic anhydrase II, matrix metalloproteinase-2, malate dehydrogenase, or lactate dehydrogenase. The small molecules presented in this work represent the most potent inhibitors of the pyruvate carboxylase enzyme to date.

ACKNOWLEDGEMENTS

Daniel John Burkett

Throughout my academic journey, I have been blessed with a myriad of support structures that have aided me in pursuing and completing my graduate degree. Pursuit of a graduate education has helped me discover my passion as an educator, and equipped me with the skills and experiences necessary to be an effective communicator of scientific ideas as I step beyond Marquette University.

I would like to thank the faculty and staff at Marquette University. Lori Callaghan, the Chemistry Department's administrative assistant, has been an essential resource in navigating many aspects of graduate student life as I've progressed through my years at Marquette. I also thank Dr. Sandra Lukaszewski-Rose, who has provided enormous support in my pursuing a teaching career, and who challenged me to deeply consider my approach to chemistry pedagogy.

To my committee and advisor, I am appreciative of the feedback that has strengthened the quality and meaning of my research. I especially want to thank Dr. Martin St. Maurice for being an essential resource in helping me navigate the biological aspects of my project. I thank my advisor, Dr. William Donaldson, for exercising patience with me as a graduate student, and acknowledging and supporting my goals.

I extend gratitude to the friends I've made in this program, especially Ricardo Rosas and Kristin Brandes, whose support was essential in my staying the course in pursuing this degree. I thank Brittney Wyatt, who was an essential partner in this project. I was fortunate to work with exceptional undergraduates both in the research laboratory and in a classroom laboratory setting, and for those experiences, I am grateful.

I have benefited from the support of a wonderful family. I thank all of my cousins, but especially Annie Geary and Jamie Burkett, who were on the receiving end of many phone calls in times of both stress and joy. My brothers, Adam and Dennis Burkett, provided endless support and encouragement throughout my educational journey. Finally, I thank my parents, John and Nancy Burkett, for encouraging my academic efforts, and offering their endless love and support, gently nudging me in the right direction in my times of greatest self-doubt. Without them, I certainly would not have made it thus far.

Finally, I dedicate this work to my grandparents, Don and Joan McGeehon, and Tom and Anne Burkett, who regrettably are no longer with us. Throughout my life, I was blessed with their unconditional love and support, and I strive to honor them every day.

TABLE OF CONTENTS

CHAPTER

I.	INTRODUCTION.....	1
1.1.	Project Summary.....	1
1.2.	The Citric Acid Cycle.....	2
1.3.	Structure and Function of Pyruvate Carboxylase.....	3
1.4.	Pyruvate Carboxylase Disease Association.....	7
1.4.A.	Pyruvate Carboxylase and Breast and Lung Cancer.....	8
1.4.B.	Pyruvate Carboxylase and Type 2 Diabetes.....	12
1.5.	Inhibitors of Pyruvate Carboxylase.....	15
1.5.A.	Inhibition via Interaction With Avidin.....	16
1.5.B.	Inhibition of the BC Domain.....	18
1.5.C.	Inhibition of the CT Domain.....	20
1.5.D.	Inhibition via the Allosteric Domain.....	25
1.5.E.	Structure Based Drug Design Rationale.....	27
II.	BIOLOGICAL EVALUATION.....	28
2.1.	Initial Screening of Compounds Via Colorimetric Assay.....	28
2.2.	Confirmation of Inhibitors via Coupled-Enzyme Assay.....	30
2.3.	Identification of Mode of Inhibition.....	32
2.4.	Metalloenzyme Assay Selectivity Panel.....	36

III.	IDENTIFICATION AND EVALUATION OF INHIBITOR SCAFFOLD.....	41
3.1	Attempts Targeting CT Domain.....	41
3.2	α -Hydroxycinnamic Acid Scaffold.....	45
3.3	Expansion of α -Hydroxycinnamic Acid Scaffold.....	58
3.3.A.	Synthesis of 3,3'-(1,4-Phenylene)bis[2-hydroxy-2-Propenoic acid].....	59
3.3.B.	Expansion via Heck Coupling.....	60
3.3.C.	Expansion via Suzuki Coupling.....	62
3.3.D.	Expansion via Sonogashira Reaction.....	64
3.4	Heteroaromatic Inhibitors.....	67
IV.	COMPUTATIONAL DOCKING AND ENZYME SELECTIVITY.....	71
4.1	Determination of Mode of Inhibition of Compound 19.....	71
4.2	Computational Docking of PC Inhibitors.....	72
4.3	Evaluation of PC Inhibitors Against Metalloenzyme Panel.....	76
V.	FUTURE DIRECTIONS.....	81
5.1	Exploration of Heteroaromatic α -Hydroxycinnamates.....	81
5.2	Further Utility of Sonogashira Reactions.....	82
5.3	Evaluation of Cell Permeability.....	84

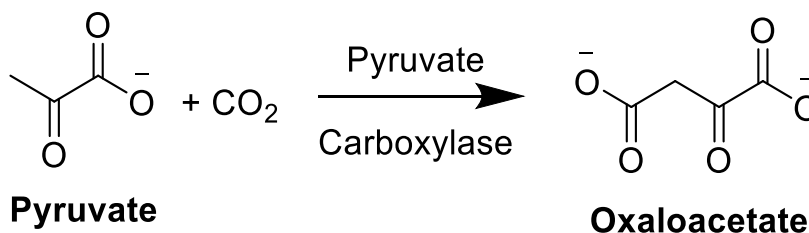
VI.	METHODS AND CHARACTERIZATION.....	87
6.1	Enzyme Inhibition Assays.....	87
6.1.A.	Screening Compounds for Inhibition Using Fast Violet B.....	88
6.1.B.	Measurement of OAA Formation With Malate Dehydrogenase.....	88
6.1.C.	Evaluation Against Human Carbonic Anhydrase (<i>hCAII</i>).....	89
6.1.D.	Evaluation Against Matrix Metalloproteinase-2 (MMP-2).....	90
6.2	Computational Docking.....	90
6.3	Chemistry.....	91
6.3.A.	General Experimental.....	92
VII.	REFERENCES.....	127

CHAPTER 1

Introduction

1.1 Project Summary

Pyruvate carboxylase is the major anaplerotic enzyme responsible for the catalytic conversion of pyruvate to oxaloacetate (OAA) in an array of organisms (Scheme 1.1).¹ Because of its reported link to a variety of diseases and infections including certain cancers², type 2 diabetes³, and listeriosis⁴ as a result of aberrant or essential expression of PC in cells, the development of small molecule inhibitors as chemical probes targeting PC in cells, the development of small molecule inhibitors as chemical probes targeting PC is desirable to allow for better characterization of PC's role in these diseases.



Scheme 1.1 Carboxylation of pyruvate to form oxaloacetate, catalyzed by pyruvate carboxylase.

In exploring an initial scaffold, the solution of a crystal structure showing 3-bromopyruvate, a known anti-cancer agent that targets multiple pathways, bound in the carboxyltransferase domain of PC showed the α -keto carboxylate moiety aligned analogously to pyruvate, the bona fide substrate.⁵ On the basis of this structure, more structurally complex α -keto acids were imagined as potential competitive inhibitors by excluding pyruvate from the CT domain active site.

Compounds tested for inhibition were either synthesized or obtained from commercially available sources. Initial screening of compounds were screened against *Staphylococcus aureus* PC (SaPC) via an optimized fixed-time assay⁶, and hits were confirmed in a coupled enzyme assay⁷. Because of their potential to interact with other metalloenzymes, potent inhibitors of PC were evaluated for activity against human carbonic anhydrase II (*hCAII*) and matrix metalloproteinase-2 (MMP-2)⁸ to evaluate selectivity for PC.

1.2 The Citric Acid Cycle

In the citric acid cycle (TCA), intermediates are generated for use in biosynthetic pathways leading to the production of glucose, fatty acids, and non-essential amino acids. As intermediates are removed from the TCA cycle in cataplerotic reactions, their replacement is achieved via anaplerosis by PC, the major anaplerotic enzyme.⁹ The major cataplerotic and anaplerotic pathways are illustrated in Figure 1.1.

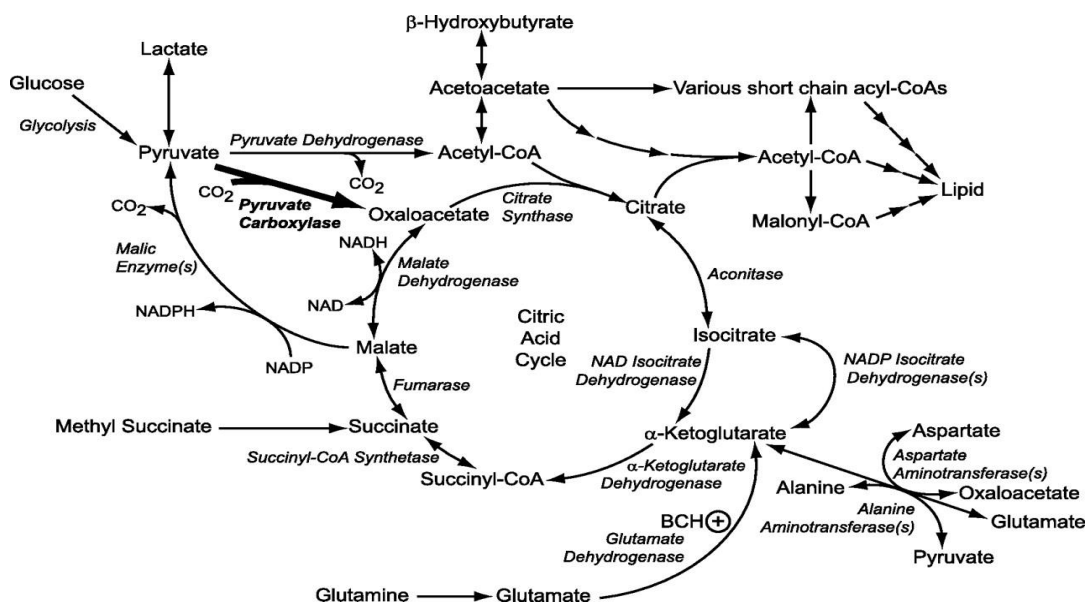


Figure 1.1 The major cataplerotic and anaplerotic reactions of the TCA cycle leading to gluconeogenesis and lipogenesis.¹⁰

As illustrated in Figure 1.1, the carboxylation of pyruvate to oxaloacetate is an integral anaplerotic process. As malate is jettisoned from the mitochondria en route to the generation of glucose (gluconeogenesis), or as citrate is consumed for the generation of fatty acids (lipogenesis), regeneration of oxaloacetate, facilitated by PC, is essential for sustained cellular function.¹⁰

1.3 Structure and Function of Pyruvate Carboxylase

Conversion of pyruvate to oxaloacetate employing endogenous bicarbonate by PC is dependent upon the presence of pyruvate, Mg^{2+} , and ATP.¹¹ This $MgATP$ -dependent carboxylation of pyruvate to generate OAA occurs in two distinct active sites of PC. These are the biotin carboxylation (BC) domain, in which a covalently linked

carboxybiotin cofactor is generated. The BC domain is conserved across all biotin dependent carboxylases.¹² This carboxybiotin cofactor ultimately transfers a carboxyl group to pyruvate bound in the carboxyltransferase (CT) domain, which is structurally unique to PC, found only in a few bacterial oxaloacetate decarboxylases apart from PC.¹³ Translocation of the covalently linked carboxybiotin cofactor from the BC domain to the CT domain by a biotin carboxyl carrier protein (BCCP) allows for decarboxylation of the carboxybiotin in the CT domain, followed by pyruvate's subsequent carboxylation, generating OAA.

Crystal structures of human, *Staphylococcus aureus*, and *rhizobium etli* PC (HsPC, SaPC, and RePC) show conservation of the aforementioned domains from organism to organism, but also rationalizes the necessity of the homotetrameric structure (Figure 1.2) for catalytic activity.¹⁴

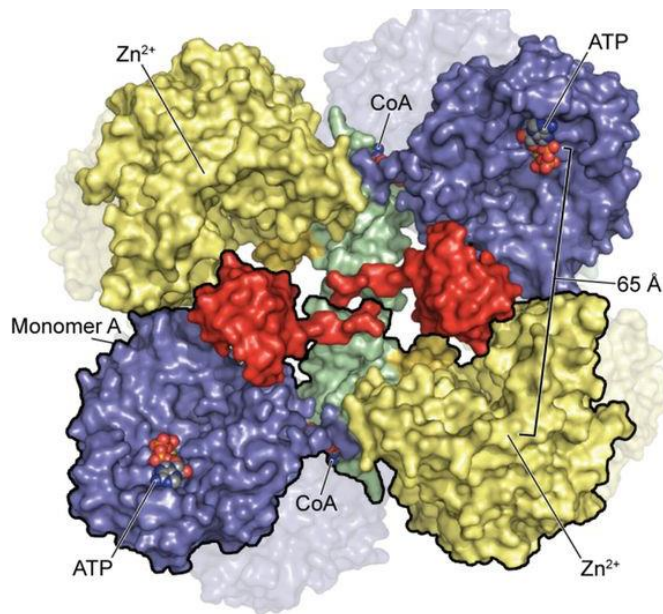
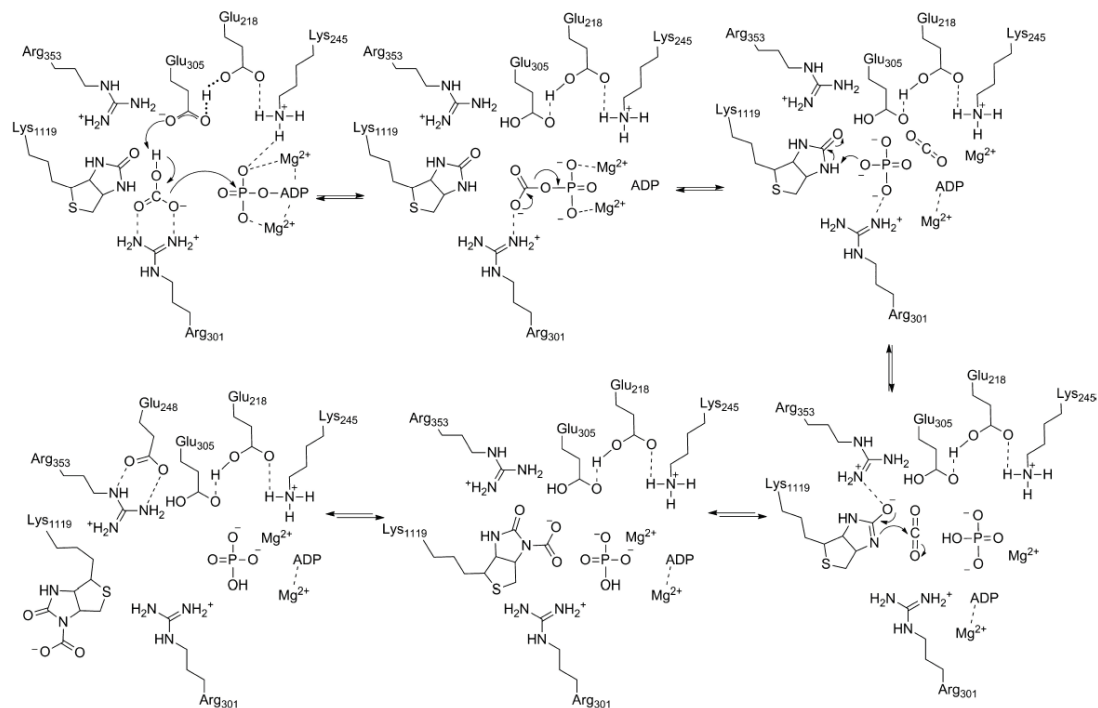


Figure 1.2 Homotetrameric structure of pyruvate carboxylase. The four essential domains of each monomer are the CT (yellow), BC (purple), BCCP (red), and central allosteric domain (green).¹

Eventual carboxylation of pyruvate begins in the BC domain. Biotin, covalently tethered via a lysine residue of the BCCP undergoes carboxylation by bicarbonate and ATP before being translocated to the CT domain. Of a contiguous monomer, the distance between BC and CT domains exceeds the length allowed for by the flexibility of the BCCP domain, which instead translocated the carboxybiotin cofactor to the CT domain of an opposing PC monomer, where carboxyl transfer to pyruvate will occur.¹⁵

Carboxylation of biotin in the BC domain is worthy of additional comment. The catalytic triad of Glu218, Lys245, and Glu305 (*RePC* numbering), serves to construct a hydrogen-bonding network between the MgATP and bicarbonate binding pockets in the BC domain active site (Scheme 1.2). Lys245 interacts with the γ -phosphate of MgATP, positioning the phosphate for nucleophilic attack by bicarbonate.¹

Necessary deprotonation of bicarbonate is performed by Glu305, which is basic enough to deprotonate bicarbonate due to hydrogen bond interactions with Glu218 serving to increase the pKa of Glu305.¹⁶ Deprotonation of bicarbonate by Glu305, followed by nucleophilic attack to generate the proposed carboxyphosphate intermediate, which decomposes to generate CO₂ and PO₄³⁻, ultimately deprotonating biotin at the N₁-position. The resulting biotin-enolate is partially stabilized by an arginine residue, and carboxylation occurs via nucleophilic attack on the CO₂ molecule by the biotin-enolate.



Scheme 1.2 Proposed mechanism of the carboxylation of the covalently-linked biotin cofactor in the BC domain of PC.¹⁶

Upon carboxylation of the tethered carboxybiotin cofactor, translocation to the CT domain of an opposing PC monomer occurs. In the CT domain, decarboxylation of the carboxybiotin cofactor is possible due to the stabilization of the resulting biotin enolate by Gln844, Ser885, and Lys886 (*SaPC* numbering). This stabilized biotin cofactor and the orientation of pyruvate is illustrated in Figure 1.3.¹⁷

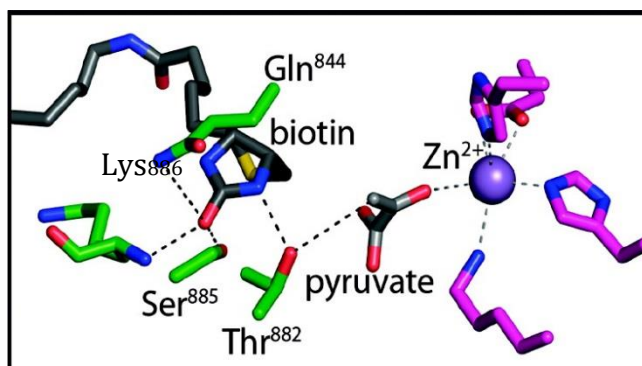
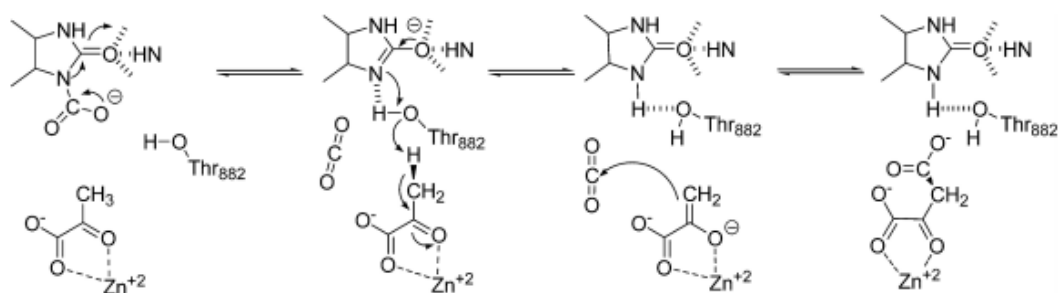


Figure 1.3 Stabilization of the biotin enolate in the CT domain occurs via hydrogen-bonding with Gln844, Ser885, and Lys886. Pyruvate binds in the CT domain active site with the enolate-oxygen oriented toward the metal ion.

Critically important is the Thr882 residue, which serves as a proton shuttle, whereby proton transfer to the biotin enolate occurs in concert with Thr882 deprotonating pyruvate to generate the requisite pyruvate enolate. The pyruvate enolate thus formed engages the liberated CO_2 molecule via nucleophilic attack, generating OAA as the product (Scheme 1.3).¹⁷



Scheme 1.3 Proposed mechanism for carboxylation of pyruvate in the CT domain active site. Central to this process is the highly conserved Thr882 residue, which serves as a proton shuttle facilitating a concerted proton transfer from pyruvate, generating the necessary pyruvate enolate intermediate, protonating the biotin enolate, regenerating biotin.

1.4 Pyruvate Carboxylase Disease Association

PC's aforementioned association to cancers, type 2 diabetes, and listeriosis demonstrates the value in developing inhibitors of the enzyme with the potential to serve as chemical probes. While PC's expression is linked to these diseases, effective inhibition of PC would allow for more complete elucidation of PC's role in these diseases.

1.4.A Pyruvate Carboxylase and Breast and Lung Cancer

Proliferating cells, such as cancer cells, are exploitative of the TCA cycle for sources of biosynthetic intermediates to allow for continued cell growth.¹⁸ As established, critical to the generation of TCA cycle intermediates is anaplerotic regeneration of OAA, a process fulfilled by PC. An alternative to PC-dependent anaplerosis is glutamine anaplerosis whereby glutamine undergoes glutaminolysis to ultimately produce OAA.¹⁹ In cancers, preference for PC-dependent anaplerosis or glutamine anaplerosis has been established and linked to aberrant PC expression.²⁰ Many breast cancers demonstrate a low dependence on PC anaplerosis²⁰⁻²¹ while a plurality of lung cancers demonstrate a high dependence on PC anaplerosis.^{22a-b} *In vivo* cultivation of lung cancer cells maintained the PC-dependent anaplerosis while *in vitro* cultivation shifts the dependence to glutamine anaplerosis.²⁰

This preference for PC-dependent versus glutamine anaplerosis is sensitive to changes in the cellular microenvironment. In the presence of glutamine anaplerosis inhibitors, PC expression is increased, and increased availability of pyruvate provides an alternative anaplerotic source of biosynthetically important intermediates, and the relative dependence on PC-dependent anaplerosis is exacerbated. Furthermore, inhibiting the

pyruvate micronutrient supply by dosing cells with the mitochondrial pyruvate carrier (MPC) inhibitor, UK-5099, which transports pyruvate to the mitochondria where PC then completes the conversion to OAA shifted preference for PC-dependent anaplerosis to glutamine anaplerosis.²³ These data are summarized in Figure 1.4.

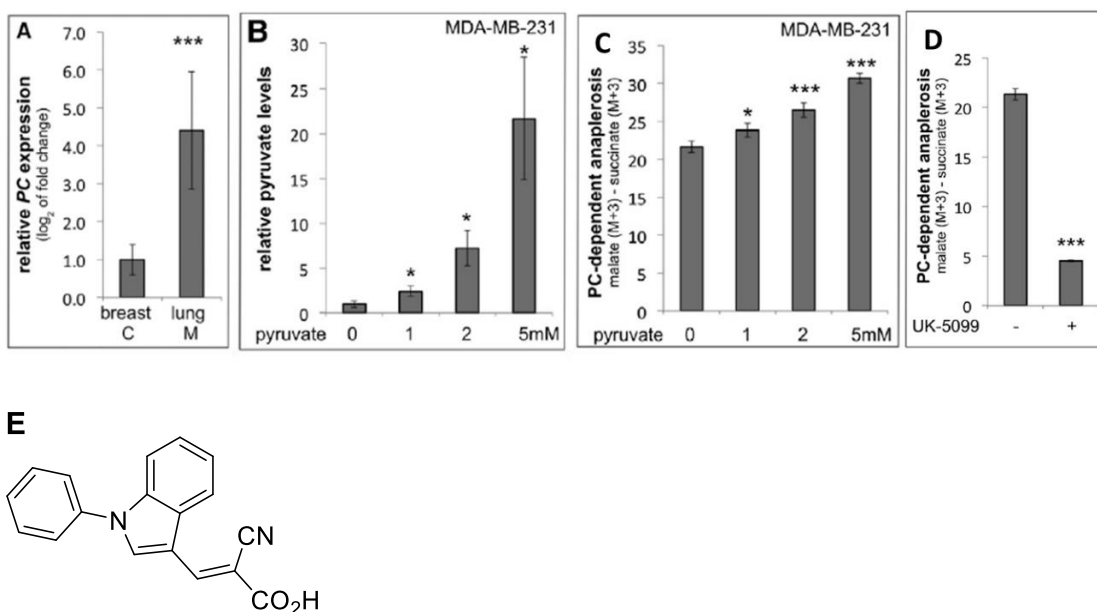


Figure 1.4 (A) Relative expression of PC in primary breast cancers (C) and lung metastases from 4T1 mice (n=7). (B) Pyruvate levels in MDA-MB-231 breast cancer cell lines cultured with increasing amounts of pyruvate in the nutrient microenvironment (n >3). (C) Relative PC-dependent anaplerosis in MDA-MB-231 breast cancer cell lines associated with increased concentrations of pyruvate in nutrient microenvironment (n >3). (D) Amount of PC-dependent anaplerosis in MDA-MB-231 breast cancer cell lines treated with (+) MPC inhibitor UK-5099 at a concentration of 10 μ M and without treatment. (-). (E) Structure of UK-5099.²³

This dependence of non-small cell lung cancers on PC-dependent anaplerosis is significant, and suppression of PC in these cell lines does not appear to allow for glutamine anaplerosis as an alternative, as cell growth is retarded with PC suppression,

owing to the disruption of biosynthesis of lipids, nucleotides, and the imbalance of glutathione metabolism.²¹

As stated, while many breast cancer cell lines are highly reliant on glutamine anaplerosis, MDA-MD-231 represents a highly motile breast cancer cell line that demonstrates PC anaplerotic dependence, at least when cultured *in vitro*. In comparison to normal breast tissue, PC is highly expressed in the MDA-MB-231 cell lines, but is much lower in less aggressive cell lines such as MCF-7 and SKBR3. Furthermore, as tumors from the MDA-MB-231 cell line grow, PC expression increases. While PC expression suppressed via silencing RNA still allowed growth of the MDA-MB-231 cell line at a 50% growth rate, migration and invasion ability of the cell line was markedly decreased.²⁴ This lower growth rate may be due to utilization of glutamine anaplerosis.

This relationship between PC expression, cell growth, migration and *in vitro* invasion of the MDA-MB-231 cell line, suggests that overexpression of PC is important to metastasis. While this connection is established, PC's role is still not fully understood.²⁵ Significantly, it has been shown that not only does overexpression of PC correlate to enhanced viability of breast cancer cell lines, but a strong correlation between expression of PC and improved migration ability of the cancer cell line exists, as demonstrated in Figure 1.5 below. It is well-established that migration of tumors to distal organs occurs via a multitude of biological steps, requiring substantial amounts of ATP. It is proposed that one consequence of suppression of PC expression thereby limits a cell's supply of OAA, ultimately resulting in reduced levels of ATP.²⁶

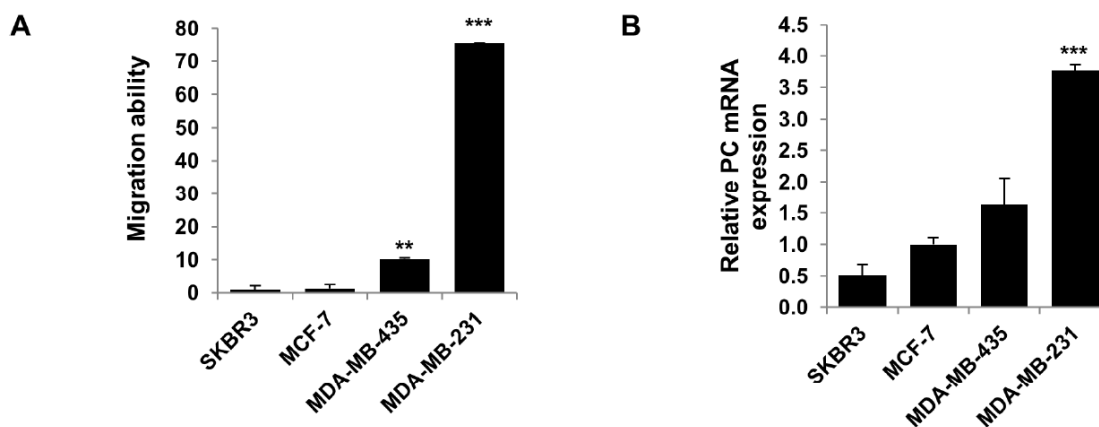


Figure 1.5 (A) Relative motilities of several breast cancer cell lines. MDA-MB-435 and MDA-MB-231, which both show dependence on PC anaplerosis when cultivated *in vitro* show higher motility than SKBR3 and MCF-7, which demonstrate glutamine-dependent anaplerosis. (B) Relative PC mRNA expression of the same four breast cancer cell lines.²⁴

Furthermore, the correlation between PC expression and the more aggressive phenotypes of breast cancer cell lines emphasizes the established association of increased expression of PC and larger tumor size. That upregulation of PC is connected to low survival rates indicates an *in vivo* significance of PC in metastatic breast cancer²⁷, despite the discrepancy in the higher observed PC-dependence for *in vitro* cultivated cell lines versus *in vivo* cell lines.²³

This study suppresses the expression of PC in MDA-MB-231 cell lines obtained from *in vitro* cultivation. As established, expression of PC is dependent on the microenvironment. Therefore, the results of this study might overinflate the impact of inhibition of PC in this breast cancer cell line, highlighting the impact *in vivo* inhibition of PC in this and other cell lines would have in elucidating PC's role in proliferation of breast cancer. Taken together, the more highly invasive breast cancer cell lines' exhibition of enhanced motility correlated to overexpression of PC and the adaptability of

cancer cell lines to transition from glutamine-dependent anaplerosis to PC-dependent anaplerosis, with the demonstrated reduced motility in PC-knockout samples demonstrates the importance of PC in breast cancer proliferation.

1.4.B Pyruvate Carboxylase and Type 2 Diabetes

Owing to predictions that by the year 2050, one in three Americans will suffer from type 2 diabetes demonstrates the necessity to understand its pathogenesis.²⁸ Essential to its pathogenesis is increased hepatic gluconeogenesis and fasting hyperglycemia.²⁹ Catalyzing the production of the first biosynthetic intermediate en route to gluconeogenesis, PC has been established as one of the four enzymes responsible for the regulation of hepatic gluconeogenesis¹¹, but is known to be upregulated in type 1 diabetic rodents³⁰ and obese Zucker Diabetic Fatty rats³¹.

In the absence of tissue-dependent molecular inhibitors of PC, antisense oligonucleotides (ASO) that selectively decrease expression of PC in liver tissue have been employed as PC suppressing agents.³² Two populations of rats were served either a regular chow-fed or a high fat fed diet, and treated with the ASOs, resulting in decreased PC expression by 70-90%. Importantly, the treated high fat fed rats were protected from weight gain, while the regular-chow fed rats maintained a healthy weight. Furthermore, fasting plasma glucose levels in the treated populations were reduced along with levels of fasting plasma insulin, indicating improved insulin-response with suppression of the expression of PC.³³

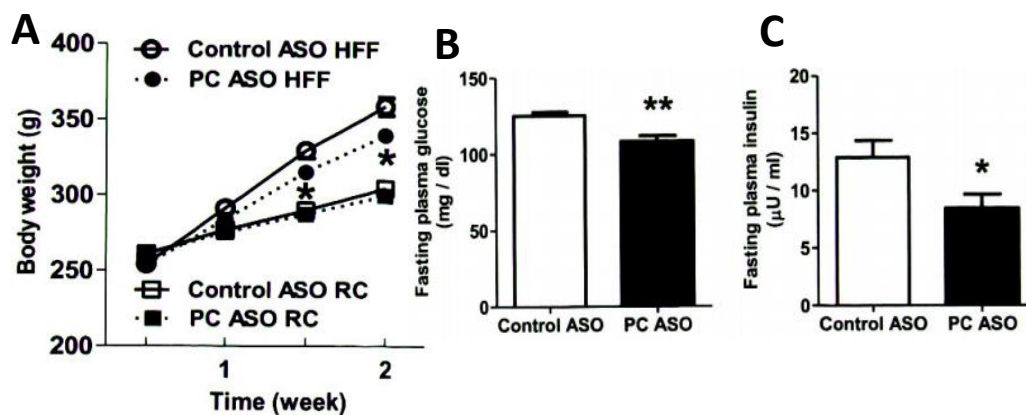


Figure 1.6 (A) Body weight (g) of control and PC-suppressed populations of high fat fed rats (circles) and regular chow-fed rats (squares). (B) Fasting plasma glucose levels of control population and PC-suppressed population. (C) Fasting plasma insulin levels of control population and PC-suppressed population.³⁴

This demonstrates tissue-selective reduction of the expression of PC in liver tissue is well-tolerated by these rat models. The reduction of weight gain observed in the PC-suppressed high fat fed rats is attributed to decreased glycerol synthesis in the liver, indicating PC's important role in *in vivo* glyceroneogenesis. In these models, suppression of PC was attributed to suppression of both gluconeogenesis and glyceroneogenesis, reduced fasting plasma glucose levels, reduced weight gain, and increased insulin sensitivity.

Insulin resistance and beta cell failure are two hallmarks of type 2 diabetes.³⁴ In response of insulin resistance, beta cell adaptation must occur, as maintenance of glucose levels requires increased secretion of insulin by and increased proliferation of beta cells.³⁵ Beta cell proliferation is dependent upon PC activity. Initial reports connecting PC's function to beta cell proliferation were either heavily reliant on correlation or use of the non-specific PC inhibitor phenylacetic acid.³⁶

In pancreatic beta cells, both PC and pyruvate dehydrogenase (PDH) are equally responsible for metabolism of glucose.³⁷ PC production inhibited by siRNA resulted in a drastic increase of PDH activity, allowing for continued viability of pancreatic beta cells. This increased level of PDH did not, however, compensate for PC's implied role in insulin secretion, as diminished levels of PC resulted in reduced insulin secretion. Further evidence validating PC's role in insulin secretion is given by mutated cells in which PC activity was increased twofold resulting in a 2.5-fold increase in insulin secretion. While reduction of PC was accommodated for in beta cell proliferation due to increased dependence of beta cells on PDH, increased PC activity resulted in increased cell proliferation, further highlighting PC's role in beta cell proliferation.³⁸

Stemming from its transcription being regulated by insulin³⁹, decreased levels of insulin correspond to an increase in the activity of PC⁴⁰ explaining the elevated plasma glucose levels in diabetic patients.⁴¹ Proposed as the rate-limiting enzyme in gluconeogenesis, inhibitory studies against PC have been conducted to ascertain its connection to type 2 diabetes.

Acetyl CoA, a product of fatty acid oxidation, serves as an allosteric activator to the PC enzyme. Inhibitors of this necessary long-chain fatty acid oxidation in turn inhibits the production of acetyl CoA, thereby leading to decreased PC activity, and ultimately inhibited gluconeogenesis.⁴² While this indirect inhibition of PC activity is suggestive of the enzyme's role in Type 2 diabetes, inhibitors acting directly on the enzyme itself promise to more strongly implicate PC's role in the disease. A series of phenylalkanoic acids were tested against PC in both *in vitro* and *in vivo* studies. Phenylacetic acid and phenylpropionic acid did act as competitive inhibitors against PC,

and were effective in reducing blood glucose levels in fasted non-diabetic rats. Despite the encouragement of a lack of toxicity in either *in vitro* or *in vivo* uses of phenylacetic acids, the concentrations used (2-4 mM) are too high to be pharmacologically relevant. Furthermore, the mechanism of action of phenylacetic acid showed that it was not the phenylacetic acid, but rather its conversion to phenylacetyl CoA, and the associated reduction of acetyl CoA that lead to the inhibition of PC.⁴³

These established relationships between abnormal PC activity and type 2 diabetes and cancers demonstrates the importance of understanding not only the structure, function, and mechanism of PC, but also underscores the potential of potent inhibitors of PC to not only further elucidate these relationships, but also to validate PC as a target for treatments of these diseases.

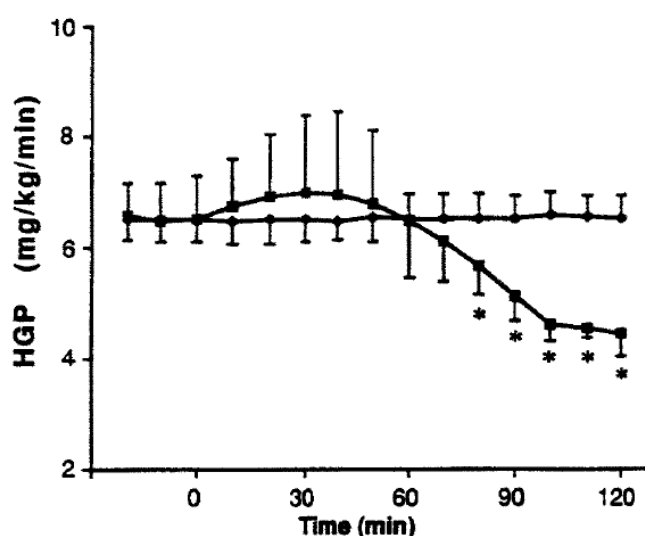


Figure 1.7 Effect of continuous infusion of phenylpropionic acid on hepatic glucose production (HGP) in fasted non-diabetic rats. Rats were treated with either saline (circles, flatter line) or 20 mg bolus of phenylpropionic acid, followed by a continuous infusion at a rate of 1 mg/minute (squares).⁴³

1.5 Inhibitors of Pyruvate Carboxylase

As mentioned in previous sections, prior studies developing and/or evaluating compounds for inhibitory activity against PC have been undertaken. While the following examples are not exhaustive of all compounds that have been studied as PC inhibitors, they are representative of the primary modes of action that were studied prior to the compounds described in the following chapters.

1.5.A. Inhibition via Interaction With Avidin

Avidin is a tetrameric protein bearing one biotin-binding site per monomer, binding biotin with a K_D with an order of magnitude of 10^{-15} M.⁴⁴ This high affinity for biotin results in Avidin's ability to act as a highly potent inhibitor of biotin-dependent enzymes, leading to its use to probe PC's mechanism of action.⁴⁵ The inhibition of PC could be monitored by a coupled enzyme assay. The initial rates of malate dehydrogenase (MDH) conversion of OAA to malate could be monitored by the loss in absorption due to NADH, which is consumed in this conversion. Since the OAA is produced by carboxylation of pyruvate via PC, the initial rate of MDH is correlated to the activity of PC. Use of this assay showed that avidin inhibition of PC is due to avidin's binding to PC.⁴⁶

Biotin, in biotinylated PC, can exist in the active site of the CT domain, a pocket outside of the CT domain, or the active site of the BC domain.⁴⁷ Compared to free biotin, avidin's affinity for biotin covalently linked to PC is significantly diminished, with a dissociation constant of the avidin-PC complex about 160 times greater than that of

avidin with free biotin⁴⁸, most likely owing to the added steric hindrance of the tethered biotin.

Avidin-induced inhibition of PC increases by a factor of eight when the allosteric activator acetyl CoA is limited to concentrations from 10-200 μM , as this activating effect induces a conformational change in PC, increasing the exposure of tethered biotin to avidin. Increasing concentrations beyond 200 μM had adverse effects on avidin's inhibition of PC, owing to a non-productive occupation of the nucleotide binding site, protecting against binding of avidin.⁴⁹

Stoichiometry of inhibition by avidin is one-to-one, avidin to PC. This stoichiometry is achieved by avidin's ability to adjoin two separate PC tetramers, ultimately forming hetero-oligomers, illustrated in Figure 1.8, confirmed by studies dosing PC obtained from chicken liver⁵⁰ and yeast⁵¹, demonstrating one face of avidin binding two biotin molecules on an adjoined tetramer of PC, with the opposite face of avidin binding another two molecules of biotin on another PC tetramer. These hetero-oligomers are stabilized by the presence of acetyl CoA.⁵²



Figure 1.8 Model illustrating the hetero-oligomers of avidin (grey cubes) and PC (shown in white).⁵⁰

Avidin inhibition served an important historic role in understanding biotin's role of the PC mechanism. These studies were the first to lead to an understanding of conformational changes induced by acetyl CoA, further explaining its activating effect. Prior to X-ray crystal structure determination, these studies divulged the possible position of biotin within PC, and provided evidence for the physical translocation of biotin via the BCCP.⁵³

1.5.B. Inhibition of the BC Domain

The hallmark reaction of PC's BC domain, the ATP-dependent carboxylation of biotin by bicarbonate, occurs in all biotin-dependent carboxylases except transcarboxylase.⁵⁴ Evidence supporting the proposed carboxyphosphate intermediate shown in Scheme 1.2 included the report of phosphonoacetic acid, which replaces the labile C-O-P linkage of the carboxyphosphate with a more stable C-CH₂-P linkage, as a noncompetitive inhibitor with respect to Mg-ATP with a K_i of 0.5 mM.⁵⁵ The presence of phosphonoacetic acid, shown to bind to PC, inhibited the conversion of ADP into ATP, and is therefore classified as an inhibitor of the BC domain reaction, as ATP was shown to be essential to the carboxylation of biotin.

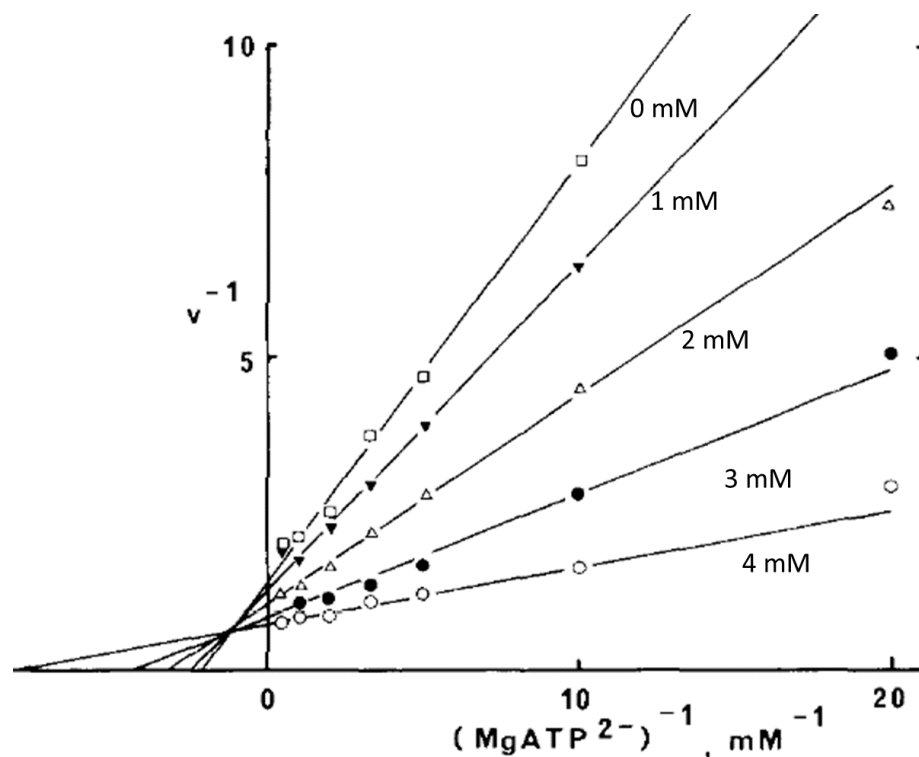


Figure 1.9 Reciprocal velocity of production of MgATP^{2-} versus reciprocal concentration of MgATP^{2-} in PC in the presence of phosphonoacetic acid from 0-4 mM. Concentrations of phosphonoacetic acid are shown under the line of each plot.⁵⁵

While phosphonoacetic acid has historical significance in elucidating PC's overall mechanism, its usefulness as an inhibitor is limited due to its targeting of the highly conserved BC domain, inhibiting a reaction common among all biotin-dependent carboxylases, except transcarboxylase, likely indicating poor selectivity.

The BC domain of PC is dependent on the nucleotide substrate MgATP . Several other nucleotides, MgGTP , MgUTP , MgCTP , MgTTP , and MgITP , with known affinities for PC⁵⁶ have been reported as competitive inhibitors with K_i values ranging from 0.7-0.9 mM.⁵⁷ The study of these nucleotides for their inhibitory activity was essential in understanding the binding mode of ATP in the BC domain active site, ultimately pointing to the importance of the adenosine moiety. Furthermore, occupation of the nucleotide-

binding site did not appear to influence the reactivity of carboxybiotin with pyruvate in the CT domain active site.

1.5.C. Inhibition of the CT Domain

The CT domain active site, home to the pyruvate-binding pocket, a biotin-binding pocket, and a metal ion has garnered attention as a potential site for competitive inhibition. Crystal structures of pyruvate analogues bound in the CT domain have been essential in understanding the arrangement of the active site wherein the enol-pyruvate nucleophilically attacks the liberated CO₂ molecule provided by the tethered carboxybiotin cofactor.

Oxamate, a structural analog of pyruvate, a known inhibitor of lactate dehydrogenase⁵⁸, also has been shown to trigger the movement of tethered carboxybiotin to the CT domain.⁵⁹ Oxamate was reported as a noncompetitive inhibitor with respect to pyruvate with a K_i of 1.6 mM.⁶⁰ Data from pulsed NMR experiments, provided evidence of the displacement of water molecules coordinated to the metal center in the presence of oxamate, suggesting direct coordination of oxamate to the metal center.⁶¹ This binding mode would suggest competitive inhibition with respect to pyruvate, leading to a hypothesis that oxamate's induction of transfer of biotin from the BC domain to the CT domain was fast relative to the carboxylation of the biotin cofactor, preventing exposure of enolpyruvate to a CO₂ molecule requisite of the carboxylated biotin cofactor.

Oxamate's inhibitory properties have been used to probe the physiological impact of PC inhibition. In addition to reduced glucose levels in isolated hepatocytes, all metabolites downstream from pyruvate, but not lactate, were observed at diminished

concentrations indicating the inhibition of gluconeogenesis was, in part, due to inhibition of PC, and ruling out inhibition of lactate dehydrogenase.⁶² Because of the implication of pyruvate carboxylation in the inhibition of gluconeogenesis, studies were directed toward mitochondria isolated from rat liver. While these studies showed inhibition of PC, and of pyruvate transport across the mitochondrial membrane, gluconeogenesis was not inhibited, suggesting pyruvate carboxylation is not rate-determining for gluconeogenesis. Exhibiting mixed-type inhibition, this study showed that isolated mitochondrial inhibition was a product of noncompetitive inhibition of PC, and competitive inhibition of the pyruvate translocator protein responsible for shuttle of pyruvate across the mitochondrial membrane.⁶³

Additionally, oxalate is reported as a non-competitive inhibitor with respect to pyruvate with reported K_i values of 70 μM (yeast)⁶⁴, 50-130 μM (rat liver)⁵⁷, and 12 μM (chicken liver)⁶⁰. Oxalate is competitive with respect to oxaloacetate (in the reverse reaction), with a dissociation constant of 8.9 μM for the metal ionic center of PC in chicken liver.⁶¹ At physiological pH, each of the two carboxyl groups of oxalate will be deprotonated, and is expected to behave as a metal chelator. In the crystal structure of oxalate crystallized in truncated *RePC* (absent the BC and BCCP domains), the distance between the metal ion in the CT domain active site and oxalate is 4.5 Å, showing interaction instead with a bridging water molecule 2.3 Å from the cationic metal ion. The carboxyl groups of oxalate are positioned such that a salt bridge is formed with the guanidinium side-chain of Arg621, and hydrogen-bonding interactions are formed with Arg548 and Gln552⁵, which are essential for catalysis in *RePC*.⁶⁴ This binding mode of oxalate is analogous to both oxamate and pyruvate (Figure 1.10).

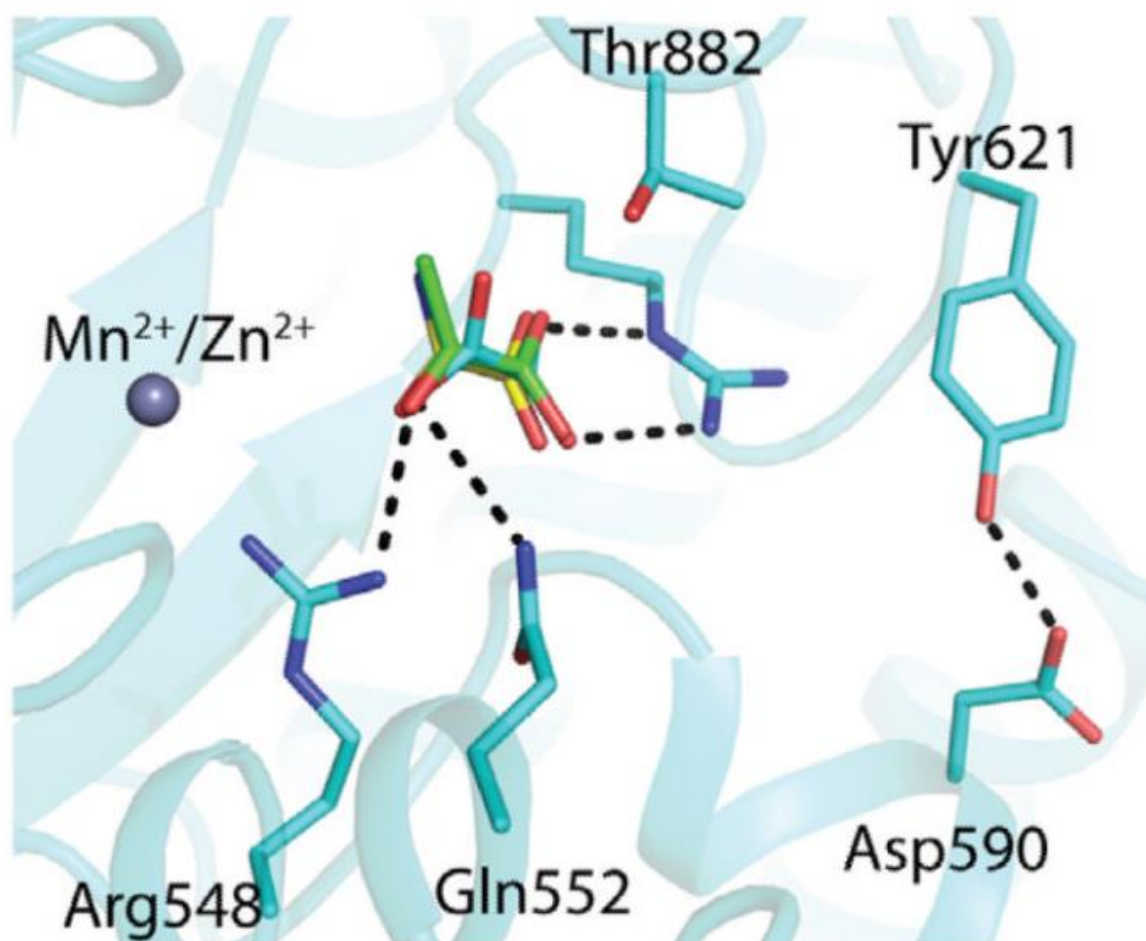


Figure 1.10 Structural overlay of the binding modes of oxalate (cyan), oxamate (yellow), and pyruvate (green). Rather than the expected metal-chelation of oxalate, a critical salt bridge is formed with Arg621, and hydrogen-bonding occurs with the catalytically-relevant residues Arg548 and Gln552. Structures obtained from crystallization in truncated *RePC* (absent the BC and BCCP domains).⁵

Oxalate is an effective metal chelator. It is surprising, then, that the crystal structure of oxalate bound in the truncated PC demonstrates a total lack of bidentate binding to the metal ion of the active site. This suggests that rather than stabilization of the requisite enolpyruvate intermediate through interaction with the metal center, the building negative charge is stabilized via a salt bridge with Arg621, and interactions with Arg658 and Gln552. This mode of stabilization allows C3 of pyruvate to position itself

such that proton transfer can occur with Thr882, supporting the proton shuttle mechanism discussed earlier.⁵

Leading to the inspiration for the current study, derivatives of pyruvate, and their associated crystal structures indicating binding in the CT domain active site with suggested direct coordination to the metal center, were shown to be inhibitors of the carboxyl transfer reaction.

In addition to the oxalate, crystal structures of pyruvate derivatives 3-hydroxypyruvate and 3-bromopyruvate, which not only are structural mimics of oxaloacetate, but are also inhibitors of the CT domain reaction.⁶⁶

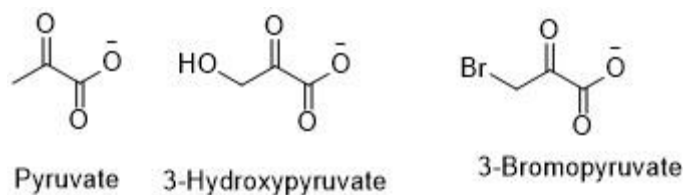


Figure 1.11 Structure of pyruvate and pyruvate derivatives 3-hydroxypyruvate and 3-bromopyruvate.

3-Hydroxypyruvate is a non-competitive inhibitor with respect to MgATP, bicarbonate, and pyruvate, with K_i values ranging from 5.4-71 mM. Analogously to pyruvate, the carboxyl moiety of 3-hydroxypyruvate forms a salt bridge with Arg 621, with hydrogen bonding interactions demonstrated between Arg548, Gln552 and the C2 carbonyl. Consistent with the binding modes observed of pyruvate, oxamate, and oxalate, 3-hydroxypyruvate does not establish bidentate coordination with the metal ion, and

binding of 3-hydroxypyruvate results in the closed conformation of the CT domain active site.⁵

Halogenation of the C3 position of pyruvate generates inhibitors that are competitive with respect to pyruvate, such as 3-fluoropyruvate with a K_i of 0.17 mM⁶⁰, and both 3-fluoropyruvate and 3-chloropyruvate inhibit gluconeogenesis in rat liver via modulation of PC activity.⁶⁷

While 3-bromopyruvate is a known anti-cancer agent, with an IC_{50} against PC of 280 μ M, it is known to target an array of metabolic targets⁶⁶, and has also been described as an antifungal agent⁶⁸, indicating low selectivity against the PC enzyme. Based on the observed crystal structure in the same truncated *RePC* described above, 3-bromopyruvate binds analogously to 3-hydroxypyruvate with a salt bridge involving the carboxyl moiety, and the bromide oriented toward the critically important Thr882 residue, just as the 3-hydroxyl moiety of 3-hydroxypyruvate. Interestingly, the bromide displaced a water molecule usually found coordinated to the metal center, and shows direct interaction with the metal ion, with a distance of 2.3 Å, possibly providing rationale for the relative potency of the halogenated pyruvate derivatives.⁵

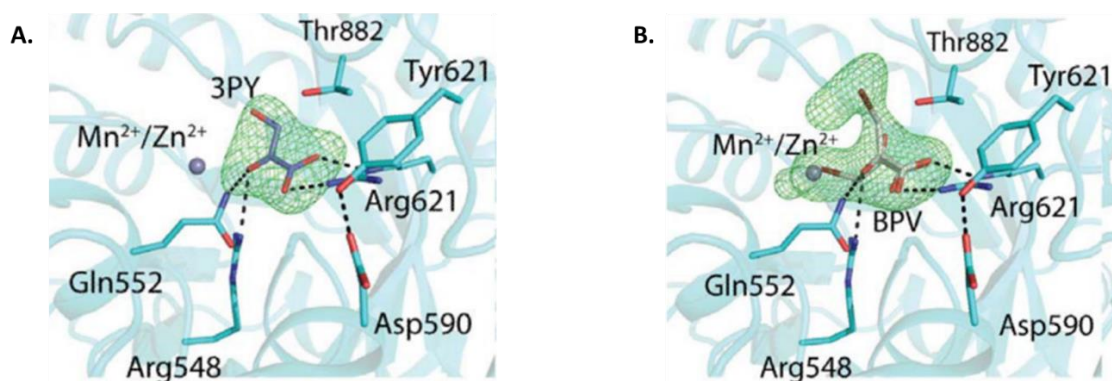


Figure 1.12 A) Binding of 3-hydroxypyruvate (3PY) in CT domain active site of truncated *RePC*. B) Binding of 3-bromopyruvate (BPV) in CT domain active site of truncated *RePC*.⁵

While inhibition due to 3-hydroxypyruvate and 3-bromopyruvate binding the CT domain active site of PC is modest, these simple molecules provide examples of the attractive features of the CT domain active site for designing small molecule inhibitors, with both compounds taking advantage of the well-defined active site via hydrogen bonding and salt bridge interactions, and the implied coordination to the metal center of the halogenated 3-bromopyruvate.

1.5.D Inhibition via the Allosteric Domain

Interactions with the allosteric domain have also shown viability as a mode for inhibition. In PC isolated from microbial and fungal sources, aspartate serves as an allosteric inhibitor⁶⁹, while PC from vertebrate sources is inhibited allosterically by glutamate.⁷⁰

In PC obtained from fungal sources, L-aspartate demonstrates competitive inhibition with an IC₅₀ of 0.6 mM with respect to the allosteric activator acetyl CoA and is a non-competitive inhibitor with respect to MgATP and pyruvate, supporting the

presence of a binding site in the enzyme's allosteric domain.⁷¹ Despite a lack of an activating effect in bacterial PC by acetyl CoA⁷² L-aspartate still demonstrates inhibitory activity against PC from these sources. While the binding site for L-aspartate has yet to be deduced crystallographically, it is proposed to be proximal to the acetyl CoA allosteric binding site. While L-aspartate is described as an inhibitor, the inhibitory concentrations are relatively high, ranging from 5 to 10 mM. Despite these high requisite concentrations of L-aspartate, it has been characterized as a physiologically relevant inhibitor of PC.⁷³

L-glutamate is a non-classical, non-competitive inhibitor with respect to acetyl CoA with a K_i of 3.8 mM against chicken liver PC and 4.7 mM against rat liver PC. Glutamate is proposed to serve as a negative feedback regulator for regulation of PC activity in these vertebrate sources.⁷⁴ Glutamate is a competitive inhibitor with respect to pyruvate, non-competitive with respect to bicarbonate, and uncompetitive with respect to MgATP.⁷⁰

While aspartate and glutamate provide examples of allosteric PC inhibition, α -ketoglutarate shows allosteric PC inhibition across a much more diverse array of sources, but still has its limitations. Several studies have reported the inhibitory activity of α -ketoglutarate via binding to an allosteric site distinct from that reported for aspartate.⁷⁰ With an apparent K_i of 3 mM in chicken liver, an example of a source of PC with a distinct allosteric binding site for α -ketoglutarate, inhibition by this mode is insensitive to reagents that eliminate acetyl CoA activation.⁷⁰ The presence of three distinct allosteric binding sites in chicken liver PC for acetyl CoA, glutamate, and α -ketoglutarate is proposed to allow for physiological regulatory control of PC activity in the mitochondria through a response to physiological ratios of these three metabolites.⁷⁵

1.5.E. Structure Based Drug Design Rationale

Taken together, these prior examples of inhibition of PC from a variety of modes including protein-protein interaction, binding of a small molecule in the BC or CT domains, or allosteric inhibition provide important insight into the mechanism of action of the PC enzyme, and underscore potential strategies to explore for inhibition of the enzyme. While the previously described inhibitors have served important roles in understanding the structure and function of the various active sites of PC, the relevant inhibitory concentrations of these inhibitors limit their usefulness as chemical probes. The relatively high concentrations required of the allosteric inhibitors raise the possibility of interference in any number of biosynthetic pathways, while the commonalities of the BC domain amongst biotin-dependent enzymes increase the likelihood of off-target effects, despite the well-defined binding pockets that lend the BC domain to structure based design of inhibitors. While the halogenated pyruvates are the most potent inhibitors discussed thus far, their promiscuous binding to metabolic enzymes limits their effectiveness.

Still, despite the limitations of the halogenated pyruvates, the crystal structure of 3-bromopyruvate and 3-hydroxypyruvate help to illustrate the potential of a potent PC inhibitor that binds in the CT domain. With a metal ion and well-defined binding sites for pyruvate and biotin paired with the uniqueness of the CT domain to PC, designing analogues incorporating the pyruvate motif to bind in the CT domain is an attractive strategy for structure based drug design.

Throughout this dissertation, strategies to evaluate and confirm inhibitory activity of small molecules against PC, and their evaluation against other biologically relevant

metalloenzymes to gauge selectivity will be described. Synthetic methods to generate the most potent small molecule inhibitors of PC to date will be described, and computational docking of these inhibitors to rationalize their potency will be presented.

CHAPTER 2

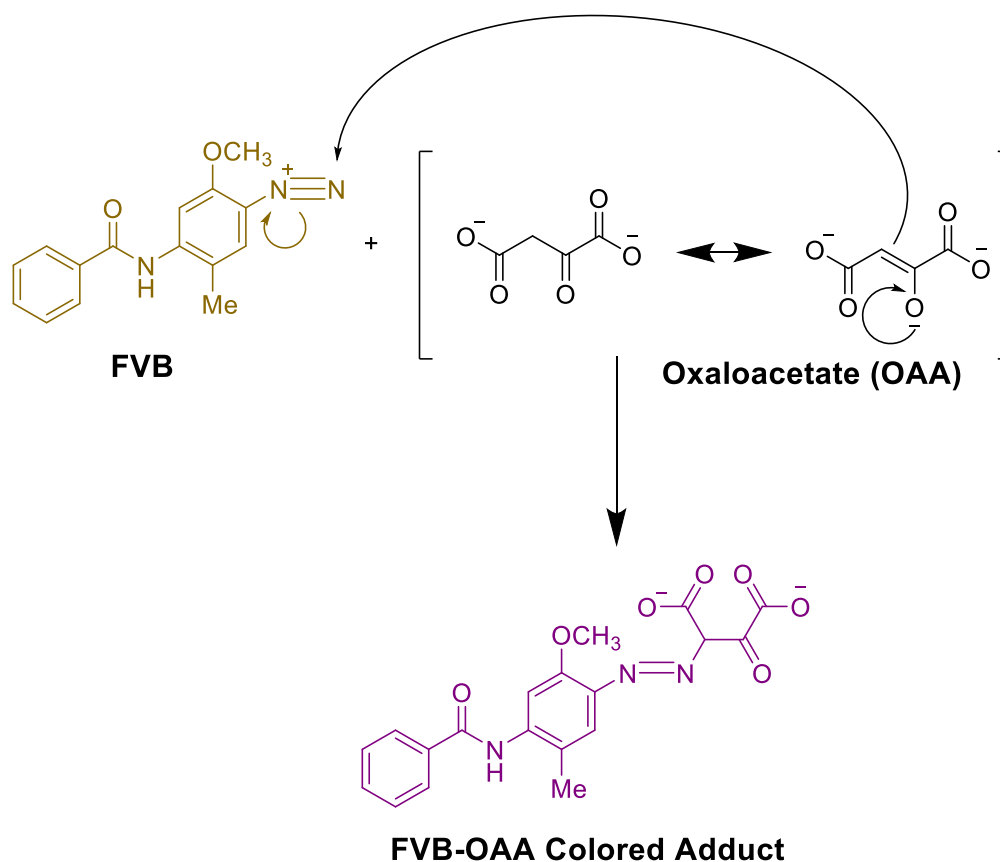
Biological Evaluation

2.1 Initial Screening of Compounds Via Colorimetric Assay

Keeping the goals outlined in the first chapter in mind, human PC represents the ideal target for the evaluation of small molecules as inhibitors of the PC enzyme.

Acquiring full-length recombinant human PC, however, is a difficult challenge⁴⁷, and at this time is not suitable for use in an initial screen of potential inhibitors. Alternatively, *Staphylococcus aureus* PC (*SaPC*) is used in an optimized fixed-time assay⁶ that has been employed in this project as the initial screening assay.

Developed to be amenable as a high throughput screen for large libraries of compounds, the initial screening assay is optimized to detect the colored adduct that forms in the reaction of oxaloacetate with Fast Violet B (FVB), a diazonium salt (Scheme 2.1). Named for the colored adduct that forms, this assay is referred to as the FVB assay. In the assay, a negative control for inhibition is conducted by introducing pyruvate to *SaPC*. For a positive control for inhibition, *SaPC* is rendered inactive by initial introduction of EDTA, which sequesters the requisite Mg^{2+} ions from the BC domain active site, preventing the forward conversion of pyruvate to OAA from occurring⁷⁶. A dose-dependent response curve, then is generated by varying the dose of potential inhibitors in other wells, and measuring the absorbance at 530 nm, λ_{max} of the OAA-FVB colored adduct. Negative control wells represent the absorbance observed corresponding to the uninhibited PC reaction in the time frame, while positive control wells give the baseline measurement for complete inhibition.



Scheme 2.1 Mechanism of the formation of the FVB-OAA colored adduct, the formation of which is measured in the FVB assay to determine inhibitory activity of small molecules.

In all wells for a given FVB assay, once the solution of assay buffer containing substrates is added, the reaction is allowed to proceed for at least 2 hours, and the assay has been validated for reactions of up to 5 hours. At the conclusion of the reaction timeframe, all wells are quenched with EDTA, effectively stopping the reaction as described above. Finally, the FVB salt is added, and wells are incubated for one hour in the presence of the salt before absorbance values are measured. An example of a dose-dependent response curve obtained from the FVB assay is given below in Figure 2.1.

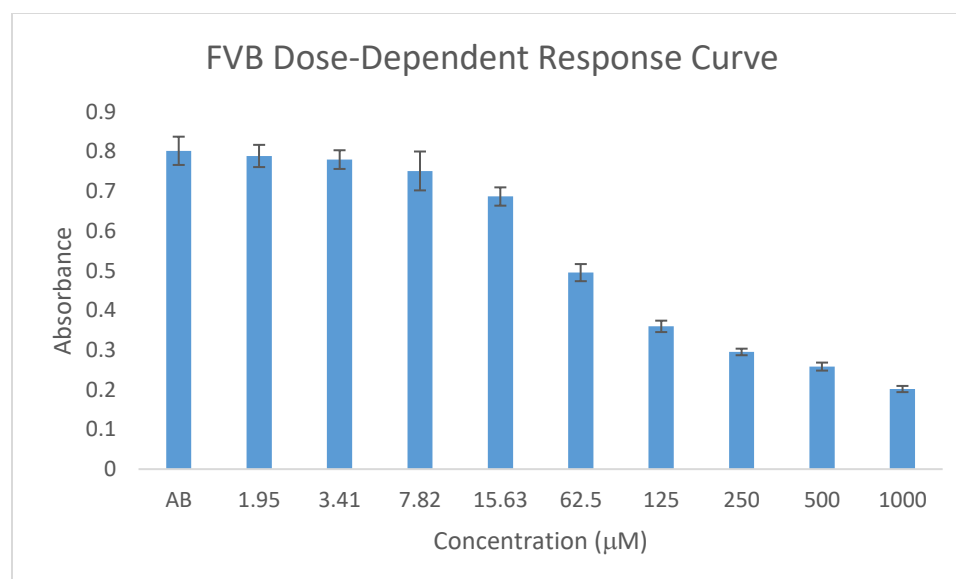


Figure 2.1 Representative dose-dependent response curve for a small molecule inhibitor of pyruvate carboxylase. The first column labeled AB represents the uninhibited forward reaction of PC.

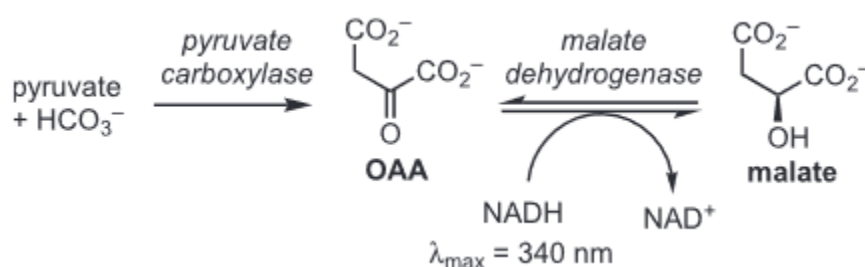
It is possible that small molecules tested in this assay could inhibit the formation of the FVB-OAA colored adduct rather than inhibiting the forward reaction of PC itself. To test for this, additional control wells are used in which OAA and a set concentration of the small molecule in question are incubated for the same length of time as the other test wells, then incubated with a solution of the FVB, and compared against wells that contain only OAA and the FVB salt. If the absorbance values obtained in these two cases are consistent, it is reasonable to conclude that any inhibitory activity observed is due to inhibition of the enzymatic reaction itself rather than inhibition of the formation of the FVB-OAA colored adduct.

2.2 Confirmation of Inhibitors via Coupled-Enzyme Assay

As a secondary assay to confirm inhibition identified in the FVB assay, a coupled enzyme assay, termed the MDH assay due to the additional enzyme present, was

employed. Malate dehydrogenase (MDH) converts OAA to malate, oxidizing NADH to NAD⁺ (Scheme 2.2). This is a kinetic assay, in which initial rates of this oxidation are recorded by monitoring the decrease in absorbance due to NADH at λ_{\max} of 340 nm. In this assay, MDH is added to wells containing pyruvate, bicarbonate, and PC, so the decrease in absorbance is due to the oxidation of NADH occurring due to the production of OAA.

Similar to the FVB assay, controls for this reaction include a negative control for inhibition, in which only the necessary substrates, PC, MDH, and NADH are present, and the rates observed for this reaction represent the uninhibited forward reaction of PC. This coupled-enzyme assay also introduces the possibility that small molecule inhibitors tested could inhibit MDH rather than PC, giving a false positive for inhibition. To account for this, a control is performed in which OAA is added directly to MDH both in the presence and absence of a small molecule inhibitor to ensure the rate of oxidation of NADH is unaffected by the small molecule's presence.



Scheme 2.2 Detection of the formation of OAA via MDH coupled-enzyme assay.

2.3 Identification of Mode of Inhibition

Since the compounds examined are likely to be reversible inhibitors, there are three primary modes of enzyme inhibition to consider. Determining which mode of inhibition potent inhibitors proceed through provides indirect evidence of where the inhibitor is binding in the enzyme. For example, an inhibitor that is competitive with respect to pyruvate would strongly suggest that the compound is reaching the CT domain active site to exclude pyruvate.

In competitive inhibition, both the inhibitor and substrate compete for the free enzyme. Binding of the inhibitor then prevents binding of the substrate while binding of the substrate prevents binding of the inhibitor. The implication is that both compounds bind in the active site of the enzyme, but this is not a requirement for competitive inhibition. This mode of inhibition is described in Figure 2.2. As shown in this figure, the inhibitor-bound enzyme complex leads to an inactive enzyme that is unable to generate product. Two essential constants in this model are the Michaelis constant, K_M , and the inhibitor constant, K_I . K_M represents the concentration of substrate required to reach half the maximum rate of reaction. K_I represents the inhibitor concentration required to reduce the reaction rate to half of V_{max} at saturating substrate conditions. In competitive inhibition, as the enzyme-inhibitor complex forms, and thus decreases $[E]$, this shifts the enzyme-substrate equilibrium to the left, increasing the apparent value of K_M in the presence of the inhibitor.

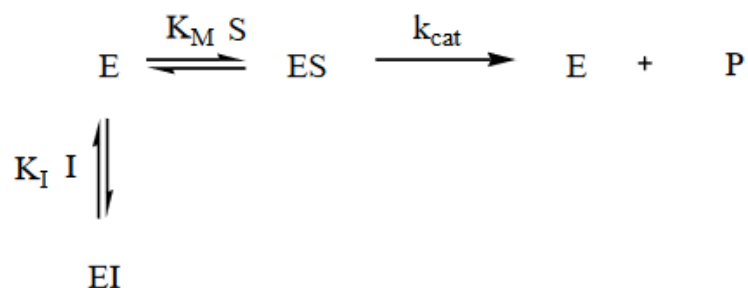


Figure 2.2 Kinetic model of competitive inhibition. E represents the enzyme, S the bona fide substrate, I, the inhibitor, and P, the product. In competitive inhibition, the Michaelis constant, K_M is the concentration of the substrate at which the reaction rate reaches half of the maximum velocity, V_{max} . K_I , then is the concentration of inhibitor at which half the value of V_{max} is achieved at saturating substrate conditions.

Determination of competitive inhibition is apparent after constructing a double reciprocal Lineweaver-Burk plot, plotting reciprocal velocity versus the reciprocal of substrate concentration. Competitive inhibitors will generate a plot in which a series of lines cross the y-axis at the same point, indicating V_{max} is unchanged accompanied by a decreasing value of $1/K_M$, thereby representing a higher K_M value, increasing with inhibitor concentration (Figure 2.3).

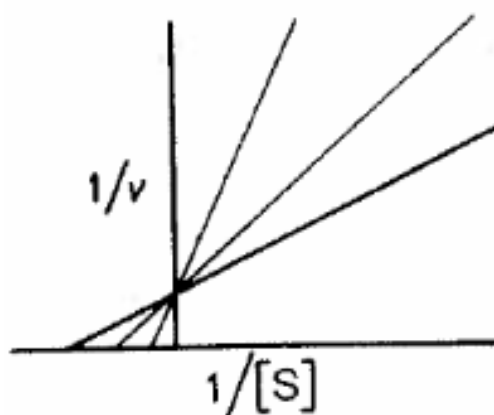


Figure 2.3 Lineweaver Burk plot for a competitive inhibitor. Individual lines represent various concentrations of an inhibitor. Lines with steeper slopes occur for increased inhibitor concentrations.

In noncompetitive inhibition, binding of the substrate or the inhibitor occurs independently of the other. Whether the enzyme first is bound by the inhibitor or the substrate, an enzyme-substrate-inhibitor (ESI) complex can form that is nonproductive. Because the enzyme-substrate complex in the presence of a noncompetitive inhibitor is in equilibrium with the nonproductive ESI complex, noncompetitive inhibition is detectable by a decrease in V_{\max} , ultimately lowering the turnover number, k_{cat} .

Because V_{\max} is affected by inhibitor concentration, a Lineweaver Burk plot for a noncompetitive inhibitor will produce lines with varying slopes, characteristic of an inhibitor binding to free enzyme, that will intersect the y-axis at varying points (Figure 2.4).

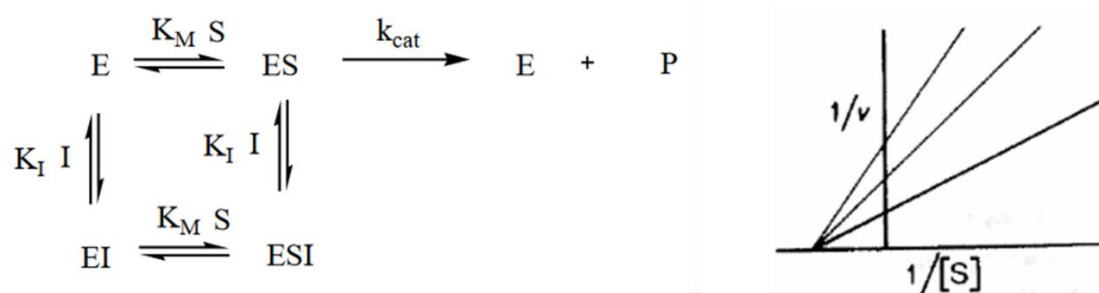


Figure 2.4 (Left) Kinetic model of noncompetitive inhibition. Noncompetitive inhibitors will bind either the free enzyme or the enzyme-substrate complex, resulting in a decrease in V_{\max} and apparent decrease in turnover number, k_{cat} . (Right) Lineweaver Burk plot for noncompetitive inhibition.

Finally, uncompetitive inhibition occurs when the inhibitor binds only the enzyme-substrate complex. Similar to noncompetitive inhibition, this results in a nonproductive ESI complex. Considering Le Chatelier's principle, this formation of the ESI complex promotes formation of the enzyme-substrate complex, thereby resulting in a decrease in K_M . The formation of the nonproductive ESI complex, however, also results in a decreased V_{\max} . In a Lineweaver Burk plot for uncompetitive inhibition, parallel lines

are generated (Figure 2.5). The slope of a Lineweaver Burk plot gives the ratio of K_M to V_{max} , so the generation of parallel lines indicates this ratio will be constant both with respect to inhibitor concentration or the presence of an inhibitor at all.

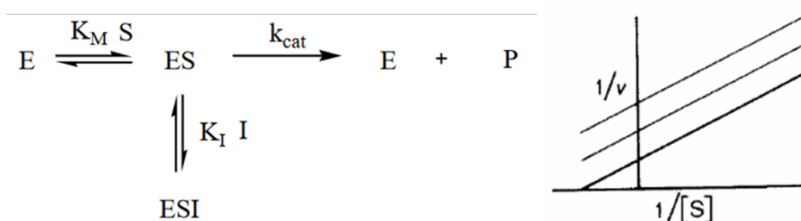


Figure 2.5 (Left) Kinetic model of uncompetitive inhibition, resulting in a decrease in both K_M and V_{max} due to the formation of the nonproductive ESI complex after formation of the ES complex. (Right) Lineweaver Burk plot representative of uncompetitive inhibition.

In the context of this project, modes of inhibition could be evaluated by steady-state kinetic analysis. Highly potent compounds would be characterized for mode of inhibition with respect to both pyruvate and the allosteric activator ATP. This further characterization of the inhibitors in terms of binding constants for the enzyme, corroborates IC_{50} values reported from the FVB and the MDH assays. In addition, a determination of competitive inhibition with respect to pyruvate would provide justification for the use of truncated forms of the enzyme with only the CT domain in co-crystallization studies.

As described in the protocol for the FVB assay, EDTA inactivates the PC enzyme via sequestration of the divalent Mg^{2+} ion in the BC domain. This underscores a potential liability in developing inhibitors of a metalloenzyme like PC which possesses metal-chelating functional groups. As the CT domain has been described as the ideal target for small molecule inhibition, ruling out a mechanism of action in which the compound

targets the BC domain via chelation and sequestration of the Mg^{2+} ions is essential. Still, further study of potent molecules against CT in other metalloenzymes is essential, as a panel of metalloenzymes represents a selection of targets to provide initial insight on the relative selectivity of potent inhibitors against PC. As such, a limited range of assays against other metalloenzymes were developed to further characterize potent inhibitors of PC in terms of selectivity.

2.4 Metalloenzyme Assay Selectivity Panel

Due to the presence of a metal ion in the targeted CT domain active site, the synthetic plans to include metal-chelating functional groups as part of the inhibitor scaffold, and the predicted coordination of inhibitors to the metal ion in the CT domain from docking studies (presented later in this document), it was apparent that the biological evaluation of generated compounds should include screening against other metalloenzymes for the most potent inhibitors characterized. While potency and determination of mode of inhibition are essential in characterizing an inhibitor, the viability of an inhibitor for use as a chemical probe or, eventually as a therapeutic, hinges upon its relative selectivity against other enzymes. While the metalloenzymes screened do not represent a comprehensive selectivity screen, the commonality of metal ions in the active sites do screen for what is a likely liability of the incorporation of metal-chelating functional groups.

Selected for its incorporation of a divalent Zn^{2+} in its active site, human carbonic anhydrase 2 (*hCAII*) regulates blood pH levels by catalyzing hydration of CO_2 , generating bicarbonate.⁷⁷ In the active site of *hCAII*, the divalent zinc is coordinated by a His_3 motif and a hydroxide ion (Figure 2.6). A selection of potent inhibitors of PC were

evaluated in a kinetic assay.⁷⁸ In this assay, the activity of *hCAII* is determined by measuring the absorbance of *p*-nitrophenol, which is produced via *hCAII*'s hydrolysis of the substrate *p*-nitrophenylacetate. As a control, *hCAII* is inhibited with acetazolamide (reported IC_{50} of 25 nM), first reported as an inhibitor of *hCAII* in its connection to its use as a treatment for glaucoma.⁷⁹ Reportedly, the sulfonamide moiety of acetazolamide tightly coordinates the divalent zinc ion of the *hCAII* active site leading to a decrease in the concentration of bicarbonate, in turn causing osmotic depletion of water from the eye, reducing intraocular pressure, contributing to its role as a glaucoma treatment.

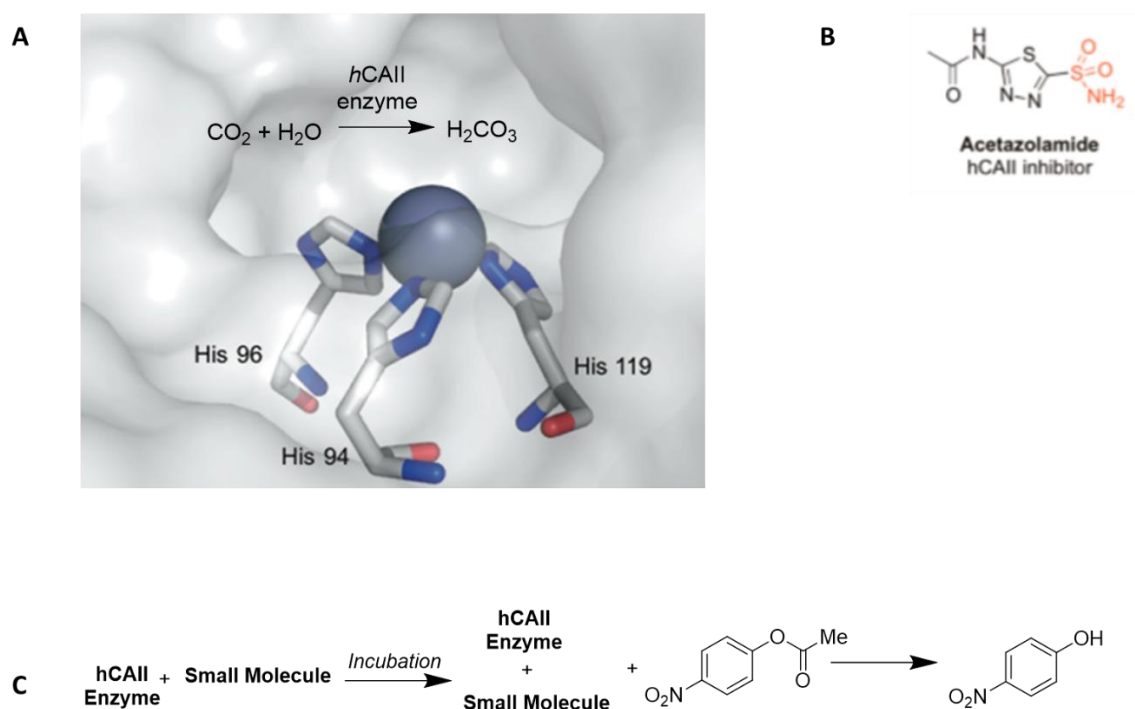


Figure 2.6 A) Active site of *hCAII* enzyme, with catalyzed production of bicarbonate overlaid. Histidine residues shown represent the His₃ binding motif coordinating Zn²⁺ (gray sphere). Not pictured is the hydroxide ion, occupying the fourth coordination site of the divalent zinc ion.⁷⁸ B) Structure of acetazolamide, the known inhibitor of *hCAII* (IC_{50} of 25 nM). C) Reaction scheme for *hCAII* inhibition assay. After small molecule effectors are incubated with the *hCAII* enzyme, activity of the enzyme is determined by measuring the absorbance of *p*-nitrophenol, which is generated by *hCAII*-catalyzed hydrolysis of *p*-nitrophenylacetate.

A second inhibition assay targeting matrix metalloproteinase 2 (MMP-2) was employed to further probe the selectivity of identified potent PC inhibitors. The active site of MMP-2 hosts a catalytic divalent Zn^{2+} cation coordinated by a His₃ motif and a water molecule.⁷⁸ Known inhibitors of MMPs contain a carboxylic acid moiety that coordinates to the divalent zinc cation.⁸⁰

As a class of endopeptidases, MMP enzymes are capable of breaking down connective tissues like gelatin in the case of MMP-2, and are common metalloenzyme targets in medicinal chemistry due to their role in disrupting angiogenesis in malignant tumors.⁸¹ Despite reported susceptibility to incorporation of metal binding groups including carboxylic acids, hydroxamic acids, and hydroxypyridinones, only one compound, doxycycline, is FDA-approved for the treatment of periodontitis.⁸² Due to the presence of metal-binding groups in the design of small molecules tested against PC, the array of reports of the myriad of metal-binding groups inhibiting MMP-2 represents a potential liability for a lack of specificity for compounds potentially inhibiting PC with the incorporation of metal binding groups.

An assay reported by Day and Cohen⁷⁸ was modified for screening activity against MMP-2. In this assay, MMP-2 cleaves a fluorogenic peptidic substrate, OmniMMP. Cleavage of OmniMMP is detected by an increase in fluorescence, so uninhibited MMP-2 activity was determined by monitoring the increase in fluorescence in the absence of small molecule inhibitors, and the fully inhibited signal was determined by introducing saturating concentrations of the known inhibitor N-[(4'-bromo[1,1'-biphenyl]-4-yl)sulfonyl]-L-valine. Potent effectors would be evaluated at concentrations approximately one order of magnitude more dilute than the most potent IC₅₀ values

determined for PC, allowing quantification for a %-inhibition value for each small molecule assayed against MMP-2. The active site and assay conditions are summarized in Figure 2.7.

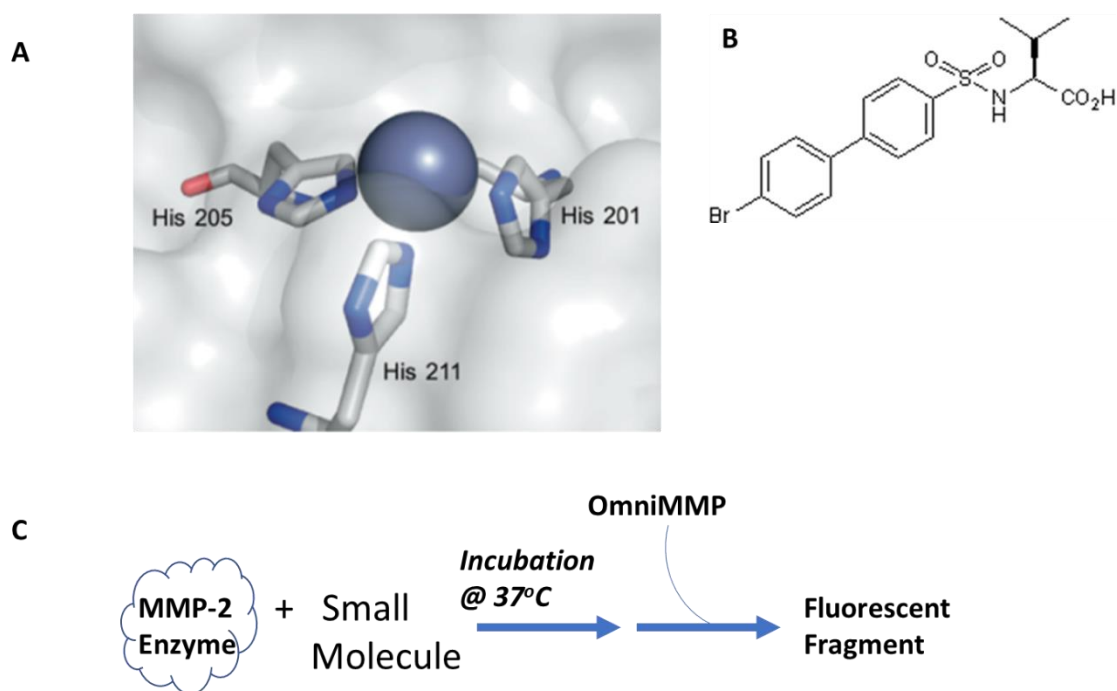


Figure 2.7 A) Active site of MMP-2 enzyme, emphasizing the His₃ metal-binding motif. Not pictured is the water molecule occupying the fourth coordination site of the Zn²⁺ ion (gray sphere)⁷⁸. B) Known inhibitor of MMP-2, N-[(4'-bromo[1,1'-biphenyl]-4-yl)sulfonyl]-L-valine, used for positive control of inhibition in kinetic assay. C) Schematic representation of MMP-2 inhibition assay. After incubation of the MMP-2 enzyme with necessary substrates, in the presence or absence of small molecule effector, the OmniMMP fluorogenic substrate is introduced, and fluorescence due to cleavage of OmniMMP is measured.

Together, the aforementioned assays represent a workflow for initial characterization of small molecule inhibitors of the PC enzyme (Figure 2.8). The FVB assay is suitable for screening small collections of generated compounds, but is also amenable for high throughput screens, so it is well-positioned as the initial assay to gauge

potency of compounds. Following up on potential hits from the FVB assay, the MDH coupled-enzyme assay then confirms hits identified through the FVB assay. As reasonably potent compounds are identified, potential liabilities are then able to be evaluated in the selectivity assays against both *hCAII* and MMP-2. This combination, then, allows not only for identification of functional groups whose inclusion is effective in inhibiting PC itself, but also is essential in identifying moieties that introduce liabilities in terms of specificity. In the following chapter, synthetic studies toward the development of potent inhibitors of PC will be described. Throughout the presentation of small molecules that have been evaluated against PC, assay data from the aforementioned assays will be presented.

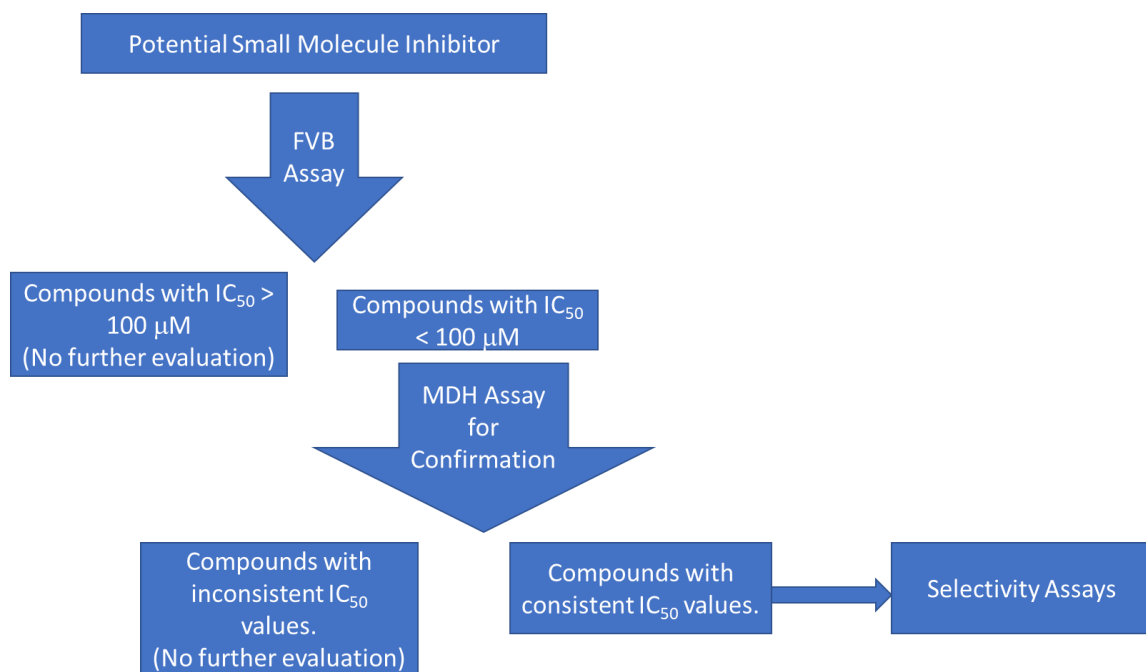


Figure 2.8 Workflow for deciding whether to progress small molecules through various assays.

CHAPTER 3

Identification and Evaluation of Inhibitor Scaffold

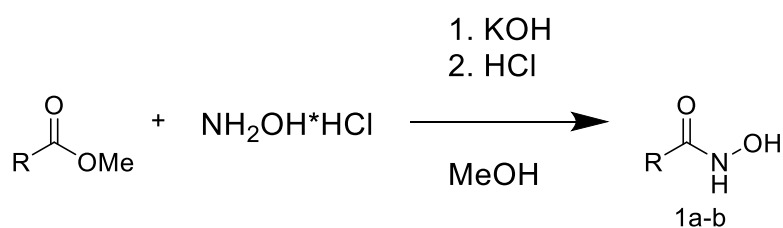
3.1 Attempts Targeting CT Domain

As established in the introduction, the CT domain represents the ideal target for structure-based design of small molecule inhibitors, owing to the well-defined binding pockets of both pyruvate and biotin, as well as the presence of a divalent metal cation. An α -keto acid, pyruvic acid's structural features contributing to its binding affinity in the CT domain active site are the previously described salt bridge formed with the carboxyl moiety and hydrogen bond network formed with the α -keto group.

Hydroxamic acids were proposed as potential competitive inhibitors, maintaining the α -keto group that could conceivably participate in hydrogen-bonding while also introducing the -N-OH moiety, known to demonstrate metal chelation interactions. Examples of hydroxamic acids inhibiting metal-containing enzymes⁸³ suggested testing a small sample of such compounds against the PC enzyme.

Utilizing facile preparation from methyl esters in aqueous media⁸⁴, synthesis was performed by free-basing the hydrochloride salt of hydroxylamine with KOH with subsequent addition to the corresponding methyl ester (Scheme 3.1). Upon acidification, the desired products cleanly precipitated out of solution, and were characterized by ¹³C and ¹H NMR spectroscopy. A characteristic shift of the carbonyl carbon from 172 to 170 ppm in the ¹³C NMR spectrum was observed, and the peak corresponding to the methyl carbon of the methyl ester was absent in the product spectra. In the ¹H NMR spectrum, the absence of the singlet at 3.6 ppm corresponding to the CH₃ of the methyl ester in the starting material. In *d*₆-DMSO, peaks at 10.6-10.8 ppm in the ¹H NMR spectrum due to

the OH proton and peaks at about 8.7 ppm due to the NH proton were used as diagnostic peaks to indicate formation of the desired product. Synthesis of these hydroxamic acids are outlined in Scheme 3.1, with results outlined in Table 3.1.



Scheme 3.1 Synthetic scheme for the synthesis of hydroxamic acids.

Table 3.1 – Hydroxamic Acid Results

Cpd. Number	Structure	%-Yield	IC ₅₀ (FVB)
1a		6.5%	>2 mM
1b		62%	>2 mM
1c*		-	>2 mM

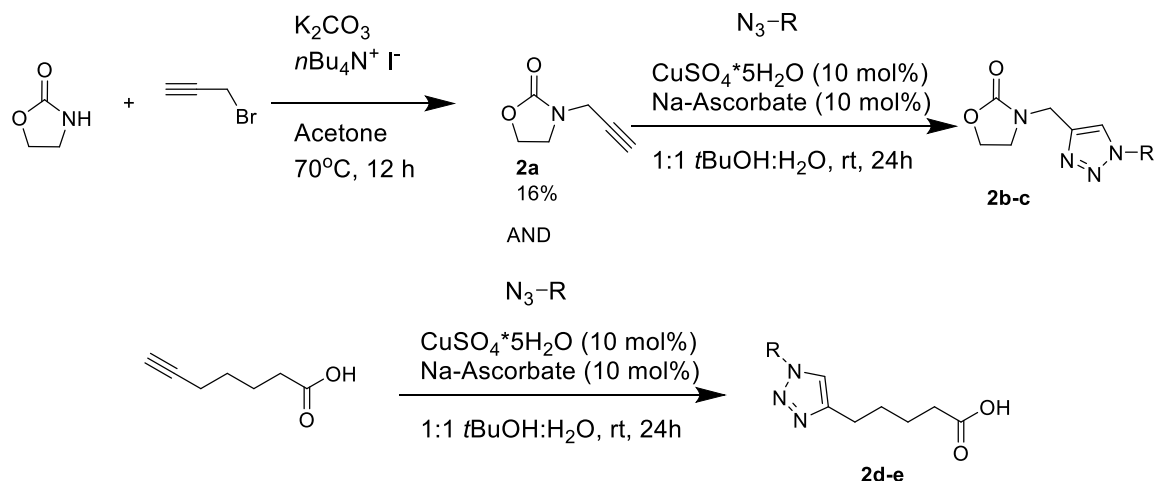
*Cpd. 1c was purchased from a commercial source.

While the hydroxamic acids evaluated represent a limited scope of potential analogues tested, the lack of even modest inhibition illustrates the ineffectiveness of the installation of the hydroxamic acid moiety in favor of the α -keto acid scaffold present in pyruvic acid.

Since X-ray crystal structures exhibited hydrogen bonding to the biotin moiety in the CT active site, it was envisioned that structural analogues such as a 1,2,3-triazole might be another class of inhibitor. The advantage of this approach included the straightforward synthesis via click chemistry. By employing various azides and alkynes in the click reaction, this route promised to open up a wealth of analogues to probe for structure activity relationships. Furthermore, the use of commercially available omega-alkynoic acids were considered, as the presence of a carboxyl group was envisioned to serve as an anchor to the CT domain active site with the carboxyl moiety chelating the divalent cationic metal deep in the active site. To this end, reaction of 6-heptynoic acid with commercially available 2-azidoethanol or *N*-(2-azidoethyl)phthalimide gave the corresponding 1,2,3-triazole-4-pentanoic acids **2d** and **2e** (Scheme 3.2).

Alternative to the carboxylic acids generated, oxazolidinone derivatives were considered as potential biotin mimics as well. The oxazolidinone ring is structurally similar to the ureido ring of biotin, substituting an oxygen for one of the nitrogen atoms of biotin's ureido ring. While commercially available 2-oxazolidinone itself showed no significant inhibitory activity, an alkyne click handle was installed via alkylation of the oxazolidinone nitrogen with propargyl bromide (Scheme 3.2). Alkyne **2a** was further diversified via the click procedure to prepare **2b** and **2c**.

In the ^{13}C NMR spectra of **2b-e** the diagnostic peaks at 68 and 83 ppm corresponding to the terminal alkyne were no longer present in the product spectra, but instead peaks at 123 and 147 ppm were observed, which are consistent with the alkenyl carbons in the triazole ring.



Scheme 3.2 Generation of triazole compounds via click reaction. Cpd. 2b-c represent those bearing the oxazolidinone moiety while cpds. 2d-e represent those generated employing 6-heptynoic acid as the starting alkyne. Triazole compounds were envisioned to serve as structural mimics of biotin.

The synthetic yields and biological evaluation of triazole compounds **2b-e** are presented in Table 3.2. While the scope of triazole compounds evaluated was somewhat limited, absence of even modest inhibition of the PC enzyme prompted the exploration of alternative potential inhibitors.

Table 3.2 – Triazole Compounds

Cpd. Number	Structure	Synthetic Yield	IC ₅₀ (FVB)
2b		64%	>2 mM
2c		56%	>2 mM
2d		34%	>2 mM
2e		68%	>2 mM

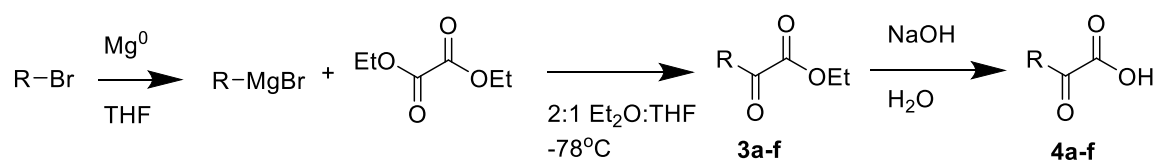
3.2 α -Hydroxycinnamic Acid Scaffold

Encouraged by the reports of inhibitory activity by structurally simple derivatives of pyruvate and the accompanying crystal structures of 3-bromopyruvate and 3-hydroxypyruvate, more complex pyruvate derivatives were prepared and evaluated against *SaPC*.

In pursuit of derivatives of pyruvate, a route was planned that would furnish α -keto ethyl esters en route to the desired α -keto acids, allowing for exploration of the

necessity of the carboxyl moiety, present as a carboxylate under physiologically relevant conditions, versus the tolerance of the ester functionality.

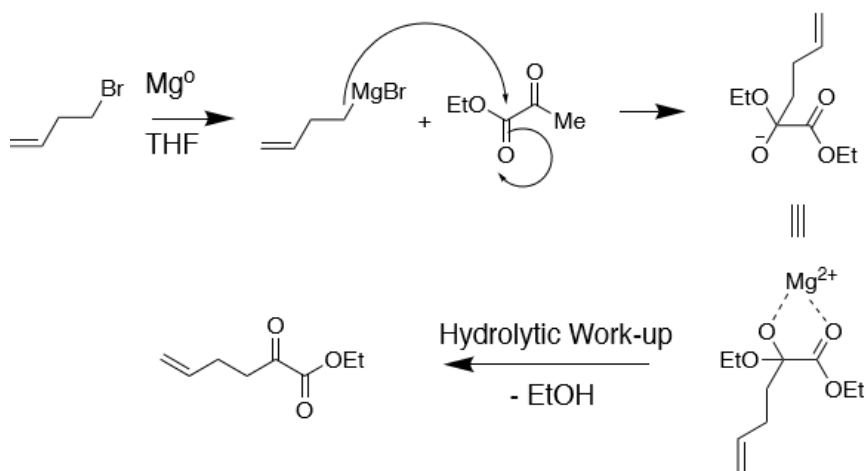
To this end, the initial route relied upon a key Grignard reaction with diethyl oxalate.⁸⁵ The α -keto esters (**3a-f**, Scheme 3.3) thus formed would be subsequently hydrolyzed to furnish the α -keto acids (**4a-f**). The key advantage of this route was the diversity of commercially available alkyl bromides for use as starting material.



Scheme 3.3 General reaction scheme for the generation of α -keto acids proceeding through a key low-temperature Grignard step, followed by alkaline hydrolysis of the resulting ester.

The conditions for the key Grignard reaction step in the sequence shown in Scheme 3.3 are worthy of additional comment. Under the standard conditions for a Grignard reaction, the expected product obtained by treating an ester with a Grignard reagent would be an alcohol. By running the reaction at -78°C the tetrahedral intermediate formed by initial addition of the Grignard is stable toward elimination of the ethoxide ion. Thus, quenching at this temperature, the carbonyl is regenerated, resulting in an α -keto moiety. For clarity, the mechanism for this transformation is shown employing 4-bromo-1-butene as the substrate (Scheme 3.4). After it is formed, the Grignard reagent nucleophilically attacks diethyl oxalate, generating a tetrahedral intermediate. Under standard conditions, this intermediate would collapse, eliminating ethoxide as a leaving group, thereby allowing for subsequent addition of a second

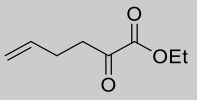
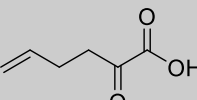
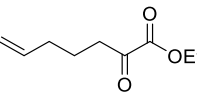
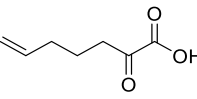
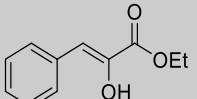
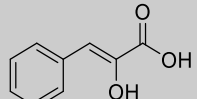
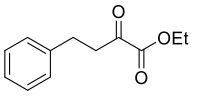
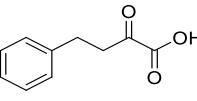
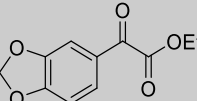
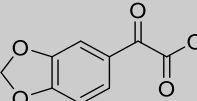
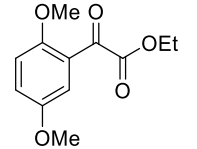
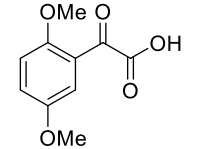
equivalent of the Grignard reagent, furnishing an alcohol upon protic workup. At the low temperatures, however, the tetrahedral intermediate is stabilized via chelation to the Mg^{2+} ion. Quenching this reaction at low temperatures, then, prevents the subsequent attack of a second Grignard reagent, thereby furnishing the α -keto moiety.



Scheme 3.4 Mechanism for the formation of α -keto ester via Grignard reaction. At low temperatures, the tetrahedral adduct is stabilized via chelation to the magnesium until the ketone is regenerated during hydrolytic work-up, eliminating ethanol as a byproduct.

This route furnished a range of compounds, from both aliphatic and aryl bromides. Yields of the esters and their corresponding carboxylic acids as well as IC_{50} values obtained from the FVB assay are presented in Table 3.3.

Table 3.3 – Compounds Generated via Grignard Sequence

Cpd. No.	Structure	Yield	IC ₅₀ (FVB) (μM)	Cpd. No.	Structure	Yield	IC ₅₀ (FVB) (μM)
3a		62%	>2000	4a		29%	>2000
3b		36%	>2000	4b		41%	>2000
3c		34%	>2000	4c		34%	240
3d		52%	>2000	4d		56%	>2000
3e		22%	>2000	4e		35%	>2000
3f		67%	>2000	4f		94%	>2000

The synthesis of this series of compounds and the relative lack of inhibitory activity showcases a couple of important findings. First, characterization of the ethyl phenylpyruvate (**3c**) and pyruvic acid (**4c**) revealed the enol tautomer as the only species present in *d*₆-DMSO. All other compounds in this series were present as exclusively the keto tautomer. These assignments were made based on observations of the recorded

NMR spectra. Signals around δ 30 ppm and δ 3 ppm in the ^{13}C and ^1H NMR spectra, respectively, correspond to the C-3 carbon and associated protons of the compounds predominately in the keto tautomer, while in the case of **3c** and **4c**, signals at around δ 107 ppm in the ^{13}C NMR spectrum and a singlet at δ 6.3 ppm in ^1H NMR spectrum were used in assigning the enol tautomer. Structurally, it can be reasoned that compounds **3c** and **4c** are present predominately as the enol tautomer due to the double bond of the enol forming a conjugated system with the aryl ring.

Furthermore, while the inhibitory activity of **4c** is best described as modest, a significant decrease in PC activity is observed despite a seemingly minor structural modification. The addition of a second methylene unit between the aryl ring and the α -carbonyl (such as in **4d**) shifts the keto-enol equilibrium to favor the keto tautomer because the aforementioned conjugated system will no longer form. Additionally, commercially available phenylglyoxylic acid (Figure 3.1) was evaluated in the FVB assay to further elucidate the significance of the predominance of the enol tautomer.

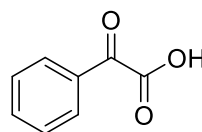


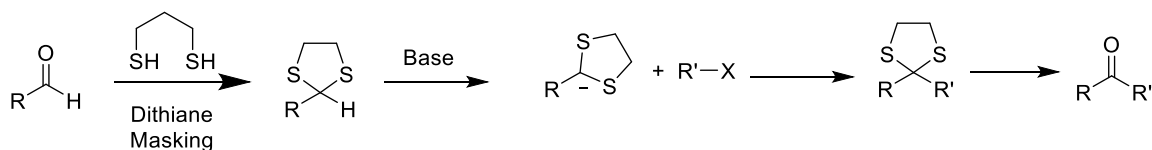
Figure 3.1 Phenylglyoxylic acid.

In comparison to **4c**, phenylglyoxylic acid represents the removal of the methylene unit connecting the aryl ring to the α -keto acid moiety. Similarly to **4d** disfavoring the enol tautomer due to the lack of conjugation, phenylglyoxylic acid is not

capable of existing as the enol tautomer. The IC_{50} is $>2000 \mu\text{M}$, further indicating **4c**'s predominance as the enol tautomer contributes to its enhanced potency compared to these examples. While **4e** and **4f** similarly restrict the formation of the enol tautomer, phenylglyoxylic acid was an important compound to evaluate to attribute the significance to the difference in keto-enol tautomerization rather than the presence of the aryl substituents present in compounds **4e** and **4f**.

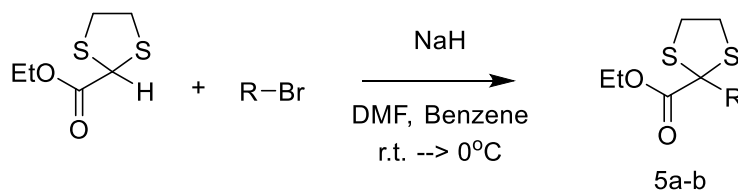
While the inhibitory activity of **4c** was somewhat modest, it was approximately as potent as 3-bromopyruvate, and this phenylpyruvic acid structure represents a readily diversifiable scaffold to begin structure-activity relationships. Among the variables to be examined, introducing substituents of a variety of simple electron-donating or electron-withdrawing substituents to the aryl ring was a straightforward next step in identifying potential inhibitors of PC.

To this end, alternative routes to generate α -keto or α -hydroxy acids were explored. Initially, umpolung, or polarity inversion, chemistry was explored. By masking a carbonyl with a 1,3-dithiane and subsequent treatment with a strong base, it is possible to generate a sulfur-stabilized acyl anion equivalent capable of performing S_N2 reactions on alkyl halides.⁸⁶ Deprotection of the dithiane moiety would then regenerate the carbonyl, as illustrated in Scheme 3.5.



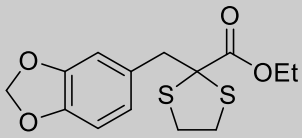
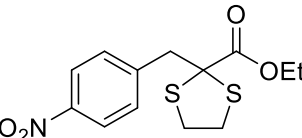
Scheme 3.5 General umpolung reaction sequence.

Conveniently, ethyl 1,3-dithiane-2-carboxylate (**5**) is a commercially available starting material with the 1,3-dithiane moiety ideally positioned alpha to the ester, providing a straightforward route to a diverse array of α -keto esters. Reaction of the anion generated from **5** with either piperonyl bromide or 4-nitrobenzyl bromide gave products **5a** and **5b** (Scheme 3.6, Table 3.4). On a small scale (1 mmol of starting bromide), the substituted dithiane was obtained cleanly. This reaction, however, was not amenable to scale-up, producing instead a complex mixture as indicated by NMR spectroscopy. Attempts to demask the dithiane to furnish the desired α -keto ester using NBS were unsuccessful on this scale.



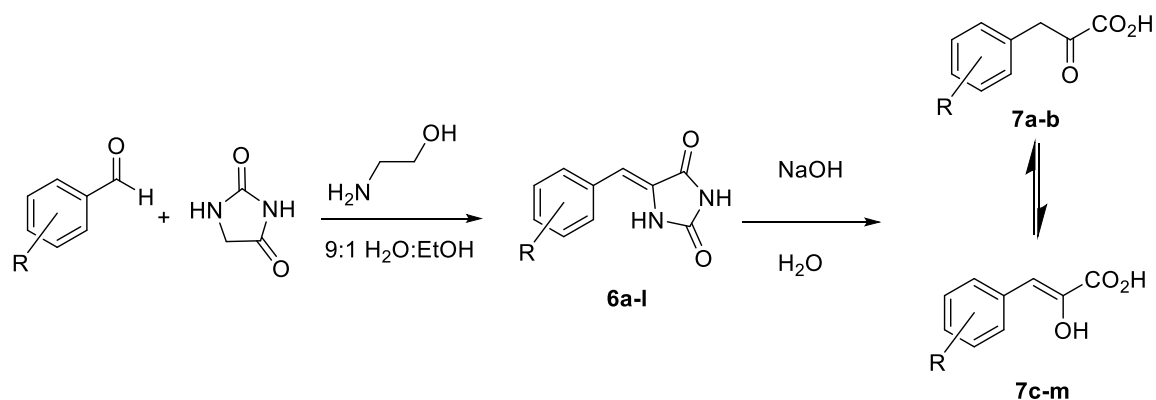
Scheme 3.6 Umpolung sequence employed en route to α -keto ester.

Table 3.4 – Esters Generated via Umpolung Synthesis

Cpd. Number	Structure	Synthetic Yield	IC ₅₀ (FVB) (μM)
5a		95%	>2000
5b		65%	>2000

While the umpolung synthetic route offered the potential of a wide substrates scope, its lack of scalability and unreliable demasking of the dithiane moiety underscored the necessity to develop a more robust synthetic route to generate substituted phenylpyruvic acids to obtain initial structure-activity relationships.

Employing a diverse array of commercially available benzaldehydes as starting material, synthesis of α -keto acids was achieved via Knoevenagel condensation with hydantoin, followed by subsequent base hydrolysis.⁸⁹ While yields for the Knoevenagel synthetic route (Scheme 3.6) were typically modest, products were typically obtained cleanly.

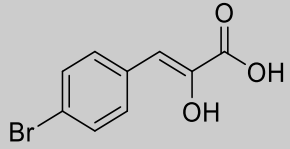
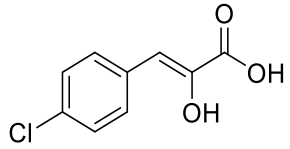
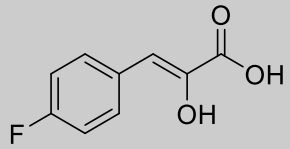
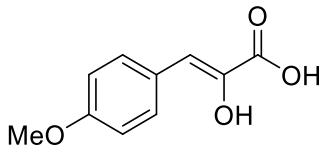
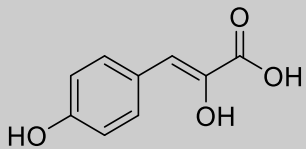
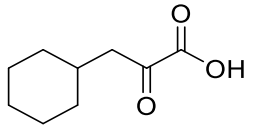


Scheme 3.6 Knoevenagel synthetic sequence to generate either α -keto acid (**7a-b**) or α -hydroxycinnamic acids (**7c-l**). In NMR spectra recorded in *d*₆-DMSO, the final compounds generally were observed in only the α -hydroxycinnamic acid tautomer, not the expected α -keto acid tautomer.⁹

In planning this route, it was anticipated that the final products would predominately form in the α -keto acid tautomer. The enol (α -hydroxycinnamic acid) tautomer, however, was found to be the predominant tautomer in the majority of cases. Compounds **7a** and **7b** are likely observed in the α -keto acid tautomer due to the presence of an *ortho*-substituent. This observation is consistent with a previous report that the keto-enol tautomerization equilibrium of phenylpyruvic acids is governed by steric, rather than electronic, factors.⁹⁰ Assignments of the keto or enol tautomer were dependent on their NMR spectral data. In particular, the presence of signals at δ 107 ppm and $\sim \delta$ 6.5 ppm (s, 1H) in the ¹³C NMR and ¹H NMR spectra in *d*₆-DMSO, could be assigned to C-3 and its attached proton respectively in the enol tautomer. Alternatively, signals at δ 30 ppm in the ¹³C NMR spectra and at δ 3 ppm in the ¹H NMR spectra were diagnostic in determining the predominance of the keto tautomer.⁹⁰ FVB and MDH data for compounds generated via this route are provided in Table 3.5

Table 3.5 – Compounds via Knoevenagel Synthetic Route

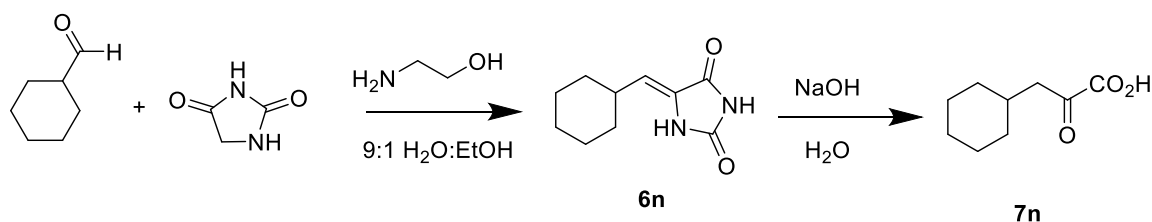
Cpd. Number	Structure	IC ₅₀ (FVB) (μM)	IC ₅₀ (MDH) (μM)
7a		>1000	>1000
7b		>2000	>2000
7c		240	130
7d		>1000	>1000
7e		360	23
7f		210	140
7g		98	38
7h		130	96

7i		200	81
7j		280	220
7k		100	30
7l		170	56
7m		67	22
7n		> 1000	-

Based on the results presented in Table 3.5, promising inhibitory activity is observed primarily for those compounds that exist predominantly in the enol tautomer, while compounds favoring the α -keto tautomer showed negligible inhibitory activity. As shown in Scheme 1.3, pyruvate must transition through an enolate intermediate to undergo carboxylation, generating oxaloacetate. Considering this, the α -

hydroxycinnamic acids are more likely to serve as transition state analogues, thereby increasing their affinity for the PC enzyme. Moreover, this would suggest the inhibitory activity is due to the α -hydroxycinnamic acids binding in the CT domain of PC. The electronic nature of the substituent does not appear to influence either the keto-enol equilibrium, as previously established, nor does it seem to strongly impact inhibitory activity, as **7d**, bearing an electron-withdrawing nitro group in the *para*- position exhibits negligible inhibitory activity, while **7h**, with an electron-withdrawing trifluoromethyl group, also in the *para*- position, is significantly more potent with an IC_{50} in the FVB assay of 130 μ M.

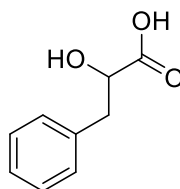
In addition to generating substituted phenylpyruvic acids, the Knoevenagel sequence was amenable to at least one aliphatic substrate, cyclohexanecarboxaldehyde, generating 3-cyclohexyl-2-oxopropanoic acid (cpd. **7n**). This compound was observed only in the α -keto tautomer, and consistent with previously described observations demonstrated negligible inhibitory activity, with an IC_{50} of over 1000 μ M in the FVB assay.



Scheme 3.7 Knoevenagel sequence employed to generate 3-cyclohexyl-2-oxopropanoic acid.

While the data presented in Table 3.5 suggests the α -hydroxycinnamic acid scaffold presents a promising scaffold for the development of potent inhibitors of PC, it is unclear if the presence of an α -hydroxy group alone that contributed to the increased potency of the compounds existing predominantly as α -hydroxycinnamic acids compared to those existing favorably in the α -keto acid tautomer, or if the enol character contributed to the enhanced potency.

To this end, phenyllactic acid (Figure 3.5) was evaluated in the FVB assay, as this compound is structurally similar to phenylpyruvic acid (cpd. 7c), eliminating only the double bond of the enol. Assayed against *Sa*PC in the FVB assay, phenyllactic acid demonstrated negligible inhibitory activity, with an IC_{50} greater than 3000 μ M.



Phenyllactic Acid

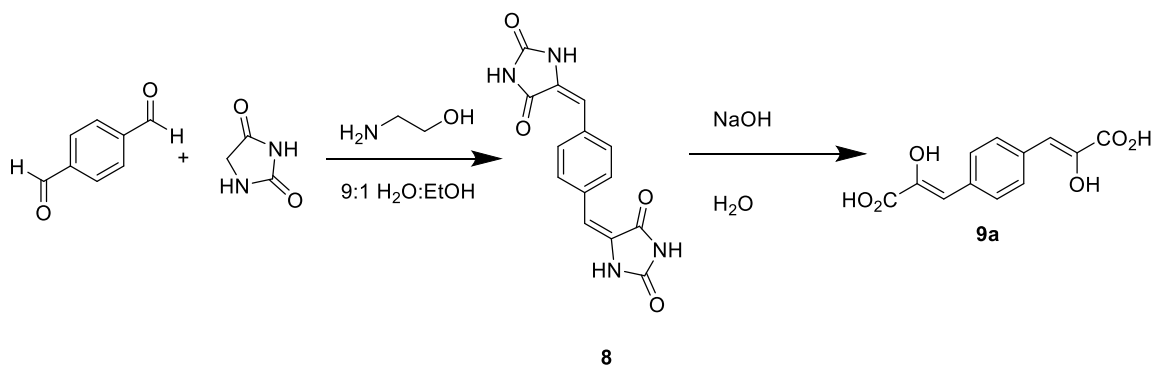
Figure 3.5 Phenyllactic acid exhibited negligible inhibitory activity with an IC_{50} of over 3000 μ M when assayed against *Sa*PC in the FVB assay.

This lack of activity observed with phenyllactic acid, taken together with the lack of activity of compounds existing primarily as the α -keto acid tautomer directed further exploration of the aryl pyruvic acid scaffold.

3.3 Expansion of α -Hydroxycinnamic Acid Scaffold

3.3.A. Synthesis of 3,3'-(1,4-Phenylene)bis[2-hydroxy-2-propenoic acid]

Due to the relative potency of phenylpyruvic acid (**7c**) and the ease of the Knoevenagel synthetic sequence, introduction of a second α -enolic acid moiety via the same sequence proved to be a straightforward method to introduce a sterically bulkier and electronically intriguing substituent in the *para*- position of phenylpyruvic acid, which would clarify if other substitutions would be tolerated by PC. To this end, 1,4-dibenzaldehyde was employed as the starting material in the Knoevenagel sequence (Scheme 3.8).



Scheme 3.8 Synthesis of 3,3'-(1,4-Phenylene)bis[2-hydroxy-2-propenoic acid] (**9a**).

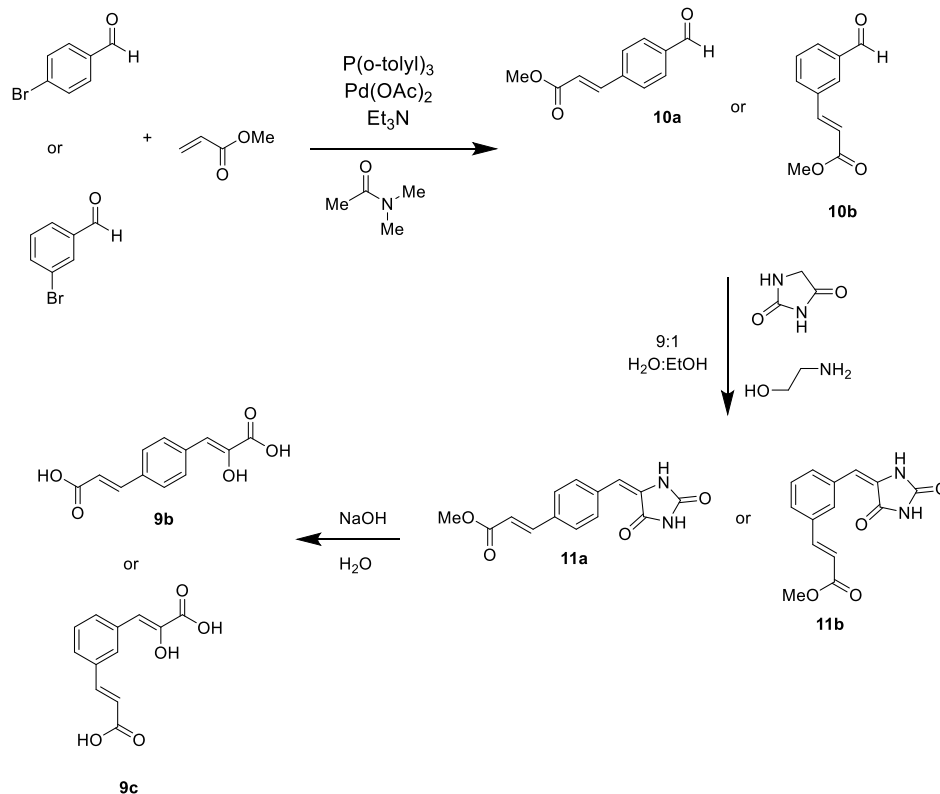
Shown in Table 3.6, the IC_{50} of **9a** determined against *Sa*PC in the FVB assay was found to be $3.0 \pm 1.0 \mu\text{M}$, several orders of magnitude greater than the potency observed for phenylpyruvic acid (**7c**). While the identification of a small molecule inhibitor with a single-digit micromolar IC_{50} against PC is significant on its own, it also

demonstrates the tolerance for bulkier substituents to be installed *para*- to the necessary α -enolic acid moiety. The incorporation of the second carboxylic acid, however, does introduce some potential liabilities, including the addition of a second metal binding group, underscoring the need for a panel to gauge selectivity of PC inhibitors against other metalloenzymes, which will be expanded upon in the following chapter.

The tolerance of a bulkier functional group opened up the possibilities for exploring other methods of further functionalization of the phenylpyruvic acid scaffold. The facile synthesis of both *p*-bromophenylpyruvic acid (**7i**) and the precursor hydantoin (**6i**) serves as an important route to generating compounds via commonly employed transition metal catalyzed reactions.

3.3.B. Expansion via Heck Coupling

In considering further exploration of the installation of various functional groups, a Heck coupling sequence was envisaged to generate *trans*-cinnamic acids analogous to **9a**, lacking the enolic hydroxy group of one α -enolic acid moiety. To this end, multiple routes were explored. The *para*- and *meta*- *trans*-cinnamic acid were obtained by the sequence shown in Scheme 3.8, lending the advantage of hydrolysis of both the benzylhydantoin moiety to generate the phenylpyruvic scaffold concurrent with the hydrolysis of the methyl ester to generate the carboxylic acid in the *para*- or *meta*-position.



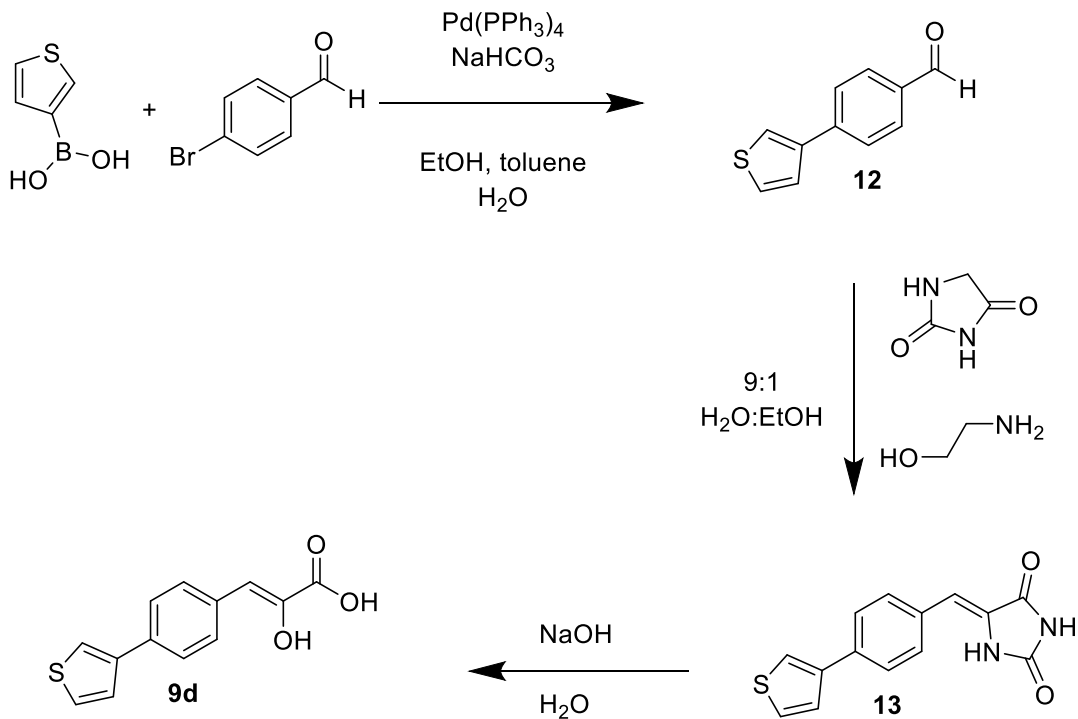
Scheme 3.9 Generation of *trans*-cinnamic acids via Heck coupling sequence.

Assayed against *SaPC* in the FVB assay, IC_{50} values for **9b** and **9c** were found to be 58.6 and 118 μM , respectively (Table 3.6). While **9b** is approximately one order of magnitude less potent than the **9a**, this result marked an important finding in marking improved potency over simply the generic phenylpyruvic acid scaffold (**7c**) for both the bulkier *para*- and *meta*- substituted *trans*-cinnamic acids, indicating that the inclusion of larger, bulkier substituents could lead to enhanced inhibitory activity. Moreover, the decreased potency does implicate the second enolic hydroxy group as contributing to the potency of **9a**, a finding that is more clearly understood on the basis of computationally docked structures presented in the following chapter.

While the decreased potency observed by these *trans*-cinnamic acids is noteworthy, it is also important to note that these compounds do not address fully the aforementioned liabilities of **9a**. These compounds still incorporate a second metal-binding group, remote from the identified pharmacophoric phenylpyruvic acid scaffold. Furthermore, while the added α,β -unsaturated carboxylic acids are still relatively tolerated, the decrease in potency warranted exploration of bulkier substituents. Conveniently, transition-metal catalyzed synthetic techniques could be employed to introduce bulkier substituents as well.

3.3.C. Expansion via Suzuki Coupling

In addition to the exploration of appending a bulkier substituent to the phenylpyruvic acid scaffold, the Suzuki reaction offered a convenient route to the addition of a second aromatic ring, increasing the degree of conjugation in the aromatic system, pushing the keto-enol tautomerization equilibrium to further favor the enol tautomer. This strategy allowed for the installation of a thiophene ring, generating **9d**, outlined in Scheme 3.9.



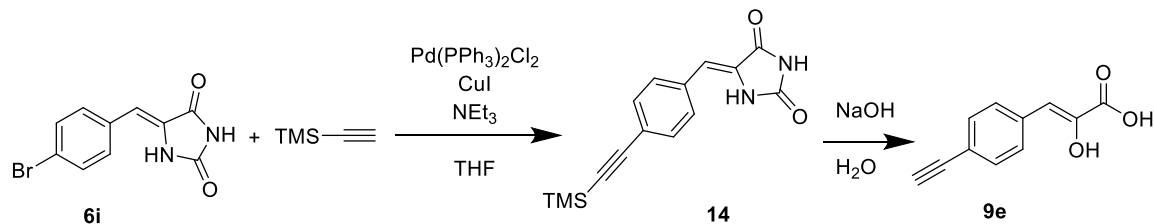
Scheme 3.10 Suzuki reaction sequence employed to generate 2-hydroxy-3-[4-(3-thienyl)phenyl]-2-propenoic acid (cpd. **9d**)

With an IC₅₀ value of 48.0 μM as determined against SaPC in the FVB assay, **9d** is still approximately one order of magnitude less potent than **9a**. Despite its diminished inhibitory activity, incorporation of the thiophene ring in **9d** does highlight potential usefulness in crystallographic studies, as the electron density of this additional aromatic ring would be useful in identifying the bound ligand if suitable crystals of PC are able to be grown in the presence of **9d**. It is important to note that despite diminished inhibitory activity compared to **9a**, analogs **9b-d** do demonstrate increased potency of the simpler monosubstituted phenylpyruvic acids, warranting further exploration into the incorporation of a wider variety of substituents.

3.3.D. Expansion via Sonogashira Reaction

The Sonogashira reaction is a cross-coupling reaction capable of generating a new carbon-carbon bond between terminal alkynes and aryl halides. In envisioning a synthetic route to generate a readily diversifiable scaffold, the Sonogashira reaction opens up the possibility of installing a terminal alkyne in the *para*- position of phenylpyruvic acid, which would serve as a “click handle” to generate triazole compounds by employing click chemistry methods previously described.

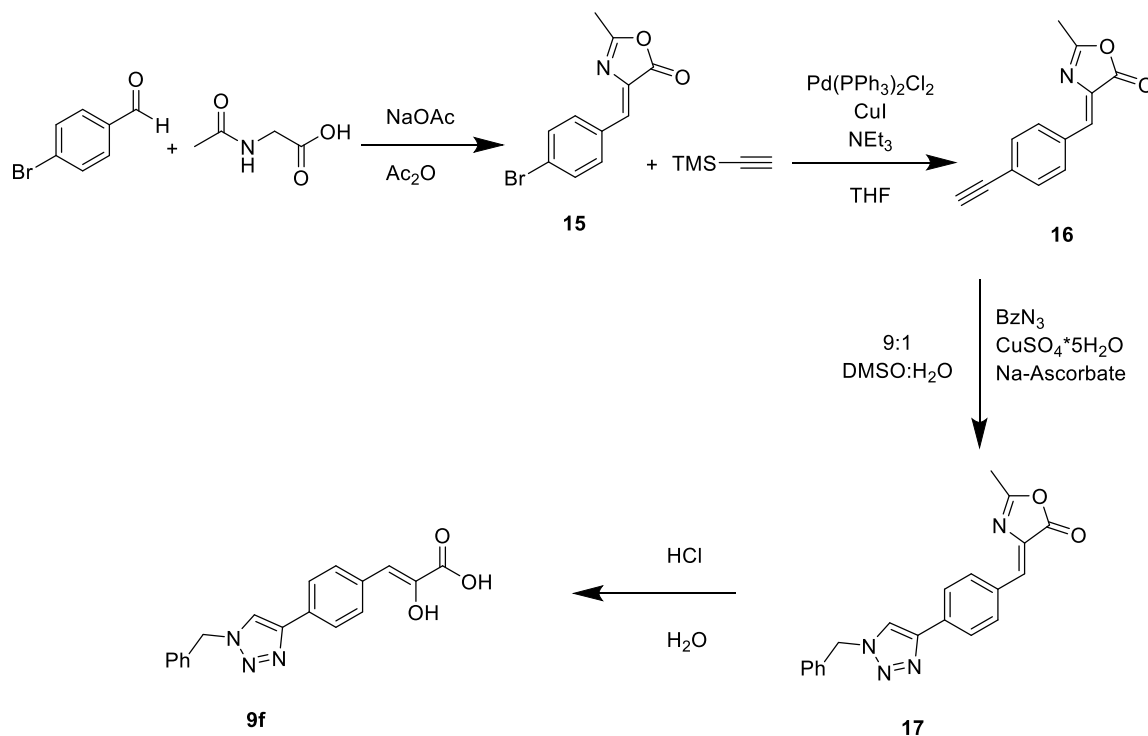
Using commercially available trimethylsilylacetylene as the free alkyne, the optimal route to generate a phenylpyruvic acid with a free alkyne click handle is outlined in Scheme 3.11. The primary focus of optimization was determining at which step to perform the Sonogashira coupling to introduce the alkyne. It was determined on the basis of both synthetic yield and consistency and robustness of reaction conditions that the optimal step to introduce the alkyne should follow the generation of 4-bromobenzylhydantoin (**6i**). Installation of the alkyne at this step provided the advantage of allowing deprotection of the TMS-protected alkyne and hydrolysis of the hydantoin moiety to generate the α -enolic acid in the same step. Generation of **9e** in this fashion furnished enough material for evaluation in the FVB assay. Attempts to further functionalize **9e**, however, were unsuccessful, and quantities produced of **9e** restricted functionalization attempts to small scales.



Scheme 3.11 Sonogashira coupling sequence to generate cpd. **9e**.

While still approximately one order of magnitude less potent than **9a**, **9e** was determined to have an IC₅₀ of 23.8 μM when assayed against PC in the FVB assay (Table 3.6). To compensate for the low quantities of **9e** generated, an alternative route was explored for the generation of α-hydroxycinnamic acids bearing a triazole at the para position. An alternative method relying on condensation of N-acetylglycine and benzaldehydes generally provided improved yields over the Knoevenagel condensation route, with similarly facile hydrolysis affording the substituted phenylpyruvic acid (Scheme 3.12). After purification of the alkynylated methyloxazolidinone intermediate via column chromatography, the TMS protecting group had been lost, furnishing the free alkyne (**16**). Reaction of **16** with benzylazide under standard alkyne-azide click reaction conditions, followed by hydrolysis afforded the triazole-substituted phenylpyruvic acid, **9f**. Unfortunately, the addition of this bulky triazole system was not well-tolerated, and an IC₅₀ of 306 μM against PC was determined in the FVB assay (Table 3.6). Still, these synthetic sequences warrant further exploration of the incorporation of less-bulky triazoles if more optimal synthetic routes to generate this class of compound are identified.

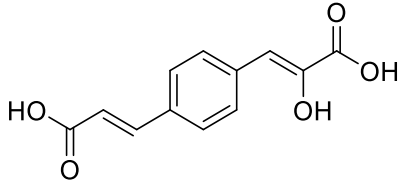
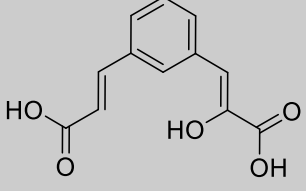
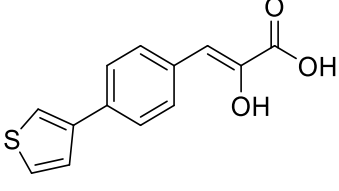
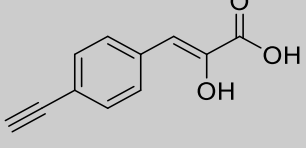
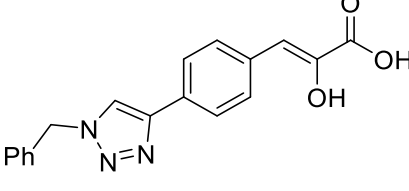
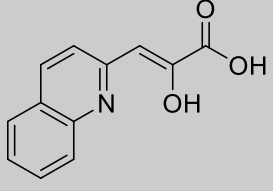
The inhibitors generated via transition-metal catalyzed synthetic methods and pertinent biological data are presented in Table 3.6.



Scheme 3.12 Generation of triazole-substituted phenylpyruvic acid **9f**.

Table 3.6 – Expanded Phenylpyruvic Acid Evaluation

Cpd. Number	Structure	IC ₅₀ (FVB)	IC ₅₀ (MDH)
		(μM)	(μM)
9a		3.0 \pm 1.0	11

9b		58.6	-
9c		118	-
9d		48.0	-
9e		23.8	-
9f		306	-
18		4.3 ± 1.5	3.2 ± 0.5

3.4. Heteroaromatic Inhibitors

In addition to the aforementioned compounds, 2-hydroxy-3-(quinolin-2-yl)propenoic acid (**18**) was purchased to be evaluated as an inhibitor of PC. As shown in Figure 3.6, **18** promised to serve as a transition state analog of pyruvate, owing to its stabilization of the enol via conjugation with the aromatic system, as observed in the phenylpyruvic acids, but also due to an intramolecular H-N bond. If preference for the enol tautomer is significant to inhibitory activity against PC, these factors, taken together, make the heteroaromatic quinoline ring system an attractive candidate to assay.

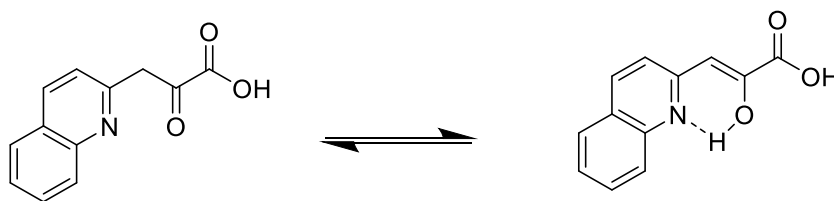
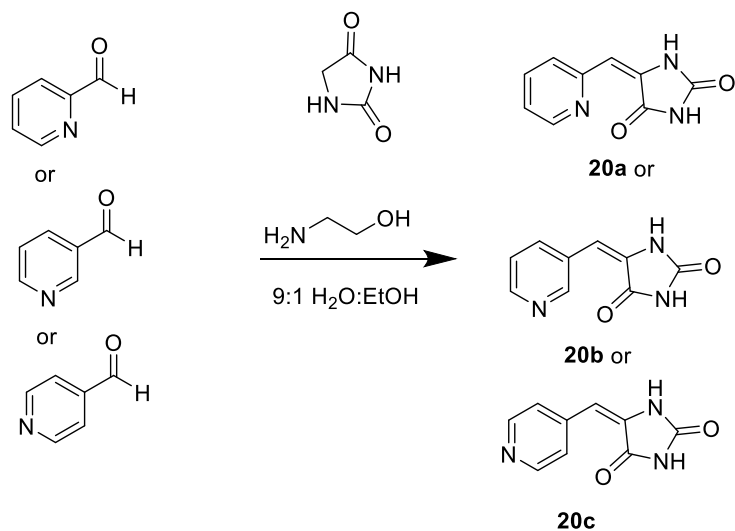


Figure 3.6 Keto-enol equilibrium of cpd. **18**. The enol tautomer is favored due to the conjugation of the enol with the aromatic system and the intramolecular N-H bond that forms.

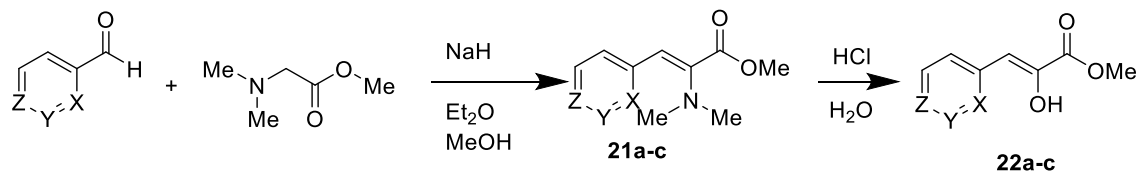
Assayed against PC in the FVB assay, an IC_{50} of $4.3 \pm 1.5 \mu\text{M}$, which is approximately equipotent as **9a**, the only other single-digit micromolar inhibitor of PC reported (Table 3.6). Buoyed by this encouraging increase in potency with the inclusion of a nitrogen-containing aromatic system, attempts to generate analogous pyridine-based α -hydroxycinnamic acids were explored. Knoevenagel condensation of hydantoin with 2-pyridinecarboxaldehyde, 3-pyridinecarboxaldehyde, and 4-pyridinecarboxaldehyde successfully yielded the 5-(pyridinylmethylene)-2,4-imidazolidinediones (Scheme 3.13). Attempts to hydrolyze these intermediates however, were unsuccessful due to an inability

to isolate the product acid.



Scheme 3.13 Generation of 5-(pyridinylmethylene)-2,4-imidazolidinonediones.

An aldol-type condensation of *N,N*-dimethylglycine methyl ester with the aforementioned pyridine carboxaldehydes gave the corresponding α -(dimethylamino)-2-pyridine-2-propenoic acid methyl esters **21a-c** (Scheme 3.14). Acidic hydrolysis of the enamines **21a-c** gave the corresponding α -hydroxy-2-pyridine-2-propenoic acid methyl esters **22a-c**.



Scheme 3.14 Generation of pyridine-derived methyl α -hydroxycinnamates.

Unfortunately, as shown in Table 3.7, these compounds either showed modest inhibition at best, or in the case of the 2-pyridine-derived cinnamate (**21a**), interfered with the formation of the FVB-OAA colored adduct, preventing the determination of an IC₅₀ value. Attempts to isolate the further hydrolyzed propenoic acids were unsuccessful, as the pK_a of the pyridinyl nitrogen is approximately the same as the pK_a of the terminal carboxyl group. As such, protonation of the carboxyl moiety resulted in protonation of the pyridine moiety, and the compound was inseparable from its aqueous media.

Table 3.7 – Methyl α -Hydroxycinnamates

Cpd. #	X	Y	Z	IC ₅₀ (μ M) (FVB)
22a	N	C	C	Indeterminate.
22b	C	N	C	>1000
22c	C	C	N	986

Despite the difficulties of generating nitrogen-containing α -hydroxycinnamic acids, a range of potent inhibitors were identified. To better prepare for subsequent generations of inhibitors, it is important to understand how the inhibitors bind the enzyme, as well as identifying liabilities. Chiefly among potential liabilities is relative selectivity of these inhibitors for PC. In the absence of crystallographic data, computational docking was employed to garner insight into the binding mode of these inhibitors. Additionally, a selection of the most potent inhibitors were characterized in terms of selectivity against a selection of metalloenzymes. These results will be described in the following chapter.

CHAPTER 4 Computational Docking and Enzyme Selectivity

4.1 Determination of Mode of Inhibition of Compound 18

Steady-state kinetic analysis of **18** made possible the determination of its K_i value and mode of inhibition. Compound **18** is a competitive inhibitor with respect to pyruvate with a K_i of $0.74 \mu\text{M}$, and a mixed-type inhibitor with respect to ATP with a K_i of $5.2 \mu\text{M}$. The K_i closely matches that predicted by the Cheng-Prussoff equation ($0.46 \mu\text{M}$). This close match of predictive and experimentally determined K_i values, coupled with the unaltered binding affinity with increased ATP concentration suggests **18**'s direct competition with pyruvate in the CT domain active site. Competitive inhibition was also determined for **7f**.⁸⁹ These data suggest α -hydroxycinnamic acids inhibit PC by specifically targeting the CT domain. Competition with pyruvate and this specific targeting of the CT domain, then, should lend confidence to hypotheses based on the computational docking that has been performed, as calculations were conducted such that molecules were docked in the pyruvate binding site.

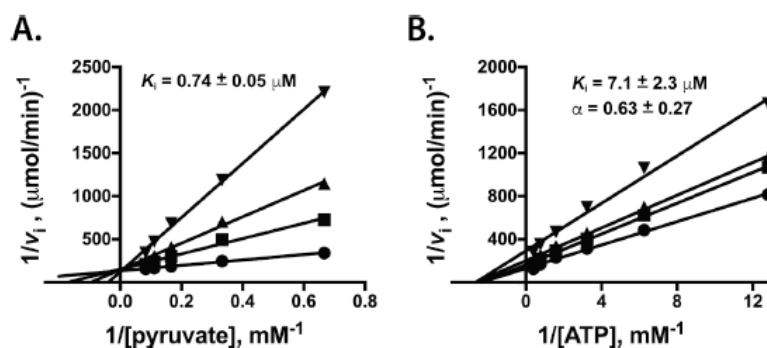


Figure 4.1 (A) Double-reciprocal plot demonstrating competitive inhibition of **18** with respect to pyruvate ($K_i = 0.74 \mu\text{M}$). (B) Double-reciprocal plot demonstrating mixed-time inhibition of **18** with respect to ATP ($K_i = 5.2 \mu\text{M}$). Initial velocities were determined at the following concentrations of **18**: 0 μM (circles), 1.5 μM (squares), 3 μM (upright triangles), and 6 μM (inverse triangles).⁸⁹

4.2 Computational Docking of PC Inhibitors

As described previously, inhibitors with a range of potencies against PC were successfully identified via the FVB and MDH assay. While these data are helpful in drawing conclusions about necessary pharmacophores, in the absence of a crystal structure with an inhibitor bound, it is difficult to rationalize the observed potencies on a structural basis. While crystallographic efforts are ongoing, computational docking has allowed for the development of a hypothesis with respect to the binding mode of potent inhibitors.

Because of the dynamic nature of PC, undergoing several conformational changes throughout the carboxylation of pyruvate, several variables must be considered. As previously described, the translocation of biotin from the BC domain to the CT domain represents the key conformational change PC undergoes. The absence of the tethered biotin cofactor in the CT domain will be referred to as the “open” conformation, while the conformer with biotin present will be referred to as “closed.” Because *Sa*PC is used in the FVB assay, docking experiments were carried out using its structure (pdb code 3BG5).

Beyond this, the inclusion or exclusion of biotin in the docking must be considered. If small molecule inhibitors access the CT domain prior to the translocation of biotin, which is reasonable due to the alleviated sterics of the open conformer, it is possible to envisage binding modes of the inhibitors in which the biotin binding site is accessed. While docking molecules in the open conformer in the absence of biotin was performed, it is perhaps not the best environment for docking. Evidence for a substrate-

induced conformational change to the closed conformation⁹¹ suggests the more pertinent conformer for docking would be the closed conformer. In the closed conformation, the carboxyl moiety of pyruvate forms a salt bridge with the guanidinium side chain of Arg644 (human PC numbering), and Arg571 and Gln575, essential in stabilizing the enolpyruvate intermediate, are within hydrogen bonding distance of the carbonyl oxygen.⁸⁹ Docking in both the presence and absence of the biotin cofactor was attempted, though results consistently showed inhibitors accessing the biotin binding pocket, so the closed conformer in the absence of biotin will serve as the principal conformer employed for computational docking.

Docking studies were carried out using the Molecular Forecaster FITTED suite. It is essential to understand the parameters of such a computational method. Chiefly, only a select portion of the protein will be evaluated for ligand-protein interactions. Understanding this, images produced via computational docking with ligands bound in the CT domain do not imply this is the true target of the small molecule effector. Rather, the docking is biased in this manner, as evaluation of protein-ligand interactions are limited to the CT domain. Despite this bias, interactions predicted in this way do give support to the hypothesis of the evaluated inhibitors binding in the CT domain by identifying reasonable protein-ligand interactions.

In generating molecules for docking, FITTED evaluates several parameters of a 2D-ligand file. Hybridization of atoms are established, pKa values of any nitrogen atoms are established, tautomers and stereoisomers are identified, hydrogen atoms are included, bond lengths and angles are optimized, energy-minimization is performed on the basis of molecular mechanics, and converts the two-dimensional file into a 3D structure

interpreted by the docking algorithm.⁹² Additionally, the protein must be converted from a protein program database (PDB) file to be used in the docking protocol. Through an iterative process, protein PDB files are evaluated for the best combination of potential sidechain rotamers, protonation states, and orientation of water molecules. Especially pertinent to computational docking for this study, the conversion of the protein PDB file also distinguishes between the protein and ligands bound in the crystal structure. As such, the bound pyruvate is recognized as a distinct entity from PC. To carry out docking, the pyruvate ligand is removed from the structure, and the inhibitor's energy is minimized proximal to pyruvate's location, underscoring a liability of this protocol. Except in rare cases, molecules were forced into a pose in the CT domain. As such, successful generation of a docked image does not necessarily imply a reasonable binding mode.

When pyruvate itself was docked in the CT domain active site, the adopted pose was analogous to the pose observed in the crystal structures with PC bound, lending confidence to the docking protocol.

While computational docking did furnish docking scores based on calculated free energies of predicted binding modes, no discernible trend between the docking score and observed IC₅₀ values was identified. This underscores how computational docking should be viewed within the context of this project. For development of future generations of inhibitors, it is important to identify interactions of the lead inhibitors, and rely on evaluation of the geometry of the docked pose rather than using the numerical score as a predictor of potency. As noted, because enol tautomers were prevalent in the potent inhibitors, the enol structures were prioritized in docking. While differences between the docked pose of the enol and keto tautomer in most instances were subtle, with both

tautomers anchored in the CT domain active site via interaction of the terminal carboxyl moiety, the keto tautomer of 3,3'-(1,4-phenylene)bis[2-hydroxy-2-propenoic acid] (**9a**) underscores a liability of this compound's structure (Figure 4.2).

A common feature of the docked phenylpyruvic acids was coordination of the carboxyl moiety with the metal center. Because carboxylates are metal binding groups, this interaction is not surprising, and even prior to docking raised concern as a potential liability in terms of selectivity against other metalloenzymes. It is the pose of the keto tautomer of **9a** that is especially alarming.

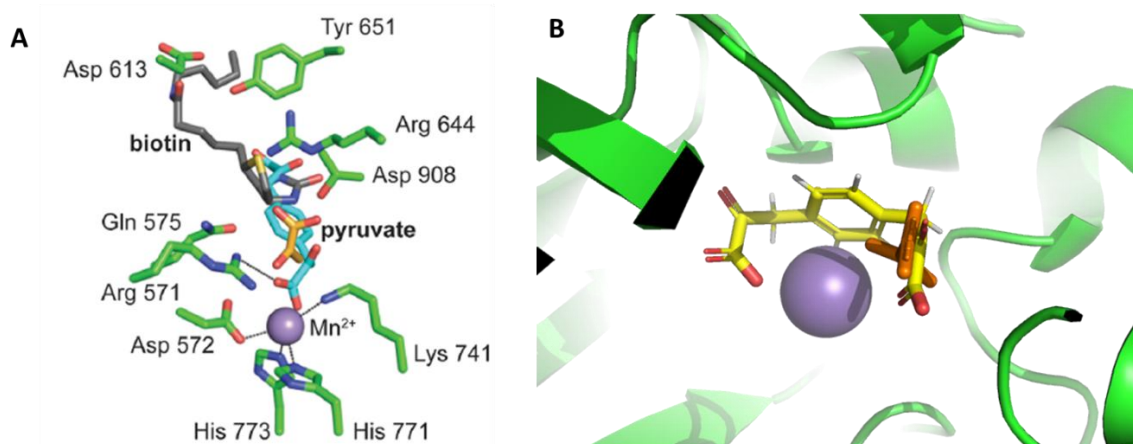


Figure 3.2 (A) 3,3'-(1,4-phenylene)bis[2-hydroxy-2-propenoic acid] (teal) docked in the active site of the CT domain in the absence of biotin. Biotin (gray) and pyruvate (orange) are shown as an overlay to demonstrate the inhibitor's occupancy of the ligand binding sites. (B) Keto tautomer of 3,3'-(1,4-phenylene)bis[2-hydroxy-2-propenoic acid] (yellow) docked in CT domain of PC with bidentate chelation of metal center with pyruvate (orange) shown as an overlay.

While **9a** demonstrated the greatest potency in the FVB assay, the incorporation of the second metal-binding carboxyl moiety introduces greater liability in terms of selectivity for PC over other metalloenzymes. While the enol tautomer of **9a**'s docked pose is analogous to other phenylpyruvic acids and of **18** (docked pose shown in Figure

4.3), which is approximately equipotent to **9a**, the bidentate chelation of the metal ion demonstrated in Figure 4.1.B demonstrates the potential for high affinity interactions with divalent metal cations in general, further validating the need for evaluation of this class of inhibitors against other metalloenzymes.

Docking of enol tautomers of **9a** and **18** (Figure 4.3) with PC in the closed conformation reveals coordination of the carboxyl moiety with the metal ion in the active site, contrasted to pyruvate's carboxyl moiety forming a salt bridge with Arg644. Consistent with previous observations of crystal structures of PC, the coordination of the inhibitor's carboxyl moiety to the metal ion active site contributes to an octahedral coordination. This coordinated carboxyl moiety of **9a** and **18** is also within hydrogen bonding distance of Arg571. Furthermore, when docked in the absence of biotin, it is predicted that the α -enolic carboxyl moiety of **9a** that is not predicted to coordinate to the metal ion and the fused quinolinyl ring of **18** occupy the biotin-binding pocket of the CT domain.⁹⁰ These docking experiments suggest the interactions of the carboxyl moiety support the emphasis on incorporation of the phenylpyruvic acid scaffold and accession of the biotin bonding pocket is a common predicted feature of the most potent inhibitors identified thus far.

4.3 Evaluation of PC Inhibitors Against Metalloenzyme Panel

Due to the liabilities introduced via incorporation of metal-binding groups, underscored by the ligand-metal interactions predicted by computational docking, evaluation of selectivity of the most potent inhibitors is essential. For clarity, the compounds evaluated for selectivity (**9a**, **9b**, **9d**, and **18**) and IC₅₀ values from the FVB assay are given in Figure 4.4.

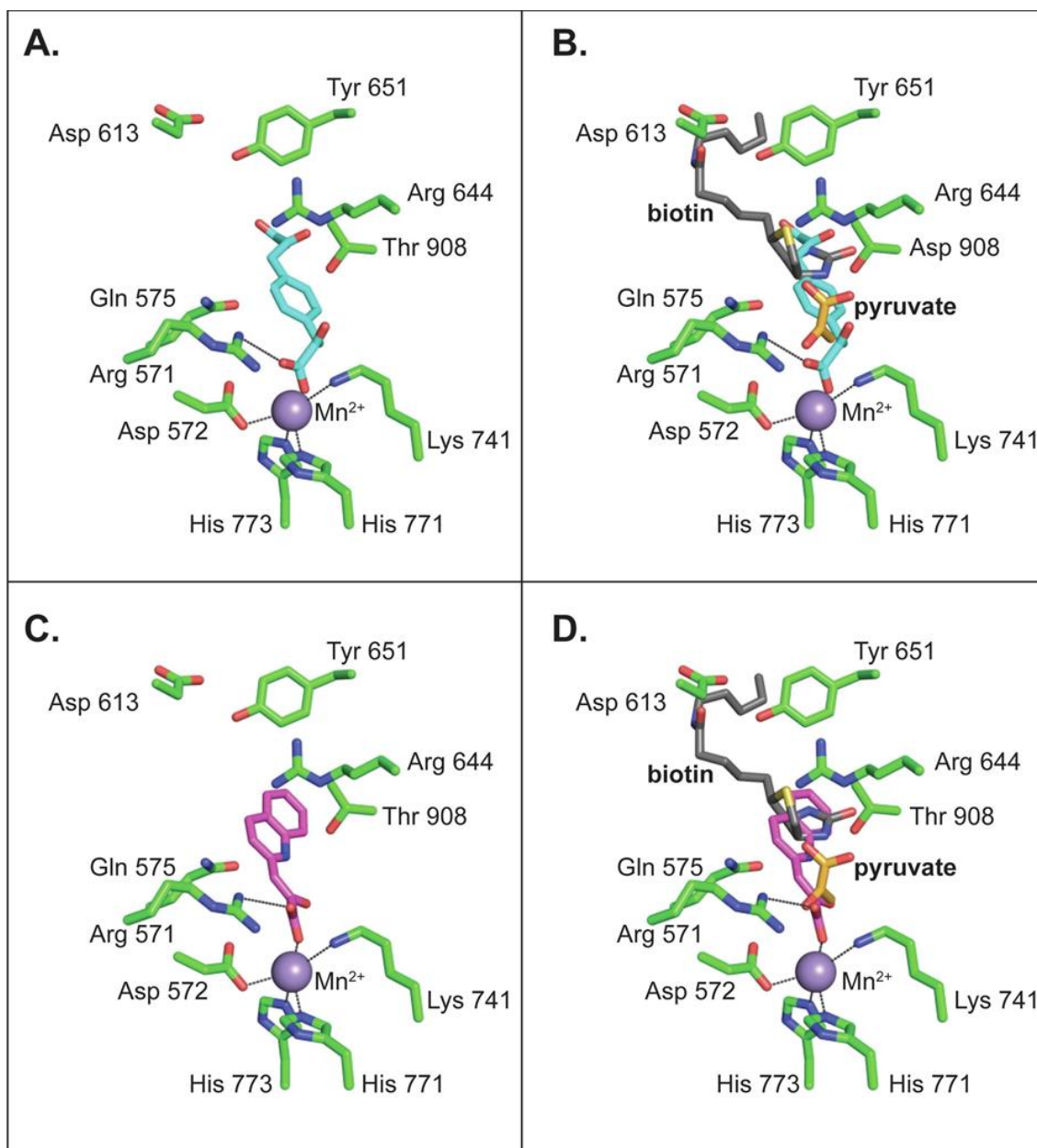


Figure 4.3 (A) Docked pose of **9a** in the closed conformation of the CT domain in the absence of biotin. (B) Docked pose of **9a** in the CT domain in the absence of biotin, with pyruvate (orange) and biotin (gray) shown as an overlay. (C) Docked pose of **18** in the closed conformation of the CT domain in the absence of biotin. (D) Docked pose of **18** in the CT domain in the absence of biotin, with pyruvate (orange) and biotin (gray) shown as an overlay.⁸⁹

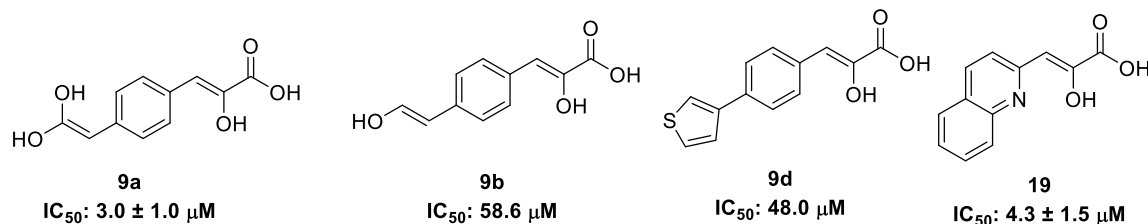


Figure 4.4 Compounds selected for evaluation for selectivity against MMP-2 and *hCAII* metalloenzymes. IC_{50} values given are obtained via the FVB assay.

For evaluation of selectivity, the compounds in Figure 4.4 were assayed against *hCAII* and MMP-2 with single-point determinations at concentrations of 200 μM and 50 μM , respectively (Figure 4.5). These concentrations are at least a full order of magnitude greater than the observed IC_{50} for the most potent compounds, **9a** and **18**. However, for compounds **9b** and **9d**, the MMP-2 concentration (50 μM) was approximately equal to the IC_{50} s observed from the FVB assay. These selectivity assays identified a major liability of **9a**, **9b**, and **9d**. Compounds **9a** and **9d** demonstrated an activating effect on *hCAII*, producing signals greater than observed in the negative control, while **9d** exhibited modest inhibition of *hCAII*. Equally important, **9a**, **9b**, and **9d** all showed significant inhibition of MMP-2 and these at concentrations near those observed for inhibition of PC. Compound **18**, however, demonstrated no significant inhibition of either *hCAII* or MMP-2. It was also established that compound **18** does not inhibit the MDH or lactate dehydrogenase (LDH) enzymes, and does not act as a substrate with LDH.⁸⁹ These data suggest that the phenylpyruvic acid scaffold, while amenable to the generation of relatively potent PC inhibitors, results in compounds lacking in selectivity. The incorporation of the quinolinyl framework of compound **18**, however, has been demonstrated as an approximately equipotent inhibitor to that of **9a**, with increased

selectivity. This heteroaromatic motif should be explored further and incorporated in subsequent generations of small molecule PC inhibitors.

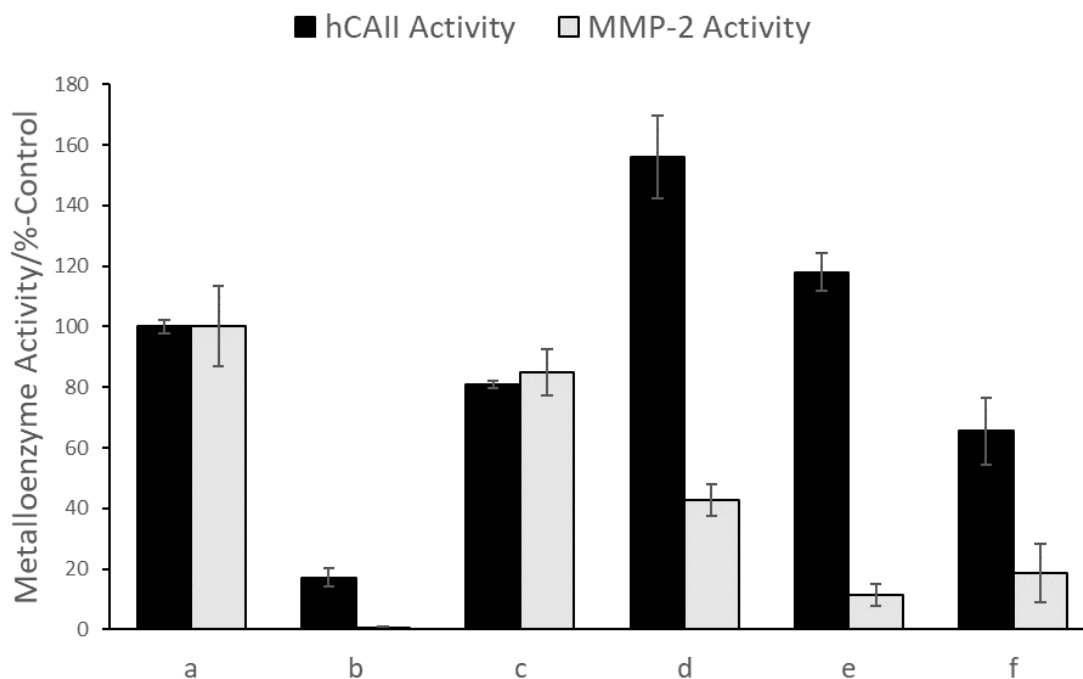


Figure 4.4 Activity of human carbonic anhydrase II (*hCAII*, black bars) in the presence of compounds (200 μM) or matrix metalloproteinase-2 (*MMP-2*, gray bars) in the presence of compounds (50 μM). (a) Negative control, (b) known inhibitor (acetazolamide, 5 μM for *hCAII*; PD166793, 100 μM for *MMP-2*) (c) **18**, (d) **9a**, (e) **9b**, (f) **9d**. Error bars represent standard error of the mean for four determinations each.

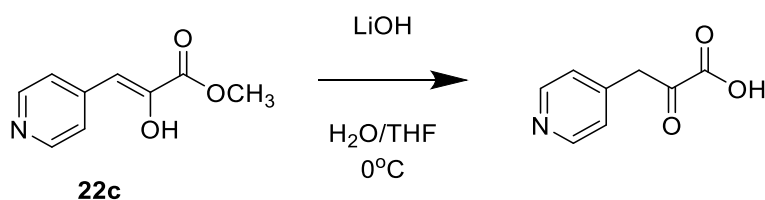
Computational docking, selectivity assays, and kinetic analysis to determine mode of inhibition serve as important hallmarks in characterization of the discovered inhibitors of PC. In addition to the confidence of inhibitory concentrations by employing the MDH assay as a secondary assay, computational docking helped to identify key interactions of the inhibitors in the CT domain active site. While occupancy of the biotin-binding domain was common amongst the two most potent inhibitors characterized to date, **9a**

and **18**, the most common feature of the inhibitors identified in docking was a tight interaction between the terminal metal-binding carboxyl group and the metal ion in the active site. The validity of these docked poses is strengthened by the evidence that the inhibitors are, in fact, competitive with respect to pyruvate and that they selectively target the CT domain. Investigation of the liability of the incorporation of metal-binding groups via the selectivity assays with *hCAII* and MMP-2 revealed that, except for the heteroaromatic inhibitor **18**, the inhibitors described lack selectivity for PC. The improved potency of the described inhibitors over previously reported inhibitors of PC, taken together with the initial promising selectivity data for **18**, marks an important step forward in the generation of small molecule inhibitors useful for probing PC's metabolic role in implicated diseases like type 2 diabetes and certain cancers. Further development of inhibitors should be pursued, leading to the identification of a class of potent and selective inhibitors of PC.

CHAPTER 5 Future Directions

5.1 Exploration of Heteroaromatic α -Hydroxycinnamates

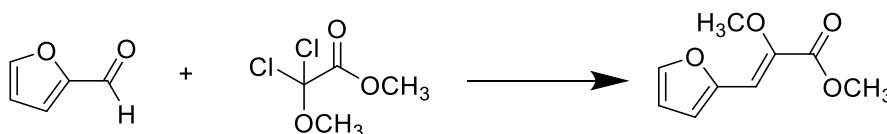
While phenylpyruvic acids represent a range of potency against *Sa*PC with **9a** exhibiting the greatest inhibitory activity, the increased selectivity and equipotency of **18** suggests exploration of heteroaromatic α -hydroxycinnamates. Literature precedent exists for the generation of heteroaromatic α -hydroxycinnamates or the related α -methoxyacrylates.^{93,94} Hydrolysis of **22c** to generate 2-oxo-3-(pyridin-4-yl)propanoic acid is reported (Scheme 5.1).⁹³ Attempts to replicate this result were unsuccessful. Identification of a method to isolate this compound would represent an important step forward in evaluating heteroaromatic α -hydroxycinnamates that are less sterically bulky than the lead compound **18**. If nitrogen is a requirement of the heteroaromatic system to achieve selectivity for PC, isolation of these compounds is essential for development of subsequent generations of PC inhibitors.



Scheme 5.1 Generation of 2-oxo-3-(pyridin-4-yl)propanoic acid.⁹³

While evaluation of nitrogen-containing heteroaromatic α -hydroxycinnamates are a logical class of compounds to pursue, incorporation of additional heterocycles containing nitrogen represent a class of compounds that has yet to be explored. While the

furanyl-derived propenoic acid is reportedly difficult to isolate and is prone to decomposition, generation of the α -methoxyacrylate is achievable in yields of up to 69%. Generation of such a methyl ester relies upon a chromium(II)-catalyzed condensation (Scheme 5.2).⁹⁴



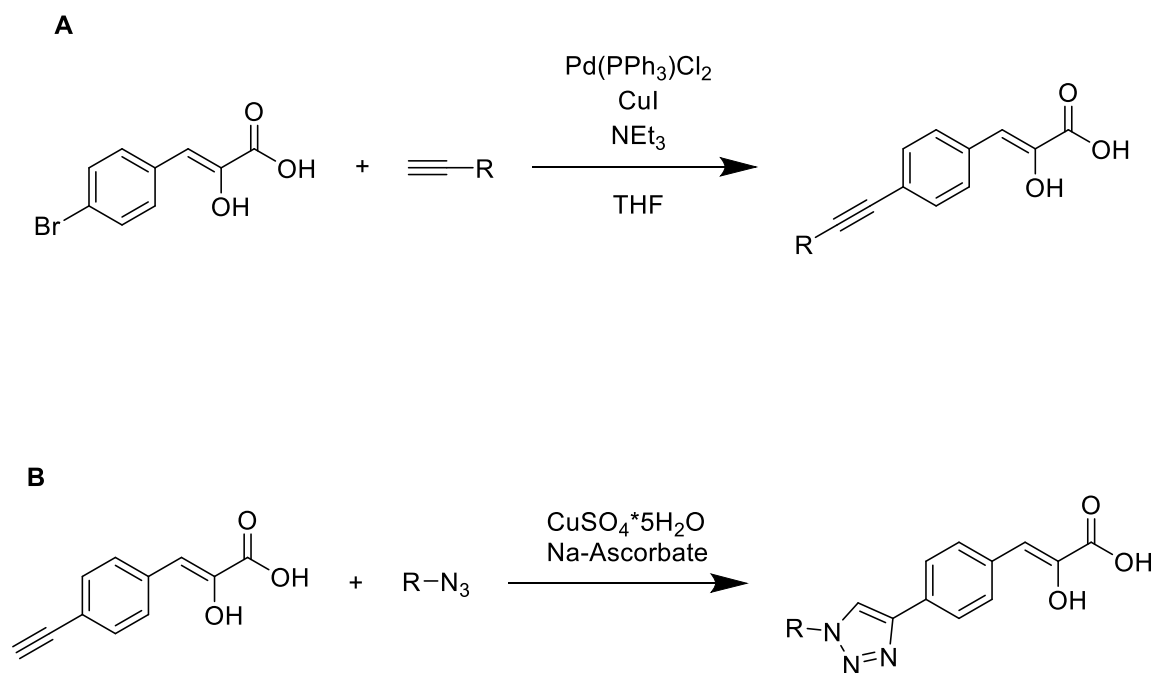
Scheme 5.2 Generation of 3-(2-furanyl)-2-methoxy-2-propenoic acid methyl ester.⁹⁴

While these conditions are primarily reported for the generation of phenyl-derived α -methoxyacrylates, exploration of these methods to generate α -methoxyacrylates derived from other heteroaromatic aldehydes containing pyridines and thiophenes represents a potential route to generate the desired heteroaromatic α -hydroxycinnamates.

5.2 Further Utility of Sonogashira Reactions

Based on computational docking, compounds **9a** and **18** both access the biotin binding pocket of the CT domain active site. The Sonogashira coupling described earlier is aptly suited for appending scaffolds in the para position of phenylpyruvic acid to generate a range of compounds that access the biotin binding site. This methodology could employ a range of commercially available or prepared terminal alkynes. Furthermore, the installation of a free alkyne, such as in **9e** opens up the possibility for the development of a range of compounds generated via alkyne-azide click chemistry (Scheme 5.3). While the other compounds derived from phenylpyruvic acid exhibited

liabilities in terms of selectivity, data regarding potency of these compounds would be useful in designing an inhibitor that incorporates key features determined for potency combined with features determined to be necessary for the development of selective inhibitors against *SaPC*.



Scheme 5.3 (A) Proposed scheme for the generation of compounds via Sonogashira coupling. (B) Generation of triazole compounds via click reaction sequence.

Buoyed by evidence that the evaluated inhibitors target the CT domain, computational docking should be employed to prioritize ligand design. Still, even with the aid of docked structures, much of the information used to predict potency and selectivity is speculative. Attempts to crystallize PC with an inhibitor bound are ongoing, and the solution of such a crystal structure will help clarify priorities in terms of compound synthesis. As the library of compounds is expanded, it is important to continue

to develop tools for biological evaluation. While potency and selectivity have been the focus of this project thus far, these are not the only important indicators of viable inhibitors.

5.3 Evaluation of Cell Permeability

Pyruvate carboxylase is located within the mitochondria.¹ As such, an effective inhibitor must have sufficient permeability to pass through a cell membrane. While there are *in silico* simulation methods to calculate a permeability coefficient, these simulated values, however, are often off by several orders of magnitude,⁹⁵ which underscores the need for reliable *in vitro* evaluation of cell permeability.

Methods for *in vitro* evaluation of cell permeability have been developed and are widely used in academia and the pharmaceutical industry. Two common methods are the Caco-2 assay, which is a cell-based assay in which a monolayer of colorectal carcinoma cells is employed due to their morphological similarity to small intestinal epithelial cells⁹⁶ and the closely related Madin-Darby Canine Kidney (MDCK) cell-based assay.⁹⁷ While effective, these methods do require up to three weeks of rigorously controlled contamination-free growth of the cell lines, and the systems include endogenous transporter and efflux systems, which can actively work against passive cell membrane permeation, complicating the data obtained from these assays.⁹⁸

The Caco-2 permeability assay is performed by growing a monolayer of Caco-2 cells in multiwell plates. Once the monolayers are grown, the test or control compounds are applied to each well, and monitored over a timeframe of two hours. Concentrations are measured via liquid chromatography mass spectrometry (LC-MS), and the apparent

permeability coefficient (P_{app}) is determined according to the equation:

$$P_{app} = \left(\frac{\frac{dQ}{dt}}{C_0 \times A} \right)$$

In this equation, dQ/dt is the rate of permeation across the monolayer, C_0 is the concentration of the test compound at time zero, and A is the area of the monolayer. Control compounds atenolol, with a human absorption of 50%⁹⁹, and propranolol, with a human absorption of 90%¹⁰⁰, can be used as controls to evaluate relative permeability based on obtained P_{app} values.

Evaluation of cell permeability is critical for the development of PC inhibitors. Despite identifying the most potent small molecule inhibitors of pyruvate carboxylase to date, potency has not been evaluated in the context of cellular systems. If the necessary pharmacophoric motif of the phenylpyruvic acid scaffold precludes cell membrane permeability, these permeability assays will reveal the necessity of the development of alternative pharmacophores.

The work presented in this thesis represents a promising start toward the development of potent small molecule inhibitors of pyruvate carboxylase. Development of good probes of PC will be essential in evaluating the enzyme's role in several metabolic disorders. Thus far, the major liability the described inhibitors carry is a lack of selectivity. While plenty inspiration exists for development of subsequent generations of small molecule inhibitors, it is important to further the biological evaluation of these

compounds in anticipation of additional liabilities these compounds carry. Still, α -hydroxycinnamic acids represent the most potent small molecule inhibitors of PC to date, and provide important insight into the development of probes that will be useful in further understanding of the important metabolic enzyme PC.

CHAPTER 6 Methods and Characterization

6.1 Enzyme Inhibition Assays

6.1.A. Screening Compounds for Inhibition Using Fast Violet B

Compounds were initially screened for inhibition of *S. aureus* PC (*SaPC*) with an optimized assay that is based on the reaction of OAA, the product of the PC-catalyzed reaction with Fast Violet B, a diazonium salt which produces a colored adduct with an absorbance maximum at 530 nm.⁶ The published 96-well plate procedure was modified to a 384-well plate format such that all of the steps were identical except that the volumes were decreased by half to a final assay volume of 60 μ L. Assay conditions consisted of 50 mM Bis-Tris (pH 7.7), 3mM MgCl₂, 150 mM KCl, 1% DMSO, and 0.5% Triton x-100. To determine whether the compounds interfered with formation of the FVB-OAA colored adduct itself, the procedure was modified slightly: 15 μ L of OAA was added to a final concentration of 200 μ M in place of 15 μ L enzyme. This functioned to assess for possible interference of the compounds with the formation of the FVB-OAA adduct. None of the described compounds interfered with the FVB assay signal at 200 μ M.

6.1.B. Measurement of OAA Formation With Malate Dehydrogenase

Malate dehydrogenase coupled enzyme assays were performed at 22°C in a 96-well plate format for a total reaction volume of 200 μ L. Assay conditions consisted of 100 mM Tris (pH 7.8), 7 mM MgCl₂, 150 mM KCl, and 0.5% Triton x-100. First, 20 μ L PC was added such that the final concentration in the assay was 10 μ g/mL. Subsequently, 20 μ L of compound was added to obtain the desired final concentration, 20 μ L of MDH

was added such that the final concentration in the assay was 20 U/mL, and lastly 140 μL of substrates were added to initiate the reaction (pyruvate, HCO_3^- , ATP, and NADH to a final assay concentration of 25 mM, 2.5 mM, and 0.25 mM, respectively). To assess the inhibition with respect to ATP, the procedure was modified such that 20 μM of ATP was added to the desired final concentrations prior to the addition of 120 μL of substrates to initiate the reaction (HCO_3^- , ATP, and NADH to a final assay concentration of 25 mM, 12 mM, and 0.25 mM, respectively). To account for possible compound inhibition of MDH, the procedure was modified such that 20 μL OAA was added to a final concentration of 30 mM, in place of PC. Reagents were dispensed manually by a hand-held multi-channel micropipette and absorbance measurements were recorded at 340 nm with a Multiskan Ascent spectrophotometer (Thermo).

6.1.C Evaluation Against Human Carbonic Anhydrase (*hCAII*)

Assays for human carbonic anhydrase activity were performed in a 96-well plate format for a total reaction volume of 100 μL , in an assay modified from Day and Cohen.⁸ All assay reagents and solutions were prepared separately and maintained at 22°C until warmed to 30°C. All substrates, effectors, and enzyme were freshly dissolved and diluted in assay buffer containing 50 mM Tris (pH 8.0). The final concentration of the human carbonic anhydrase II enzyme was 200 nM. Where noted, acetazolamide was included at a final concentration of 10 μM . The substrate, *p*-nitrophenyl acetate, was added at a final concentration of 504 μM . For all experiments, 20 μL of enzyme stock solution was added to each well in a 96-well, flat-bottom, polystyrene microplate (Santa Cruz Biotechnology) followed by the addition of 10 μL of the effectors (assay buffer for the

uninhibited reaction, acetazolamide for inhibition). The 96-well plate was then incubated in a plate reader at 30°C for 10 min; concurrently, the substrate solution was also warmed to 30°C for 10 min. The enzymatic reaction was initiated by adding 70 μ L of the substrate solution (*p*-nitrophenyl acetate). The absorbance values were then measured at 405 nm every 30 s over a period of 20 min for a total of 40 measurements.

6.1.D. Evaluation Against Matrix Metalloproteinase-2 (MMP-2)

Assays for human matrix metalloproteinase-2 activity were performed in a 96-well plate format for a total reaction volume of 100 μ L, in an assay modified from Day and Cohen.⁸ All assay reagents were prepared and maintained at 22°C until warmed to 37°C. The omniMMP fluorogenic substrate and MMP-2 enzyme were prepared in assay buffer (50 mM HEPES, 10 mM CaCl₂, 0.05% Brij-35, pH of 7.52) and small molecule effectors were prepared as a solution in 50% DMSO, 50% assay buffer. The final concentration of enzyme in the 100 μ L enzymatic reaction was 0.0083 U/ μ L. A known inhibitor, *N*-[(4'-bromo[1,1'-biphenyl]-4-yl)sulfonyl]-L-valine (PD166793), was included where noted at a final concentration of 100 μ M. OmniMMP fluorogenic substrate was added to the 100 μ L enzymatic reaction at a final concentration of 4 μ M. For all experiments, 30 μ L of enzyme stock solution was added to each well in a 96-well, flat-bottom, black polystyrene microplate (SantaCruz Biotechnology), followed by the addition of 10 μ L of the effectors (50% assay buffer, 50% DMSO for the uninhibited reaction, PD166793 for inhibition). The 96-well plate was then incubated in a plate reader at 37°C for 30 min; concurrently the substrate solution was also warmed to 37°C for 30 min. The enzymatic reaction was initiated by adding 60 μ L of the omniMMP

fluorogenic substrate solution. The change in fluorescence was then monitored for 30 min with excitation and emission wavelengths at 320 and 400 nm, respectively, every 46 s for a total of 40 measurements.

6.2. Computational Docking

The ligand structures were built using ChemDraw (PerkinElmer) and saved as MDL Molefiles. The docking studies were performed using the docking program FITTED within the web-based FORECASTER platform, using the workflow “Docking-2D Molecules to a Rigid Protein (pdb)” which converts the 2D MDL Molefile to a 3D molecule and the protein pdb file (pdb code 3BG5) to a mol2 file. Protein Rotamer Elaboration and Protonation based on Accurate Residue Energy, or PREPARE< was utilized as part of the FITTED workflow. This software prepared all the atom files from the pdb files for suitable mol2 files. In addition to preparing the pdb files, PREPARE identified pyruvate in the pdb file by the residue name (PYR), chain location (A for open or C for closed conformation), and residue number (2001). The protein (as a mol2 file) was subsequently processed by PROtein Conformational Ensemble System Setup, or PROCESS, in the FITTED workflow to dock the 3D compounds in the binding site of the CT domain. The center of the binding site was defined by the center of pyruvate present in the active site. After the removal of pyruvate from the active site, a sphere with a radius of 15 Å was applied as the default for establishing the binding site cavity. FITTED utilized a genetic algorithm/hybrid matching algorithm to dock the compounds within the established cavity site. Docking scores were reported from FITTED as the predicted binding energy (ΔG) and, following computational docking, the lowest energy pose was visualized in Pymol.

6.3. Chemistry

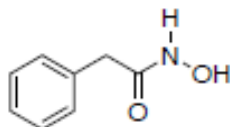
6.3.A. General Experimental

All reactions involving moisture or air sensitive reagents were carried out under a nitrogen atmosphere in oven-dried glassware with anhydrous solvents. THF and ether were distilled from sodium/benzophenone. Purifications by chromatography were carried out using flash silica gel (32-64 μ). NMR spectra were recorded on either a Varian Mercury + 300 MHz or a Varian UnityInova 400 MHz instrument. CDCl_3 and d_6 -DMSO were purchased from Cambridge Isotope Laboratories. ^1H NMR spectra were calibrated to 7.27 ppm for residual CHCl_3 or 2.50 ppm for d_5 -DMSO. ^{13}C NMR spectra were calibrated from the central peak at 77.23 ppm for CDCl_3 or 39.52 ppm for d_6 -DMSO. Coupling constants are reported in Hz. Elemental analyses were obtained from Midwest Microlabs, Ltd., Indianapolis, IN, and high-resolution mass spectra were obtained from the COSMIC lab at Old Dominion University.

General Procedure for Synthesis of Hydroxamic Acids (1a-c)

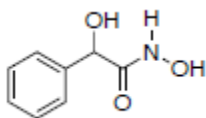
With gentle heating, hydroxylamine hydrochloride (0.42 g, 6.0 mmol) was dissolved in EtOH (11 mL). Separately, a solution of KOH (0.50 g, 8.9 mmol) in EtOH (4 mL) was prepared, and added to the hydroxylamine hydrochloride solution, and stirred (10 min). Upon cooling of this solution in an ice bath to allow for precipitation of KCl, the solution was filtered into a flask containing the appropriate methyl ester, and stirred for 16 h at room temperature. The reaction was then quenched with MeOH, concentrated HCl added dropwise, inducing the formation of a white precipitate. This solution was filtered, and the filtrate extracted with dichloromethane (4 x 10 mL), the organic layer

dried (MgSO_4), and concentrated to give the product as a solid.



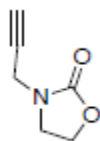
N-hydroxy-2-phenylacetamide (**1a**)

From methyl phenyl acetate (0.420 g, 2.80 mmol), **1a** was collected as a white solid (20.3 mg, 6.5%). mp = 142-145°C (lit.¹⁰¹ mp = 143-145°C); ^1H NMR (300 MHz, d_6 -DMSO): δ 10.64 (s, 1H), 8.80 (s, 1H), 7.37-7.17 (m, 5H), 3.25 (s, 2H). ^{13}C NMR (100 MHz, d_6 -DMSO): δ 170.0, 132.7, 129.6, 128.9, 127.2, 40.4 ppm.



N,2-dihydroxy-2-phenylacetamide (**1b**)

From methyl mandelate (499 mg, 3.0 mmol), **1b** was collected as a white solid (37 mg, 7.1%). mp = 141-143°C (lit.¹⁰² mp = 138-139°C); ^1H NMR (300 MHz, d_6 -DMSO) δ 10.75 (s, 1H), 8.78 (s, 1H), 7.50-7.20 (m, 5H), 5.97 (s, 1H), 4.87 (s, 1H), 3.58 (s, 1H) ^{13}C NMR (100 MHz, d_6 -DMSO): δ 168.9, 140.7, 128.1, 128.0, 126.7, 73.4 ppm.



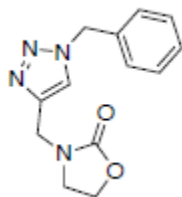
***N*-Propargyl-2-oxazolidinone (2a)**

2-Oxazolidinone (100 mg, 1.1 mmol), propargyl bromide (120 mg, 1.00 mmol), potassium carbonate (492 mg, 3.60 mmol), and TBAI (21 mg, 0.05 mmol) were added to acetone, which was heated to reflux to give a murky yellow reaction mixture. After 48 h, the solution faded to a murky off-white color, was removed from heat, and the mixture was concentrated under reduced pressure. The off-white solid was dissolved in EtOAc, which was washed with 1 N HCl (30 mL), water (30 mL), saturated NaHCO₃ (30 mL), and brine (30 mL). The organic layer was dried (MgSO₄), and concentrated to give **2a** as a white solid (22 mg, 16%). The product was used in subsequent steps without further purification. ¹H NMR (400 MHz, CDCl₃): δ 4.26-4.26 (m, 2H), 4.04-4.01 (m, 2H), 3.63-3.59 (m, 2H), 2.58 (s, 1H); ¹³C NMR (100 MHz, CDCl₃): δ 157.8, 73.4, 62.0, 43.8, 34.2 ppm.

General Procedure for Synthesis of Triazoles Via Alkyne-Azide Click Chemistry

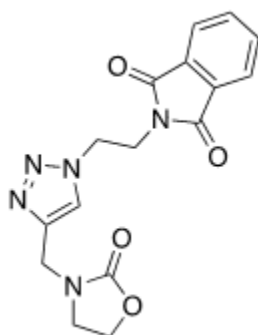
The starting alkyne was dissolved in a 1:1 mixture of *t*-BuOH:H₂O. An equimolar amount of the azide was added, followed by CuSO₄·5H₂O (10 mol%) and Na-Ascorbate (20 mol%). The resulting solution is stirred for 24 h at rt, and was subsequently quenched

with an equal volume of saturated aqueous sodium chloride solution, and extracted with EtOAc (3 x 5 mL).



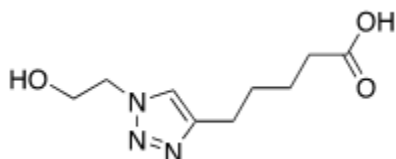
3-[(1-benzyl-1H-1,2,3-triazol-4-yl)methyl]-1,3-oxazolidin-2-one (**2b**)

From *N*-propargyl-2-oxazolidinone (51 mg, 0.41 mmol) and benzyl acide (0.05 mL, 0.41 mmol), **2b** was obtained as a white solid (67 mg, 64%). ¹H NMR (400 MHz, CDCl₃): δ 7.46 (s, 1H), 7.33-7.27 (m, 2H), 7.23-7.18 (m, 2H), 5.43 (s, 2H), 4.41 (s, 2H), 4.21 (t, *J* = 7.8 Hz, 2H), 3.56 (t, *J* = 7.8 Hz, 2H); ¹³C NMR (100 MHz, CDCl₃): δ 161.0, 158.3, 143.1, 134.4, 129.2, 128.1, 122.7, 61.7, 54.4, 44.3, 39.4 ppm.



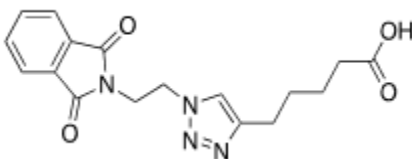
2-(2-{4-[(2-oxo-1,3-oxazolidin-3-yl)methyl]-1,2,3-triazol-1-yl}ethyl)isoindole-1,3-dione (**2c**)

From *N*-propargyl-2-oxazolidinone (19 mg, 0.15 mmol) and 2-(2-azidoethyl-2,3-dihydro-1*H*-isoindole-1,3-dione) (26 mg, 0.12 mmol), **2c** was obtained as a white solid (23 mg, 56%). ¹H NMR (400 MHz, CDCl₃): δ 7.84 – 7.48 (m, 4H), 4.61 (s, 2H), 4.43 (s, 2H), 4.33-4.19 (m, 2H), 4.09-3.98 (m, 2H), 3.64-3.47 (m, 3H); ¹³C NMR (100 MHz, CDCl₃): δ 167.9, 158.6, 144.2, 134.4, 134.1, 131.7, 123.5, 62.3, 48.4, 44.3, 39.4, 38.1 ppm.



1-(2-hydroxyethyl)-1*H*-1,2,3-triazole-4-pentanoic acid (**2d**)

From 6-heptynoic acid (0.1 mL, 0.8 mmol) and 2-azidoethanol (64 mg, 0.74 mmol), **2d** was obtained as a yellow oil after purification via column chromatography (silica gel, dichloromethane:methanol 1:1). ¹H NMR (300 MHz, *d*₆-DMSO): δ 7.77 (s, 1H), 4.45 (t, *J* = 5.3 Hz, 2H), 3.91 (t, *J* = 5.3 Hz, 2H), 2.71 (t, *J* = 7.3 Hz, 2H), 2.30, (t, *J* = 6.2 Hz, 2H), 1.77-1.56 (m, 4H); ¹³C NMR (100 MHz, *d*₆-DMSO): δ 177.2, 147.4, 122.8, 60.6, 52.5, 34.4, 28.8, 24.9, 24.6.

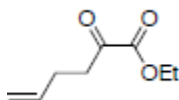


1-[2-(1,3-dihydro-1,3-dioxo-2*H*-isoindol-2-yl)]-1*H*-1,2,3-triazole-4-pentanoic acid (**2e**)

From 6-heptynoic acid (0.015 mL, 0.12 mmol) and 2-(2-azidoethyl)-2,3-dihydro-1H-isoindole-1,3-dione (22 mg, 0.10 mmol), **2e** was obtained as a white solid (23 mg, 67%).
 ^1H NMR (300 MHz, d_6 -DMSO): δ 7.88-7.72 (m, 4H), 4.90 (s, 2H), 4.67 (t, $J = 5.3$ Hz, 2H), 4.10 (t, $J = 5.3$ Hz, 2H), 2.65 (t, $J = 6.2$ Hz, 2H), 2.29 (t, $J = 6.2$ Hz, 2H), 1.70-1.53 (m, 4H); ^{13}C NMR (100 MHz, d_6 -DMSO): δ 177.9, 167.3, 148.5, 134.1, 131.7, 124.2, 123.0, 48.7, 38.1 37.5, 28.5, 24.4, 23.8 ppm.

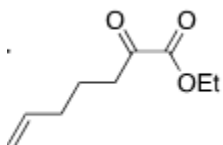
General Procedure for Grignard Synthesis of α -Keto Esters (**3a-f**)

To magnesium turnings (30 mmol), the alkyl bromide(3.0 mmol) was added dropwise as a solution of THF (10 mL) and stirred for 20 min. The resulting gray solution was added dropwise to a solution of diethyl oxalate in diethyl ether and THF (2:1, 25 mL), and cooled to -78°C in an acetone-dry ice bath, and stirred for 4 h. The reaction was then quenched with an equal volume of saturated aqueous NH_4Cl . The resulting white precipitate was removed via gravity filtration, and the filtrate extracted with EtOAc (4 x 20 mL). The organic layer was dried (MgSO_4), and concentrated to give the products. Esters furnished were used in subsequent hydrolysis without further purification.



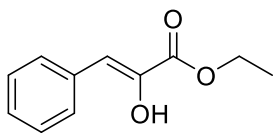
Ethyl-2-oxo-5-hexenoate (**3a**)

From 4-bromo-1-butene (408 mg, 3.0 mmol), **3a** was obtained as a yellow oil. ^1H NMR (400 MHz, CDCl_3): δ 5.82-5.69 (m, 1H), 5.04-4.92 (m, 2H), 4.28 (q, $J = 7.4$ Hz, 2H), 2.88 (t, $J = 7.2$ Hz, 2H), 2.32 (q, $J = 7.2$ Hz, 2H), 1.30 (t, $J = 7.4$ Hz, 3H); ^{13}C NMR (100 MHz, CDCl_3) δ : 193.7, 161.1, 136.0, 115.6, 62.3, 38.3, 26.9, 13.8 ppm.



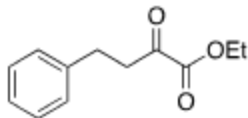
Ethyl 2-oxo-6-heptenoate (**3b**)

From 5-bromo-1-pentene (503 mg, 3.4 mmol), **3b** was collected as a yellow oil (184 mg, 32%). ^1H NMR (400 MHz, CDCl_3): δ 5.90-5.65 (m, 1H), 5.08-4.89 (m, 2H), 4.31 (q, $J = 7.4$ Hz, 2H), 2.80 (t, $J = 7.2$ Hz, 2H), 2.20-2.03 (m, 2H), 1.90 (p, $J = 7.2$ Hz, 2H), 1.34 (t, $J = 7.4$ Hz, 3H); ^{13}C NMR (100 MHz, CDCl_3) δ : 194.5, 157.5, 137.1, 115.6, 63.1, 38.2, 29.6, 26.9, 13.6 ppm.



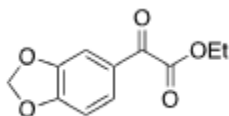
Ethyl 2-hydroxy-3-phenyl-2-propenoate (**3c**)

From benzyl bromide (502 mg, 3.0 mmol), **3c** was collected as a white solid (235 mg, 51%). ^1H NMR (400 MHz, CDCl_3): δ 7.32-7.26 (m, 1H), 7.23-7.17 (m, 2H), 7.14-7.09 (m, 2H), 6.42 (s, 1H), 4.28 (q, $J = 7.3$ Hz, 2H), 1.30 (t, $J = 7.3$ Hz, 3H); ^{13}C NMR (100 MHz, CDCl_3) δ : 191.9, 156.8, 140.7, 131.0, 127.4, 124.8, 108.0, 62.0, 12.8 ppm.



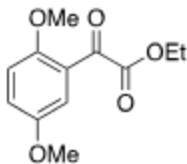
Ethyl α -oxo-benzene butanoate (**3d**)

From 2-bromoethyl benzene (932 mg, 5.00 mmol), **3d** was collected as a yellow oil (458 mg, 44%). ^1H NMR (400 MHz, CDCl_3): δ 7.15-6.98 (m, 5H), 4.17 (q, $J = 7.4$ Hz, 2H), 2.99 (t, $J = 7.4$ Hz, 2H), 2.77 (t, $J = 7.4$ Hz, 2H), 1.21 (t, $J = 7.4$ Hz, 3H); ^{13}C NMR (100 MHz, CDCl_3) δ : 193.4, 160.8, 140.1, 128.7, 128.4, 126.3, 63.1, 40.9, 29.0, 13.9 ppm.



Ethyl 3-(2H-1,3-benzodioxol-5-yl)-2-oxoacetate (**3e**)

From 5-bromomethyl-2H,1,3-benzodioxole (403 mg, 2.0 mmol), **3e** was collected as a yellow oil (97 mg, 22%). ^1H NMR (300 MHz, CDCl_3): δ 7.60 (d, $J = 8.7$ Hz, 1H), 7.47 (s, 1H), 6.88 (d, $J = 8.7$ Hz, 1H), 5.99 (s, 2H), 4.42 (q, $J = 7.6$ Hz, 2H), 1.4 (t, $J = 7.6$ Hz, 3H); ^{13}C NMR (100 MHz, CDCl_3) δ : 184.8, 164.1, 153.8, 149.1, 128.1, 127.5, 108.9, 108.5, 102.5, 62.5, 14.2 ppm.

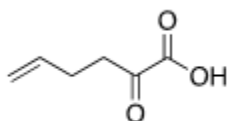


Ethyl 2-(2,5-dimethoxyphenyl)-2-oxoacetate (**3f**)

From 2-(bromomethyl)-1,4-dimethoxybenzene (500 mg, 2.30 mmol), **3f** was collected as a yellow oil (581 mg, 67%). $^1\text{H NMR}$ (400 MHz, CDCl_3): δ 7.37 (d, $J = 3.2$ Hz, 1H), 7.36-7.31 (m, 1H), 7.20-7.10 (m, 1H), 4.43-4.31 (m, 2H), 3.85 (s, 3H), 3.76 (s, 3H), 1.40 (t, $J = 7.4$ Hz, 3H) ppm.

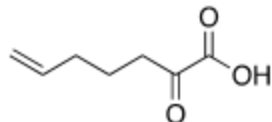
General Procedure for Hydrolysis of α -ketoesters

To compounds **3a-f**, a solution of excess 2.5 N NaOH was added. The aqueous mixture was stirred at rt until the initially emulsified mixture reached uniformity, at least 12 h. The reaction mixture was quenched with 1 N HCl, and the resulting α -keto acids were extracted several times with ether, and the combined organic layers washed with brine, dried (MgSO_4), and concentrated to give the corresponding product.



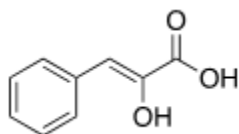
2-oxohex-5-enoic acid (**4a**)

Hydrolysis of **3a** yielded **4a** as a yellow oil (14 mg, 29%). $^1\text{H NMR}$ (400 MHz, CDCl_3) δ 5.80-5.65 (m, 1H), 5.04-4.91 (m, 2H), 2.98 (t, $J = 7.2$ Hz, 2H), 2.44-2.30 (m, 2H); $^{13}\text{C NMR}$ (100 MHz, CDCl_3) δ 195.1, 160.0, 135.8, 116.2, 36.7, 26.6 ppm.



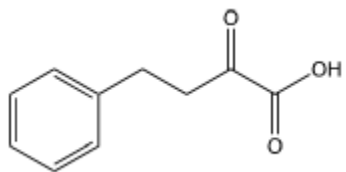
2-oxohept-6-enoic acid (4b)

Hydrolysis of **3b** yielded **4b** as a yellow oil (11 mg, 41%). ^1H NMR (300 MHz, CDCl_3): 5.79-5.61 (m, 1H), 5.03-4.91 (m, 2H), 2.88 (t, $J = 7.5$ Hz, 2H), 2.14-2.00 (m, 2H), 1.71 (p, $J = 7.5$ Hz, 2H). ^{13}C NMR (100 MHz, CDCl_3) δ 195.9, 162.6, 137.3, 116.1, 36.9, 33.0, 22.4 ppm.



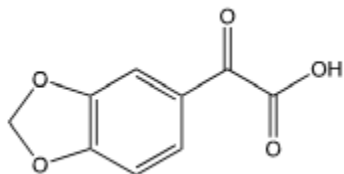
Phenylpyruvic Acid (4c)

Hydrolysis of **3c** yielded **4c** as a white solid (18 mg, 41%). mp = 146-148°C; ^1H NMR (400 MHz, d_6 -DMSO): δ 9.31 (s, 1H), 7.73 (d, $J = 7.8$ Hz, 2H), 7.32 (t, $J = 7.8$ Hz, 1H), 7.26-6.92 (m, 2H), 6.38 (s, 1H); ^{13}C NMR (100 MHz, d_6 -DMSO) δ 166.8, 142.3, 135.2, 129.7, 128.8, 127.6, 109.9 ppm.



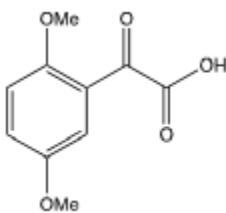
2-oxo-4-phenylbutanoic acid (4d)

Hydrolysis of **3d** yielded **4d** as a yellow oil (29 mg, 56%). ^1H NMR (400 MHz, CDCl_3): δ 7.33 – 7.17 (m, 5H), 3.21 (t, $J = 7.6$ Hz, 2H), 2.96 (t, $J = 7.6$ Hz, 2H); ^{13}C NMR (100 MHz, CDCl_3) δ 195.4, 161.1, 140.1, 128.6, 128.4, 126.4, 40.1, 29.0 ppm.



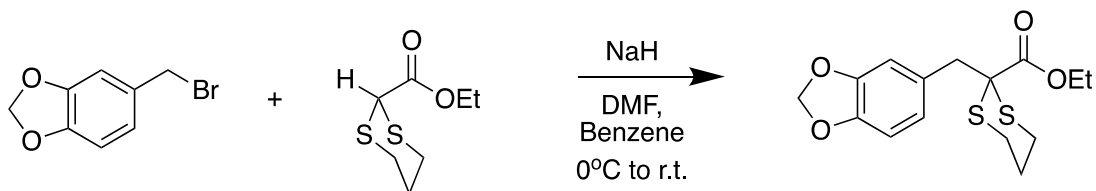
2-(2H-1,3-Benzodioxol-5-yl)-2-oxoacetic acid (4e)

Hydrolysis of **3e** yielded **4e** as a white solid (9 mg, 35%). ^1H NMR (400 MHz, CDCl_3): δ 7.72-7.67 (m, 1H), 7.22-7.17 (m, 1H), 6.85 (d, $J = 8.4$ Hz, 1H), 6.04 (s, 2H); ^{13}C NMR (100 MHz, CDCl_3) δ 182.3, 161.6, 154.9, 148.8, 130.1, 126.5, 110.3, 108.3, 102.2 ppm.



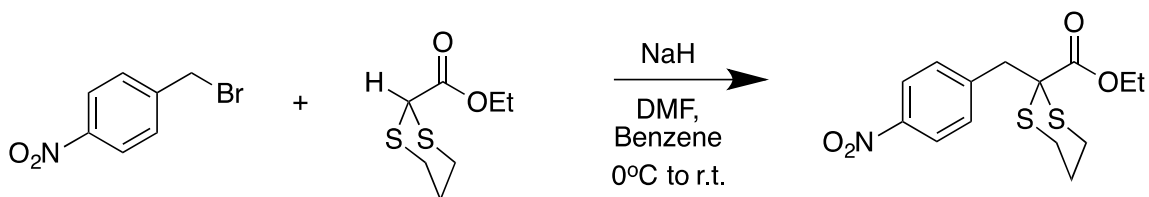
2-(2,5-Dimethoxyphenyl)-2-oxoacetic acid (4f)

Hydrolysis of **3f** yielded **4f** as a yellow solid (318 mg, 94%). ^1H NMR (300 MHz, CDCl_3): δ 7.38 (d, $J = 3.2$ Hz, 1H), 7.27-7.11 (m, 1H), 6.98 (d, $J = 9.1$ Hz, 1H), 3.91-3.77 (m, 6H); ^{13}C NMR (100 MHz, CDCl_3) δ 185.6, 169.2, 155.6, 154.3, 124.8, 122.5, 114.5, 112.8, 57.0, 56.1 ppm.



Ethyl 2-(1,3-benzodioxole)-1,3-dithiane-2-carboxylate (5a)

To a vigorously stirred suspension of sodium hydride (50 mg, 60% in paraffin oil, 1.1 mmol) in benzene (7.5 mL), at 0°C was added dropwise a solution of 5-bromomethyl-1,3-benzodioxole (218 mg, 1.01 mmol) and ethyl 1,3-dithiane-2-carboxylate (210 mg, 1.09 mmol) in DMF (2.5 mL). The resulting pale yellow solution was stirred at 0°C for 1 h. During this time, the reaction mixture became deep orange in color. The mixture was allowed to warm to room temperature, and stirred for an additional 16 h, returning to a pale yellow reaction mixture. The mixture was washed with water (3 x 20 mL), and the organic layer dried (MgSO₄), filtered, and concentrated to give the product as a pale yellow oil (296 mg, 95%). The product was used in subsequent steps without purification. ¹H NMR (400 MHz, CDCl₃) δ 6.92 (d, *J* = 1.8 Hz, 1H), 6.88-6.84 (m, 1H), 6.80 (s, 1H) 5.96 (s, 2H), 4.26 (q, *J*₁ = 4.4 Hz, *J*₂ = 7.5 Hz, 2H), 3.60-3.35 (m, 2H), 3.20 (t, *J* = 13.1 Hz, 2H), 2.75 (q, *J*₁ = 3.4 Hz, *J*₂ = 4.5 Hz, 1H), 2.7 (q, *J*₁ = 3.4 Hz, *J*₂ = 4.5 Hz, 1H) 2.24-2.12 (m, 1H), 1.99-1.85 (m, 1H), 1.47-1.39 (m, 3H); ¹³C NMR (100 MHz, CDCl₃) δ 170.9, 147.2, 146.9, 132.2, 128.7, 108.4, 107.7, 100.9, 62.1, 53.8, 44.0, 28.3, 24.5, 14.1 ppm.

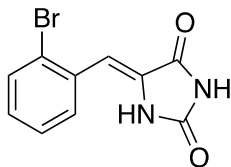


Ethyl *p*-nitro-phenyl-1,3-dithiane-2-carboxylate (5b)

To a vigorously stirred suspension of sodium hydride (44 mg, 60% in paraffin oil, 1.1 mmol) in benzene (7.5 mL), at 0°C was added dropwise a solution of 4-nitrobenzyl bromide (206 mg, 1.07 mmol) and ethyl 1,3-dithiane-2-carboxylate (257 mg, 1.19 mmol) in DMF (2.5 mL). This colorless solution stirred at 0°C for 1 h. During this time, the reaction mixture became deep orange in color. The mixture was warmed to room temperature and stirred for an additional 15 h. At this time, the mixture had become a pale yellow oil. The mixture was washed with water (3 x 20 mL), and the organic layer was dried (MgSO₄), filtered, and concentrated to give the product as a yellow oil (226 mg, 65%). ¹H NMR (400 MHz, CDCl₃) δ 8.14 (d, *J* = 8.8 Hz, 2H), 7.52 (d, *J* = 8.8 Hz, 2H), 4.28 (q, *J* = 7.2 Hz, 2H), 3.46 (s, 2H), 3.28 (t, *J* = 13.2 Hz, 2H), 2.72-2.65 (m, 2H), 2.14 (m, 1H), 1.82 (m, 1H), 1.35 (t, *J* = 7.2 Hz, 3H); ¹³C NMR (100 MHz, CDCl₃) δ 170.3, 147.2, 142.3, 131.8, 123.0, 62.3, 52.2, 44.0, 28.0, 24.1, 14.2 ppm.

General Procedure for Preparation of Substituted 5-methylenehydantoins (6a-n)

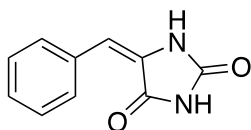
Hydantoin (500 mg, 5 mmol) was dissolved in H₂O (50 mL) at 70°C with stirring. Ethanolamine (0.61 mL) was added to the mixture, which was then heated to reflux. An equimolar quantity of the appropriate aldehyde solution (5 mmol in 5 mL ethanol) was added dropwise. The reaction mixture heated at reflux for 5 h. The mixture was cooled to room temperature, during which time the product precipitated. The precipitate was collected via vacuum filtration, washed several times with H₂O, and dried *in vacuo*.



5-[(2-Bromophenyl)methylene]-1,4-imidazolidinedione (6a)

From 2-bromobenzaldehyde (925mg, 5mmol), 233mg (17%) of product was collected.

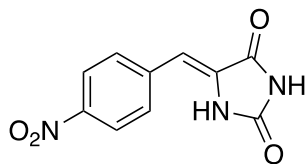
mp > 215°C ¹H NMR (400 MHz, *d*₆-DMSO) δ 7.88 (d, *J* = 7.8 Hz, 1H), 7.73-7.70 (m, 1H), 7.42-7.39 (m, 2H), 7.35 (d, *J* = 7.8 Hz, 1H), 7.21 (s, 1H); ¹³C NMR (100 MHz, *d*₆-DMSO) δ 166.0, 156.4, 133.6, 133.3, 131.0, 130.9, 130.7, 128.7, 124.7, 106.0 ppm.



5-(Phenylmethylene)-2,4-imidazolidinedione (6c)

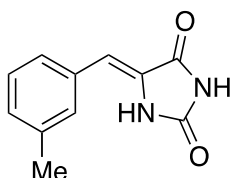
From benzaldehyde (527 mg, 4.97 mmol), 486 mg (52%) were collected as a white solid.

mp >215°C; ¹H NMR (400 MHz, *d*₆-DMSO) δ 10.83 (br s, 2H), 7.59 (d, *J* = 7.5 Hz, 2H), 7.38 (t, *J* = 7.5 Hz, 2H), 7.31 (t, *J* = 7.5 Hz, 1H), 6.40 (s, 1H); ¹³C NMR (100 MHz, *d*₆-DMSO) δ 166.0, 156.2, 133.4, 129.8, 129.2, 128.9, 128.4, 108.7 ppm.



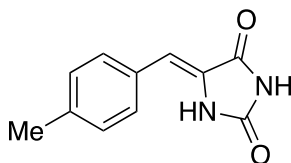
5-[(4-Nitrophenyl)methylene]-2,4-imidazolidinedione (6d)

From 4-nitrobenzaldehyde (756 mg, 5.0 mmol), 204 mg (18%) Precursor to 110 were obtained as an off-white solid. mp > 215°C; ¹H NMR (300 MHz, *d*₆-DMSO) δ 10.47 (br s, 2H), 8.19-8.10 (m, 2H), 7.87 (d, *J* = 8.7 Hz, 2H), 6.95 (s, 1H); ¹³C NMR (100 MHz, *d*₆-DMSO) δ 167.5, 162.3, 132.5, 132.0, 131.3, 125.2, 122.6, 113.2 ppm.



5-[(3-Methylphenyl)methylene]-2,4-imidazolidinedione (6e)

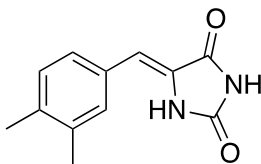
From 3-methylbenzaldehyde (601 mg, 5 mmol), 397 mg (39%) were collected as an off-white solid. mp > 215°C; ¹H NMR (300 MHz, *d*₆-DMSO): δ 10.82 (br s, 2H), 7.44 (s, 1H), 7.36 (d, *J* = 7.3 Hz, 1H), 7.26 (t, *J* = 7.3 Hz, 1H), 7.12 (d, *J* = 7.3 Hz, 1H), 6.35 (s, 1H), 2.3 (s, 3H); ¹³C NMR (100 MHz, *d*₆-DMSO) δ 161.7, 150.8, 135.6, 130.4, 128.7, 127.9, 127.3, 126.8, 123.9, 112.2, 21.2 ppm.



5-[(4-Methylphenyl)methylene]-2,4-imidazolidinedione (6f)

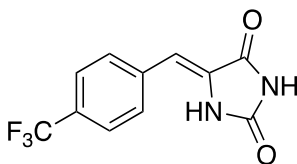
From *p*-tolualdehyde (644 mg, 5.34 mmol), 651 mg (65%), **6f** was collected as a white solid. mp > 215°C; ¹H NMR (400 MHz, *d*₆-DMSO) δ 11.08-10.47 (br s, 2H), 7.50 (d, *J* =

8.4 Hz, 2H), 7.19 (d, $J = 8.4$ Hz, 2H), 6.36 (s, 1H), 2.30 (s, 3H); ^{13}C NMR (100 MHz, d_6 -DMSO) δ 166.4, 156.3, 138.8, 130.1, 130.0, 127.9, 121.8, 109.1, 21.4 ppm.



5-(3,4-Dimethylphenyl)methylene-2,4-imidazolidinedione (6g)

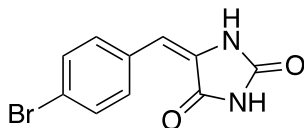
From 3,4-dimethylbenzaldehyde (671 mg, 5.0 mmol), 653 mg (60%) of product was obtained as a white solid. mp >215 °C; ^1H NMR (400 MHz, d_6 -DMSO): δ 11.08-10.47 (br s, 2H), 7.38 (s, 1H), 7.27 (d, $J = 7.9$ Hz, 1H), 7.10 (d, $J = 7.9$ Hz, 1H), 6.30 (s, 1H), 2.19 (s, 3H), 2.17 (s, 3H); ^{13}C NMR (100 MHz, d_6 -DMSO) δ 166.2, 156.1, 137.5, 137.2, 130.8, 130.4, 130.3, 127.7, 127.4, 109.2, 19.7, 19.5 ppm. Anal. Calcd. For $\text{C}_{12}\text{H}_{12}\text{N}_2\text{O}_2$: C, 66.65; H, 5.59; N, 12.93. Found: C, 66.87; H, 5.54; N, 13.10.



5-[(4-Trifluoromethylphenyl)methylene]-2,4-imidazolidinedione (6h)

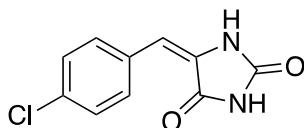
From 4-(trifluoromethyl)benzaldehyde (868 mg, 5.00 mmol), 445 mg (35%), **6h** was obtained as an off-white solid. mp > 215 °C; ^1H NMR (400 MHz, d_6 -DMSO) δ 11.44-10.39 (br s, 2H), 7.77 (d, $J = 8.2$ Hz, 2H), 7.67 (d, $J = 8.2$ Hz, 2H), 6.41 (s, 1H); ^{13}C

NMR (100 MHz, d_6 -DMSO) δ 165.9, 156.4, 137.7, 130.4, 130.2, 128.2, 125.8 (q, $^1J_{C,F}$ = 233.7 Hz), 123.3, 106.4 ppm.



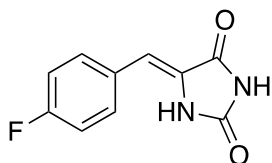
5-[(4-Bromophenyl)methylene]-2,4-imidazolidinedione (6i)

From 4-bromobenzaldehyde (920 mg, 4.97 mmol), 429 mg (32%), **6i** was collected as an off-white solid. mp $>215^\circ\text{C}$; ^1H NMR (400 MHz, d_6 -DMSO) δ 10.99–10.78 (br s, 2H), 7.56, (s, 4H), 6.36 (s, 1 H); ^{13}C NMR (100 MHz, d_6 -DMSO) δ 166.3, 156.5, 132.8, 132.1, 131.6, 129.4, 121.8, 107.0 ppm.



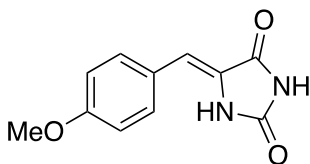
5-[(4-Chlorophenyl)methylene]-2,4-imidazolidinedione (6j)

From 4-chlorobenzaldehyde (731 mg, 5.2 mmol), 522 mg (47%), **6j** was collected as an off-white solid. mp $>215^\circ\text{C}$; ^1H NMR (400 MHz, d_6 -DMSO) δ 11.00 (br s, 2H), 7.61 (d, J = 8.1 Hz, 2H), 7.41 (d, J = 8.1 Hz, 2H), 6.38 (s, 1H); ^{13}C NMR (100 MHz, d_6 -DMSO) δ 165.9, 156.2, 133.2, 132.3, 131.5, 129.1, 129.0, 107.3 ppm.



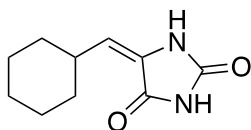
5-[(4-Fluorophenyl)methylene]-2,4-imidazolidinedione (6k)

From 4-fluorobenzaldehyde (621 mg, 5.00 mmol) 473 mg (46%) were collected as an off-white solid. ^1H NMR (400 MHz, d_6 -DMSO) δ 10.14 (br s, 2H), 7.56 (d, $J = 7.8$ Hz, 2H), 7.05 (d, $J = 7.8$ Hz, 2H), 6.27 (s, 1H); ^{13}C NMR (100 MHz, d_6 -DMSO) δ 166.5, 162.5 (d, $^1J_{\text{C,F}} = 250.4$ Hz), 156.9, 132.1, 130.3, 128.7, 116.4, 107.5 ppm.



5-[(4-Methoxyphenyl)methylene]-2,4-imidazolidinedione (6l)

From p-anisaldehyde (681mg, 5.00 mmol), 971mg (89%) of product was collected. mp > 215°C; ^1H NMR (300 MHz, d_6 -DMSO) δ 8.97 (s, 1H), 7.70 (d, $J = 8.4$ Hz, 2H), 7.10 (d, $J = 8.4$ Hz, 2H), 6.37 (s, 1H), 3.74 (s, 3H); ^{13}C NMR (100 MHz, d_6 -DMSO) δ 167.2, 163.2, 159.1, 140.5, 131.5, 125.8, 114.6, 110.2, 55.7 ppm.

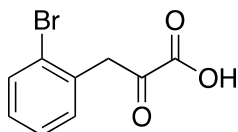


5-(Cyclohexylmethylene)-2,4-imidazolidinedione (6n)

From cyclohexanecarboxaldehyde (561 mg, 5 mmol), 554 mg (57%), **6n** was collected. mp >215°C; ¹H NMR (300 MHz, *d*₆-DMSO) δ 10.90 (s, 1H), 10.11 (s, 1H), 5.34 (d, *J* = 11.1 Hz, 1H), 2.43-2.26 (m, 1H), 1.86-1.50 (m, 5H), 1.36-0.92 (m, 5H); ¹³C NMR (100 MHz, *d*₆-DMSO) δ 165.4, 155.5, 129.6, 117.4, 35.7, 32.4, 26.0, 25.7 ppm.

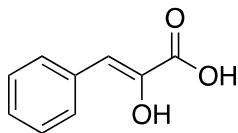
General Procedure for Hydrolysis of Benzylhydantoins

To a suspension of the benzylhydantoin in H₂O (25 mL) was added solid NaOH (15 equivalents). The mixture was heated at reflux for 12 h under an N₂ atmosphere, during which time the material went into solution. After cooling to room temperature, the stirred reaction mixture was quenched with concentrated HCl. The mixture was extracted several times with ether. The combined extracts were dried (MgSO₄) and concentrated to give the resultant acid.



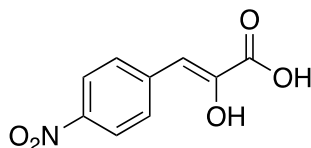
3-(2-Bromophenyl)-2-hydroxy-2-propanoic acid (**7a**)

Hydrolysis of **6a** yielded **7a** (39mg, 9%) as a yellow-orange solid. mp 157-162°C; ¹H NMR (400 MHz, *d*₆-DMSO) δ 10.29-9.23 (br s, 1H), 8.23 (d, *J* = 7.8 Hz, 1H), 7.62 (t, *J* = 8.5 Hz, 1H), 7.33-7.30 (m, 2H), 4.30 (s, 2 H); ¹³C NMR (100 MHz, *d*₆-DMSO) δ 193.0, 162.5, 134.4, 133.1, 131.1, 129.2, 128.0, 123.7, 45.6 ppm.



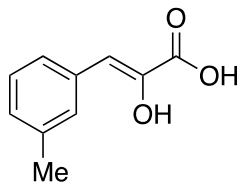
Phenylpyruvic Acid (7b)

Hydrolysis of **6b** yielded **7b** (190 mg, 48%) as a white solid. mp = 146-148°C; ^1H NMR (400 MHz, d_6 -DMSO): δ 9.31 (s, 1H), 7.73 (d, $J = 7.8$ Hz, 2H), 7.32 (t, $J = 7.8$ Hz, 1H) 7.26-6.92 (m, 2H), 6.38 (s, 1H); ^{13}C NMR (100 MHz, d_6 -DMSO) δ 166.8, 142.3, 135.2, 129.7, 128.8, 127.6, 109.9 ppm.



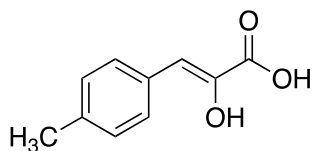
2-Hydroxy-3-(4-nitrophenyl)-2-propenoic acid (7d)

Hydrolysis of **6d** yielded **7d** (25 mg, 14%) as a reddish-brown solid. mp = 188-191°C; ^1H NMR (300 MHz, d_6 -DMSO): δ 10.59 (s, 1H), 8.22-8.05 (m, 2H), 7.96-7.79 (m, 2H), 6.96 (s, 1H); ^{13}C NMR (100 MHz, d_6 -DMSO) δ 167.4, 153.7, 145.9, 131.9, 131.4, 122.8, 113.3 ppm.



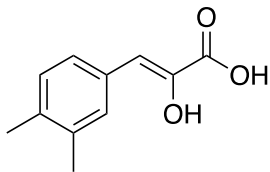
2-Hydroxy-3-(3-methylphenyl)-2-propenoic acid (7e)

Hydrolysis of **6e** yielded **7e** (156 mg, 46%) as a pale yellow oil. ^1H NMR (300 MHz, d_6 -DMSO) δ 13.11 (s, 1H), 9.19 (s, 1H), 7.57 (s, 1H), 7.53 (d, $J=7.0$ Hz, 1H), 7.21 (t, $J=7.0$ Hz, 1H), 7.03 (d, $J=7.0$ Hz, 1H), 6.35 (s, 1H), 2.27 (s, 3H); ^{13}C NMR (100 MHz, d_6 -DMSO) δ 168.6, 139.1, 135.7, 130.4, 129.5, 128.5, 127.3, 126.8, 113.9, 21.1 ppm.



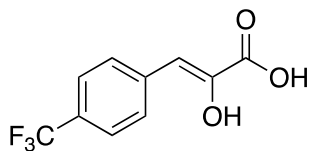
2-Hydroxy-3-(4-methylphenyl)-2-propenoic acid (7f)

Hydrolysis of **6f** yielded **7f** (159 mg, 59%) as an off-white solid. mp = 181-183°C; ^1H NMR (400 MHz, d_6 -DMSO) δ 12.87 (br s, 1H), 7.61 (d, $J = 8.1$ Hz, 2H), 7.11 (d, $J = 8.1$ Hz, 2H), 6.33 (s, 1H), 2.46 (s, 3H); ^{13}C NMR (100 MHz, d_6 -DMSO) δ 167.1, 141.9, 137.4, 132.5, 129.9, 129.6, 110.6, 21.5 ppm.



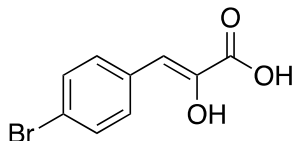
3-(3,4-Dimethylphenyl)-2-hydroxy-2-propenoic acid (**7g**)

Hydrolysis of **6f** yielded **7g** (206 mg, 55%) as an orange solid. mp = 145-146°C; ^1H NMR (400 MHz, d_6 -DMSO) δ 9.90 (s, 1H), 7.60 (d, $J = 7.6$ Hz, 2H), 7.33 (d, $J = 7.6$ Hz, 2H), 6.64 (s, 1H), 2.23 (s, 3H), 2.18 (s, 3H); ^{13}C NMR (100 MHz, d_6 -DMSO) δ 167.0, 141.4, 136.4, 136.0, 132.9, 130.8, 129.9, 127.4, 110.4, 19.9, 19.7 ppm. HRMS (FAB): M + Na⁺, found 215.0675. C₁₁H₁₂O₃ requires 215.0678.



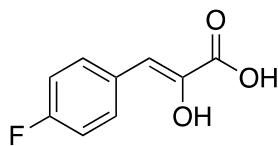
2-Hydroxy-3-(4-trifluoromethylphenyl)-2-propenoic acid (**7h**)

Hydrolysis of **6h** yielded **7h** (100 mg, 32%) as a pale yellow solid. mp = 191-192°C; ^1H NMR (400 MHz, d_6 -DMSO) δ 9.70 (s, 1H), 7.94-7.79 (m, 2H), 7.38-7.25 (m, 2H), 6.42 (s, 1H); ^{13}C NMR (100 MHz, d_6 -DMSO) δ 167.6, 166.4, 144.2, 139.9, 130.5, 129.6 (q, $^1J_{\text{C,F}} = 276.0$ Hz), 128.8, 108.7 ppm.



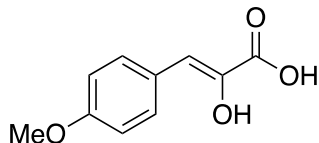
3-(4-Bromophenyl)-2-hydroxy-2-propenoic acid (**7i**)

Hydrolysis of **6i** yielded **7i** (99 mg, 27%) as a white solid. mp 194-196°C; ^1H NMR (400 MHz, d_6 -DMSO) δ 9.49 (s, 1H), 7.69 (d, $J = 8.6$ Hz, 2H), 7.51 (d, $J = 8.6$ Hz, 2H), 6.36 (s, 1H); ^{13}C NMR (100 MHz, d_6 -DMSO) δ 166.5, 143.1, 134.7, 131.7, 131.6, 120.5, 108.5 ppm. HRMS (FAB): $M + \text{Na}^+$, found 264.9470. $\text{C}_9\text{H}_7\text{O}_3\text{BrNa}$ requires 264.9471.



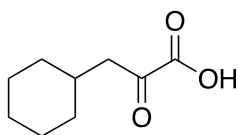
3-(4-Fluorophenyl)-2-hydroxy-2-propenoic acid (**7k**)

Hydrolysis of **6k** yielded **7k** (224 mg, 57%) as an off-white solid. mp 148-151°C; ^1H NMR (300 MHz, d_6 -DMSO) δ 9.30 (s, 1H), 7.82-7.76 (m, 1H), 7.25-7.08 (m, 3H), 6.39 (s, 1H); ^{13}C NMR (100 MHz, d_6 -DMSO) δ 167.1, 161.7 (d, $^1J_{\text{C,F}} = 245.4$ Hz), 142.1, 132.6, 131.8, 116.0, 109.3 ppm.



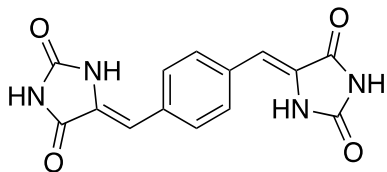
2-Hydroxy-3-(4-methoxyphenyl)-2-propenoic acid (7l)

Hydrolysis of **6l** yielded **7l** (150 mg, 28%) as a white solid. mp 166-168°C; ¹H NMR (300 MHz, *d*₆-DMSO) δ 8.95 (s, 1H), 7.70 (d, *J* = 8.3 Hz, 2H), 7.10 (d, *J* = 8.3 Hz, 2H), 6.37 (s, 1H), 4.04, (s, 3H); ¹³C NMR (100 MHz, *d*₆-DMSO) δ 159.0, 141.0, 131.5, 128.3, 125.8, 114.4, 110.8, 55.7 ppm.



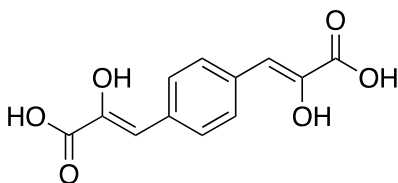
α-Oxo-cyclohexanepropanoic acid (7n)

Hydrolysis of **6n** yielded **7n** (50 mg, 11%) as a yellow solid. ¹H NMR (300 MHz, CDCl₃): δ 8.63 (s, 1H), 2.82 (d, *J* = 6.5 Hz, 2H), 2.00-1.92 (m, 1H), 1.76-1.63 (m, 4H), 1.38-0.93 (m, 5H); ¹³C NMR (100 MHz, CDCl₃) δ 195.7, 160.5, 45.0, 33.9, 33.2, 26.2, 26.1 ppm.



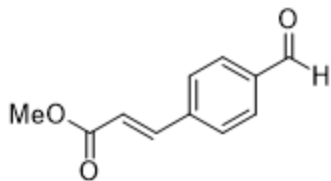
5,5'-(1,4-Phenylenedimethylidyne)bis[2,4-imidazolidinedione] (**8**)

Condensation of 1,4-benzenedicarboxaldehyde (671 mg, 5.00 mmol) by the general procedure was modified by the use of two equivalents of hydantoin (1.011 g, 10.10 mmol) to yield **8** (442 mg, 30%) as a white solid. mp > 215°C; ^1H NMR (300 MHz, d_6 -DMSO): δ 10.89 (br s, 4H), 7.63 (s, 4H), 6.40 (s, 2H) ppm.

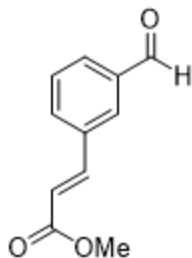


3,3'-(1,4-Phenylene)bis[2-hydroxy-2-propenoic acid] (**9a**)

Hydrolysis of **8** by the general procedure yielded **9a** (122 mg, 33%) as a dark yellow solid. mp 210°C (dec); ^1H NMR (400 MHz, d_6 -DMSO) δ 9.29 (s, 2H), 7.69 (s, 2H), 7.14 (d, $J = 8.0$ Hz, 2H), 6.35 (s, 2H); ^{13}C NMR (100 MHz, d_6 -DMSO) δ 166.7, 142.4, 134.3, 129.6, 109.8 ppm. HRMS (FAB) $M + \text{Na}^+$, found 273.0369. $\text{C}_{12}\text{H}_{10}\text{O}_6\text{Na}^+$ requires 273.0370.

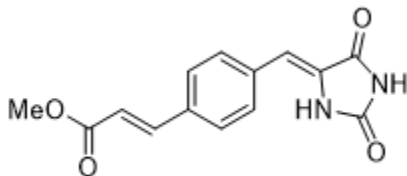
**Methyl 4'-formyl cinnamate (10a)**

To degassed N,N-dimethylacetamide (50 mL), 4-bromobenzaldehyde (928 mg, 5.01 mmol), methyl acrylate (667 mg, 7.75 mmol), tri(o-tolyl)phosphine (103 mg, 0.339 mmol), palladium acetate (28 mg, 0.12 mmol), and triethylamine (1.4 mL) were subsequently added, and the mixture was heated to 110°C for 16 h under an atmosphere of N₂. The mixture was then poured into water (50 mL), forming an off-white precipitate. The solid was removed by filtration, and the filtrate extracted with diethyl ether (3 x 20 mL). The combined organic layers were washed twice with water, once with brine, dried (MgSO₄), and concentrated to give 632 mg (67%) of the desired product as a fluffy yellow solid. mp 69-72°C; ¹H NMR (400 MHz, *d*₆-DMSO) δ 9.98 (s, 1H), 7.89 (s, 4H), 7.68 (d, *J* = 16.0 Hz, 1H), 6.76 (d, *J* = 16.0 Hz, 1H), 3.69 (s, 3H); ¹³C NMR (100 MHz, *d*₆-DMSO) δ 193.4, 166.9, 143.8, 140.2, 137.5, 130.5, 129.6, 121.5, 52.2 ppm.



Methyl 3'-formylcinnamate (**10b**)

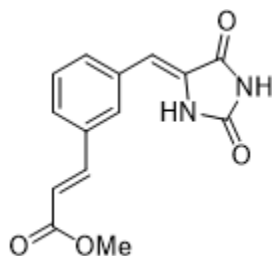
Following the procedure for **10a**, from 3-bromobenzaldehyde (922 mg, 4.98 mmol), 572 mg (60%) of **10b** was obtained as a pale yellow solid. mp 43-44°C; ^1H NMR (400 MHz, d_6 -DMSO) δ 9.99 (s, 1H), 8.20 (s, 1H), 8.01 (d, $J = 7.5$ Hz, 1H), 7.89 (d, $J = 7.5$ Hz, 1H), 7.71 (d, $J = 15.9$ Hz, 1H), 7.60 (t, $J = 7.5$ Hz, 1H), 6.73 (d, $J = 15.9$ Hz, 1H), 3.70 (s, 3H); ^{13}C NMR (100 MHz, d_6 -DMSO) δ 193.3, 166.9, 143.6, 137.1, 135.4, 134.3, 131.0, 130.2, 130.1, 120.0, 52.2 ppm.



5-(4-(2-Methoxycarbonyl)ethenylphenyl)methylene-2,4-imidazolidinedione (**11a**)

Condensation of **10a** by the general procedure gave **11a** (369 mg, 47%) as a pale yellow solid. mp > 215°C; ^1H NMR (400 MHz, d_6 -DMSO) δ 11.31 (s, 1H), 10.69 (s, 1H), 7.67 (d, $J = 8.0$ Hz, 2H), 7.61 (d, $J = 8.0$ Hz, 2H), 7.53 (d, $J = 15.4$ Hz, 1H), 6.55 (d, $J = 15.4$ Hz,

1H), 6.37 (s, 1H), 3.53 (s, 3H); ^{13}C NMR (100 MHz, d_6 -DMSO) δ 168.1, 165.9, 156.1, 143.6, 135.2, 134.4, 130.2, 129.0, 128.3, 120.1, 107.8, 57.8 ppm.



5-(3-(2-Methoxycarbonyl)ethenyl)phenyl)methylene-2,4-imidazolidinedione (**11b**)

Condensation of **10b** by the general procedure gave **11b** (409 mg, 53%) as a yellow solid.

mp 232-235°C; ^1H NMR (400 MHz, d_6 -DMSO) δ 8.27–8.14 (m, 1H), 7.84

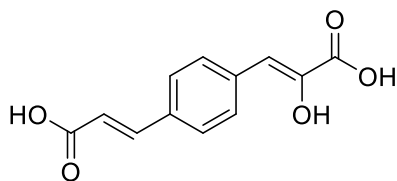
(s, 1H), 7.77 (s, 1H), 7.59 (d, $J=16.4$ Hz, 1H) 7.57–7.47 (m, 1H), 7.41 (t, $J=6.8$ Hz, 1H),

7.25 (t, $J=6.8$ Hz, 1H), 6.65 (d, $J=16.4$ Hz, 1H), 6.39 (s, 1H), 3.20 (s, 3H); ^{13}C NMR (100

MHz, d_6 -DMSO) δ 166.3, 165.8, 156.3, 139.0, 136.5, 134.0, 132.6, 129.8, 129.0, 127.2,

123.4, 121.7, 108.0, 60.3 ppm. HRMS (FAB): (M_2^+Na^+) found 567.1487.

($\text{C}_{14}\text{H}_{12}\text{N}_2\text{O}_4$) $_2\text{Na}$ requires 567.1486.



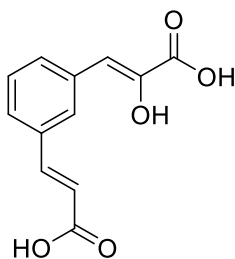
3-[4-(2-Carboxyethenyl)phenyl]-2-hydroxy-2-propenoic acid (**9b**)

Hydrolysis of **11a** by the general procedure gave **9b** (43 mg, 14%) as a mustard brown

solid. mp > 220°C; ^1H NMR (400 MHz, d_6 -DMSO) δ 9.55 (s, 1H), 7.75 (d, $J = 8.6$ Hz,

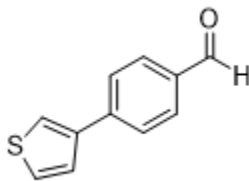
2H), 7.61 (d, $J = 8.6$ Hz, 2H), 7.24 (d, $J = 17.2$ Hz, 1H), 6.45 (d, $J = 17.2$ Hz, 1H), 6.38

(s, 1H); ^{13}C NMR (100 MHz, d_6 -DMSO) δ 168.1, 166.5, 144.0, 143.2, 137.4, 130.0, 128.7, 128.5, 119.4, 108.9 ppm. HRMS (FAB): ($\text{M} - \text{H}^+$) found 233.0453. ($\text{C}_{12}\text{H}_{10}\text{O}_5 - \text{H}^+$) requires 233.0455.



3-[3-(2-Carboxyethenyl)phenyl]-2-hydroxy-2-propenoic acid (**9b**)

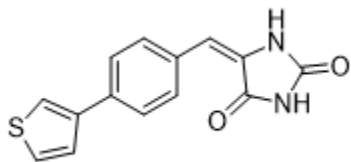
Hydrolysis of **11b** yielded **9c** (80 mg, 24%) as a yellow solid. mp 189°C (dec.); ^1H NMR (400 MHz, d_6 -DMSO) δ 9.41 (s, 1H), 7.94 (s, 1H), 7.82 (d, $J = 7.7$ Hz, 1H), 7.53 (d, $J = 8.6$ Hz, 1H) 7.50 (s, 1H), 7.36 (t, $J = 7.7$ Hz, 1H), 7.22 (d, $J = 16.1$ Hz, 1H), 6.46 (d, $J + 16.2$ Hz, 1H), 6.40 (s, 1H); ^{13}C NMR (100 MHz, d_6 -DMSO) δ 168.0, 166.6, 144.3, 143.0, 138.6, 136.2, 134.6, 131.1, 129.4, 127.1, 126.0, 119.7 ppm. HRMS (FAB): ($\text{M} + \text{Na}^+$) found 257.0421. $\text{C}_{12}\text{H}_{10}\text{O}_5\text{Na}^+$ requires 257.0420.



4-(3-Thienyl)benzaldehyde (**12**)

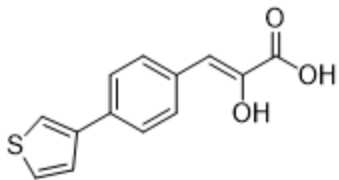
To a solution of 4-bromobenzaldehyde (1.03 g, 5.60 mmol) in a 1:1 mixture of ethanol and toluene (40 mL) was added $\text{Pd}(\text{PPh}_3)_4$ (19 mg, 0.016 mmol). The resulting clear, pale

orange solution stirred at room temperature for 15 min under an atmosphere of N₂. 3-Thienyl boronic acid (858 mg, 6.80 mmol) was subsequently added, followed by sodium bicarbonate (1.89 g, 22.5 mmol) as a solution in water (11 mL). The resulting solution was heated at reflux for 2 h. The deep red solution was filtered through Celite, and the organic layer separated, washed with brine (2 x 20 mL) and concentrated to give 540 mg (51%) of the product as an orange solid. mp 95-96°C; ¹H NMR (400 MHz, *d*₆-DMSO) δ 9.97 (s, 1H), 8.08 (s, 1H), 7.95-7.87 (m, 4H), 7.68-7.62 (m, 2H); ¹³C NMR (100 MHz, *d*₆-DMSO) δ 193.0, 141.0, 140.6, 135.2, 130.7, 128.1, 127.0, 126.8, 124.1 ppm.



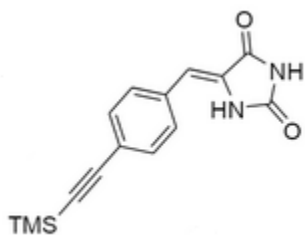
5-[4-(3-Thienyl)phenylmethylene]-2,4-imidazolidinedione (**13**)

Condensation of **12** by the general procedure gave **13** (560 mg, 78%) as a beige solid. mp > 215°C; ¹H NMR (300 MHz, *d*₆-DMSO) δ 8.28 (s, 1H), 7.93 (s, 1H), 7.76 (d, *J* = 3.9 Hz, 1H), 7.74-7.70 (m, 2H), 7.64 (s, 1H), 7.62-7.57 (m, 2H), 6.34 (s, 1H); ¹³C NMR (75 MHz, *d*₆-DMSO) δ 162.0, 157.3, 141.7, 135.6, 132.5, 130.3, 129.1, 128.1, 126.5, 122.6, 122.3, 107.9 ppm.



2-Hydroxy-3-[4-(3-thienyl)phenyl]-2-propenoic acid (**9d**)

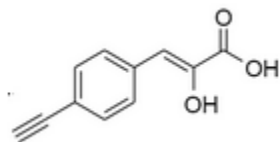
Hydrolysis of **13** yielded **9d** (49 mg, 13%) as a pale yellow solid. mp 194-196°C; ^1H NMR (400 MHz, d_6 -DMSO) δ 9.29 (s, 1H), 7.92 (q, $J = 5.5$ Hz, 1H), 7.87-7.83 (m, 1H), 7.81 (s, 1H), 7.76 (d, $J = 8.2$ Hz, 2H), 7.20 (d, $J = 8.2$ Hz, 2H), 6.39 (s, 1H) ^{13}C NMR (100 MHz, d_6 -DMSO) δ 167.0, 142.5, 141.8, 134.5, 134.4, 130.6, 127.8, 126.7, 126.6, 121.7, 110.0 ppm. HRMS (FAB): $\text{M} + \text{Na}^+$ found 269.0241. $\text{C}_{13}\text{H}_{10}\text{O}_2\text{SNa}^+$ requires 269.0243.



5-({4-[2-(Trimethylsilyl)ethynyl]phenyl}methylidene)imidazolidine-2,4-dione (**14**)

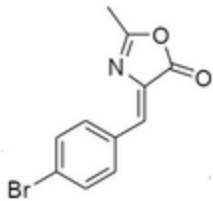
To a solution of **6i** (561 mg, 3.03 mmol), bis(triphenylphosphine) palladium (II) dichloride (47 mg, 0.070 mmol), and copper (I) iodide (26 mg, 0.14 mmol) dissolved in freshly distilled THF (15 mL) were added triethylamine (1.25 mL, 17.0 mmol) and trimethylsilylacetylene (0.44 mL, 5.7 mmol). The mixture was stirred at room temperature for 20 h. The solution was filtered through a pad of celite, and concentrated

to give a thick, oily residue, which was dissolved in chloroform (20 mL), filtered again through celite, and concentrated to give 570 mg of the crude product as a dark crystalline solid, which was purified by column chromatography (9:1 hexanes:EtOAc to 4:1 hexanes:EtOAc) to give the product (452 mg, 74%) as a white crystalline solid. mp > 215°C; ^1H NMR (400 MHz, d_6 -DMSO) δ 7.77 (d, $J = 7.6$ Hz, 2H), 7.55 (d, $J = 7.6$ Hz, 2H), 0.22 (s, 9H); ^{13}C NMR (100 MHz, d_6 -DMSO) δ 164.6, 153.8, 131.9, 131.7, 126.3, 125.3, 123.7, 111.4, 103.9, 96.8, -0.1 ppm.



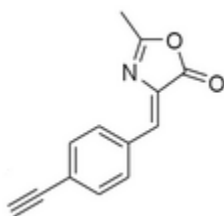
3-(4-Ethynylphenyl)-2-hydroxy-2-propenoic acid (9e)

Hydrolysis of **6i** according to the general procedure yielded **9e** (44mg, 11%) as a white solid. mp > 215°C. ^1H NMR (400 MHz, d_6 -DMSO) δ 8.74 (s, 1H), 7.56 (d, $J = 7.8$ Hz, 2H), 7.50 (d, $J = 7.8$ Hz, 2H), 6.47 (s, 1 H), 3.17 (s, 1H); ^{13}C NMR (100 MHz, d_6 -DMSO) δ 167.7, 140.3, 132.1, 131.0, 127.9, 122.8, 116.4, 80.2, 78.8 ppm.



4-[(4-Bromophenyl)methylidene]-2-methyl-4,5-dihydro-1,3-oxazol-5-one (15)

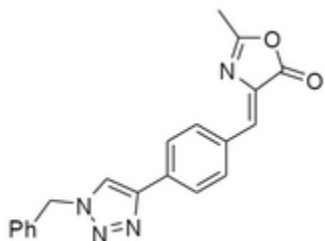
To 4-bromobenzaldehyde (931 mg, 5.03 mmol) as a solution in acetic anhydride (8 mL), N-acetyl glycine (585 mg, 5.00 mmol) and sodium acetate (410 mg, 5.00 mmol) were added, and the reaction was heated at 100°C for 4 h. Upon cooling to room temperature **15** (249 mg, 19%) precipitated as a pale yellow solid. mp 134-136°C; ¹H NMR: (400 MHz, *d*₆-DMSO) δ 8.06 (d, *J* = 8.6 Hz, 2H), 7.66 (d, *J* = 8.6 Hz, 2H), 7.16 (s, 1H), 2.34 (s, 3H); ¹³C NMR (100 MHz, *d*₆-DMSO) δ 167.7, 156.1, 134.0, 133.6, 132.7, 128.7, 125.2, 122.3, 15.9 ppm.



4-[(4-Ethynylphenyl)methylidene]-2-methyl-4,5-dihydro-1,3-oxazol-5-one (16)

To a solution of **15** (600 mg, 2.90 mmol), bis(triphenylphosphine) palladium (II) dichloride (51 mg, 0.072 mmol), and copper (I) iodide (30 mg, 0.14 mmol) dissolved in freshly distilled THF (15 mL) were added triethylamine (1.25 mL, 17.0 mmol)

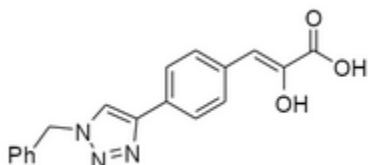
trimethylsilylacetylene (0.44 mL, 5.7 mmol). The mixture was stirred at room temperature for 20 h. The solution was filtered through a pad of celite, and concentrated to give a thick, oily residue, which was dissolved in chloroform (20 mL), filtered again through celite, and concentrated to give 430 mg of the crude product as a dark crystalline solid, which was purified by column chromatography (9:1 hexanes:EtOAc to 4:1 hexanes:EtOAc) to give **16** (200 mg, 34%) as a white crystalline solid. mp > 215°C; ¹H NMR: (400 MHz, *d*₆-DMSO) δ 8.17 (d, *J* = 6.8 Hz, 2H), 7.58 (d, *J* = 6.8 Hz, 2H), 7.16 (s, 1H), 3.70 (s, 1H), 2.47 (s, 3H); ¹³C NMR (100 MHz, *d*₆-DMSO) δ 166.2, 155.1, 134.3, 132.0, 131.4, 13.0, 126.9, 124.1, 81.1, 79.4, 14.1 ppm.



4-[[4-(1-Benzyl-1H-1,2,3-triazol-4-yl)phenyl]methylidene]-2-methyl-4,5-dihydro-1,3-oxazol-5-one (17)

To a solution of **16** (60 mg, 0.26 mmol) dissolved in DMSO (9 mL) and H₂O (1 mL) was added benzyl azide (36 mg, 0.26 mmol), copper sulfate pentahydrate (16 mg, 0.021 mmol), and sodium ascorbate (24 mg, 0.12 mmol). The solution stirred at room temperature for 24 h, and was quenched with an equal volume of water, causing precipitation of **17** (57 mg, 56%) as a pale yellow solid, which was collected by vacuum

filtration. ^1H NMR (400 MHz, d_6 -DMSO) δ 8.72 (s, 1H), 8.21 (d, $J = 8.2$ Hz, 2H), 7.93 (d, $J = 8.2$ Hz, 2H), 7.40-7.28 (m, 5H), 7.18 (s, 1H), 5.62 (s, 2H), 1.20 (s, 3H) ^{13}C NMR (100 MHz, d_6 -DMSO) δ 171.0, 168.1, 147.2, 136.1, 132.2, 129.1, 128.9, 128.6, 127.6, 127.2, 126.9, 126.8, 126.4, 121.0, 55.9, 14.2 ppm.



3-[4-(1-Benzyl-1H-1,2,3-triazol-4-yl)phenyl]-2-hydroxyprop-2-enoic acid (9f)

Hydrolysis of **17** according to the general procedure yielded **9f** (14 mg, 7%) as a pale yellow solid. mp 197-199°C. ^1H NMR (400 MHz, d_6 -DMSO) δ 9.47 (s, 1H), 8.60 (s, 1H), 7.84 (d, $J = 7.9$ Hz, 2H), 7.79 (s, 1H), 7.65 (d, $J = 7.9$ Hz, 2H), 7.39-7.26 (m, 4H), 7.21-7.16 (m, 1H), 6.39 (s, 1H), 5.61 (s, 2H); ^{13}C NMR (100 MHz, d_6 -DMSO): δ 169.4, 167.2, 146.4, 136.4, 133.6, 131.6, 130.8, 129.3, 128.6, 128.4, 127.8, 125.6, 122.4, 53.1 ppm.

References

1. Jitrapakdee, S., St. Maurice, M., Rayment, I., Cleland, W. W., Wallace, J. C., Attwood, P. V.; *Biochem. J.* **2008**; *413*, 369-387.
2. Cheng, T., Sudderth, J., Yang, C., Mullen, A.R., Jin, E.S., Mates, J. M., DeBerardinis, R. J.; *Proc. Natl. Acad. Sci. USA* **2011**; *108*, 8674-8679.
3. Kumashiro, N., Beddow, S. A., Vatner, D. F., Majumdar, S.K., Cantley, J.L., Guebre-Egziabher, F., Fat, I., Guigni, B., Jurczak, M. J., Birkenfeld, A. L., Kahn, M., Perler, B. K., Puchowicz, M. A., Manchem, V. P., Bhanot, S., Still, C. D., Gehrard, G. S., Petersen, K. F., Cline, G. W., Shulman, G. I., Samuel, V. T.; *Diabetes*. **2013**; *62*, 2183-2194.
4. Shar, J., Stoll, R., Schauer, K., Schauer, K., Loeffler, D. I. M., Eyler, E., Joseph, B., Eisenreich W., Fuchs, T.M., Goebel, W.; *J. Bactriol.* **2010**, *192*, 1774-1784.
5. Lietzan, A.D., St. Maurice, M.; *Biochem. Biophys. Res. Commun.* **2013**, *441*, 377-382.
6. Wyatt, B.N., Arnold, L., St. Maurice, M.; *Anal Biochem.* **2018**, *550*, 90-98.
7. Attwood, P.V., Cleland, W.W.; *Biochem.* **1986**, *25*, 8191-8196.
8. Day, J.A., Cohen, S.M.; *J. Med. Chem.* **2013**, *56*, 7997-8007.
9. Owen, O.E., Kalhan, S.C., Hanson, R.W.; *J. Biol. Chem.* **2002**, *277*, 30409-30412.
10. Hasan, N.M., Longacre, M.J., Stoker, S.W., Boonsaen T., Jitrapakdee, S., Kendrick, M.A., Wallace, J.C., MacDonald, M.J.; *J. Biol. Chem.* **2008**, *283*, 28048-28059.
11. Utter, M.F., Keech, D.B.; *J. Biol. Chem.* **1960**, *235*, 17-18.

12. Tong, L.; *Cell Mol Life Sci.* **2013**, *70*, 863-891.
13. Lietzan, A.D., St. Maurice, M.; *Arch Biochem. Biophys.* **2014**, *562*, 70-79.
14. Attwood, P.V., Johannssen, W., Chapman-Smith, A., Wallace, J.C.; *Biochem. J.* **1993**, *290*, 583-590.
15. St. Maurice, M., Reinhardt, L., Surinya, K.H., Attwood, P.V., Wallace, J.C., Cleland, W.W., Rayment, I.; **2007**, *317*, 1076-1079.
16. Zeczycki, T.N., Menefee, A.L., Adina-Zada, A., Jitrapakdee, S., Surinya, K.H., Wallace, J.C., Attwood, P.V., St. Maurice, M., Cleland, W. W.; *Biochemistry*, **2011**, *50*, 9724-9737.
17. Zeczycki, T. N., St. Maurice, M.; Jitrapakdee, S., Wallace, J.C., Attwood, P.V., Cleland, W. W.; *Biochemistry*, **2009**, *48*, 4305-4313.
18. Pavlova, N.N., Thompson, C.B.; *Cell Metab*, **2016**, *23*, 27-47.
19. Cheng, T., Sudderth, J., Yang, C., Mullen, A.R., Jin, E.S; Mates, J.M., DeBeradinis, R.J.; *Proc. Natl. Acad. Sci. USA*; **2011**, *108*, 8674-8679.
20. Davidson, S.M., Papagiannakopoulos, T., Olenchock, B.A., Heyman, J.E., Keibler, M.A., Luengo, A., Bauer, M.R., Jha, A.K., O'Brien, J.P., Pierce, K.A., Gui, D.Y, Sullivan, L.B., Wasylenko, T.M., Subbaraj, L., Chin, C.R., Stephanopolous, G., Mott, B.T., Jacks, T., Clish, C.B., Vander Heiden, M.G.; *Cell Metab.* **2016**, *23*, 517-528.
21. Sellers, K., Fox, M.P., Bousamra, M., Slone, S.P., Higashi, R.N., Miller, D.M., Wang, Y., Yan, J., Yuneva, M.O., Desphande, R., Lane, A.N., Fan, T.W.M.; *J. Clin. Invest.* **2015**, *125*, 687-698.

22. a) Deberadinis, R.K., Sayed, N., Dittsworth, D., Thompson, C.B.; *Curr. Opin. Genet. Dev.* **2008**, *18*, 54-61 b) Elia, I., Schmieder, R., Christen, S., Fendt, S.; *Handbook Exp. Pharmacol.* **2016**, *233*, 321-353.
23. Christen, S., Lorendeau, D., Schmieder, R., Grunewald, T.G.P., De Bock, K., Fendt, S.M.; *Cell Reports*, **2016**, *17*, 837-848.
24. Phannasil, P., Thuwajit, C., Warnnissorn, M., Wallace, J.C., MacDonald, M.J., Jitrapakdee, S.; *PLOS ONE* **2015**.
25. Laemmli, U.K.; *Nature*, *227*, 680-685.
26. Lu, X., Bennet, B., Rabinowitz, M.E., Kang, Y.; *J Biol Chem.* **2010**, *285*, 9317-9321.
27. Shinde, A., Wilmanski, T., Chen, H., Teegarden, D., Wendt, M.K.; *Breast Cancer Res.* **2018**, *76*.
28. Boyle, J.P., Thompson, T.J., Gregg, E.W., Barker, L.E., Williamson, D.F.; *Popul. Health. Metr.* **2010**, *8*, 29.
29. Hundal, R.S., Krssak, M., Dufour, S., *Diabetes*, **2000**, *49*, 2063-2069.
30. Weinberg, M.B., Utter, M.F.; *Biochem. J.* **1980**, *188*, 601-608.
31. Jitrapakdee, S., Gong, Q., MacDonald, M.J., Wallace, J.C.; *J. Biol. Chem.* **1998**, *273*, 34422-34428.
32. Bahl, J.J., Matsuda, M; DeFronzo, R.A., Bressler, R.; *Biochem Pharmacol* **1997**, *53*, 67-74.
33. Kumashiro, N., Beddow, S., Vatner, D.F., Majumdar, S.K., Cantley, J.L., Guebre-Egziabher, F., Fat, I., Guigni, B., Jurczak, M.J., Birkenfeld, A.L., Kahn, M., Perler, B.L., Puchowicz, M.A., Manchem, V.P., Bhanot, S., Still, C.D., Gerhard,

- G.S., Petersen, K.F., Cline, G., Shulan, G.I., Samuel, V.T.; *Diabetes*, **2013**, *62*, 2183-2194.
34. DeFronzo, R.A., Prato, S.D.; *J. Diabetes Complicat.* **1996**, *10*, 243-245.
35. Leahy, J.L.; *Diabetes Care*, **1990**, *13*, 992-1010.
36. Jensen, M.V., Joseph, J.W., Ilkayeva, O.; *J. Biol. Chem.* **2006**, *281*, 22342-22351.
37. Khan, A., Ling, Z.C., Landau, B.R.; *J. Biol. Chem.* **1996**, *271*, 2539-2542.
38. Xu, J., Han, J., Long, Y.S., Epstein, P.N., Liu, Y.Q.; *Diabetologia* **2008**, *51*, 2022-2030.
39. Granner, D., Pilkis, S.; *J. Biol. Chem.* **1990**, *265*, 10173-10176.
40. Hue, L.; *Diabetes Metab Rev*, **1987**, *3*, 111-126.
41. Rosetti, L., Giaccari, A., Barzilai, N., Howard, K., Sebel, G., Meizu, H.; *J. Clin. Invest.* **1993**, *92*, 1126-1134.
42. Tutwiler, G. F., Dellevigne, P.; *J. Biol. Chem.* **1979**, *254*, 2935-2941.
43. Bahl, J. J; Matsuda, M; DeFronzo, R.A; Bressler, R.; *Biochem. Pharmacol.* **1996**, *53*, 67-74.
44. Winter, A; Hoffman, A.; *Curr. Chem. Biol.* **2008**, *2*, 11-19.
45. Scrutton, M.C; Utter, M.F.; *J. Biol. Chem*, **1965**, *240*, 3488-3498.
46. Duggleby, R.G., Attwood, P.V., Wallace, J.C., Keech, D.B.; *Biochemistry*, **1982**, *21*, 3364-3370.
47. Xiang, S., Tong, L.; *Nat. Strut. Mol. Biol.* **2008**, *15*, 295-302.
48. Green, M.; *Biochem. J.* **1962**, *89*, 585-591.
49. Scrutton, M. C., Utter, M.F.; *J. Biol. Chem.* **1967**, *242*, 1723-1735.

50. Johannssen, W., Attwood, P.V., Wallace, J.C., Keech, D.B.; *Eur. J. Biochem.* **1983**, *133*, 201-206.
51. Rohde, M., Lim, F., Wallace, J.C.; *Eur. J. Biochem.* **1986**, *156*, 15-22.
52. Attwood, P.V., Mayer, F., Wallace, J.C.; *FEBS Let* **1986**, *203*, 191-196.
53. Zeczycki, T.N., St. Maurice, M., Attwood, P.V.; *TOEIJ*, **2010**, *3*, 8-26.
54. Knowles, J.R.; *Ann. Rev. Biochem.*, **1989**, *58* 195-221.
55. Ashman, L.K., Keech, D.B.; *J. Biol. Chem.* **1975**, *250*, 14-21.
56. Scrutton, M.C., Utter, M.F.; *J. Biol. Chem.* **1965**, *240* 3714.
57. McClure, W.R., Lardy, H.A., Wagner, M., Cleland, W.W.; *J. Biol. Chem.* **1971**, *246*, 3579-3583.
58. Wilkinson, J.H., Walter, S.J.; *Enzyme*, **1972**, *13* 170-176.
59. Goodall, G.J., Baldwin, G.S., Wallace, J.C., Keech, D.B.; *Biochem. J.* **1981**, *199*, 603-609.
60. Scrutton, M.C., Olmsted, M.R., Utter, M.F.; *Methods Enzymol*, **1969**, *13*, 235-249.
61. Mildvan, A.S., Scrutton, M.C., Utter, M.F.; *J. Biol. Cem.* **1966**, *241*, 3488-2498.
62. Martin-Requero, A., Ayuso, M.S., Parrilla, R.; *J. Biol. Chem.* **1986**, *246*, 114-127.
63. Martin-Requero, A., Ayuso, M.S., Parrilla, R.; *J. Biol. Chem.* **1986**, *30*, 13973-13978.
64. Ruiz-Amil, M., De Torriontegui, G., Palacian, E., Catalina, L., Losada, M.; *J. Biol. Chem.* **1965**, *240*, 3485-3492.

65. Duangpan, S., Jitrapakdee, S., Adina-Zada, A., Byrne, L., Zeczycki, T.N., St. Maurice, M., Cleland, W. W., Wallace, J.C., Attwood, P.V.; *Biochemistry*, **2010**, *49*, 3296-3304.
66. Shoshan, M.C.; *J. Bioenerg. Biomembr*, **2012**, *44*, 7-15.
67. Doedens, D., Ashmore, J.; *Biochem. Pharmacol.* **1972**, *21*, 1745-1751.
68. Dylag, N., Lis, P., Niedzwiecka, K., Ko, Y.H., Pedersen, P.L., Goffeau, A., Ulaszewski, S.; *Biochem. Biophys. Res. Commun.* **2013**, *434*, 322-327.
69. Libor, S.M., Sundaram, T.K., Scrutton, M.C.; *Biochem. J.* **1978**, *169*, 543-558.
70. Scrutton, M.C; White, M.D. *Eur. J. Biochem.* **1983**, *249*, 5405-5415.
71. Osmani, S.A., Marston, F.A., Selmes, I.P.; *Eur. J. Biochem.* **1981**, *118*, 271-278.
72. Mukhopadhyay, B., Purwantini, E., Kreder, C.L., Wolfe, R.S.; *J. Bacteriol.* **2001**, *183*, 3804-3810.
73. Cazzulo, J.J., Stoppani, A.O.; *Arch. Biochem. Biophys.* **1968**, *127*, 563-567.
74. Cyr, D.M., Egan, S.G., Brini, C.M., Tremblay, G.C.; *Biochem. Pharmacol.* **1991**, *42*, 645-654.
75. Scrutton, M.C., Fatebene, F.; *FEBS Lett.* **1976**, *62*, 220-225.
76. Osmani, S.A., Scrutton, M.C.; *FEBS Letters*, **1984**, 157-160.
77. Meldrum, N.U., Roughton, F.J.W.; *J. Physiol*, **1933**, *80*, 113-142.
78. Day, J.A., Cohen, S.M.; *J. Med. Chem*, **2013**, *56*, 7997-8007.
79. Becker, B.; *Am. J. Ophthalmol*, **1954**, *37*, 13-15.
80. Tamura, Y., Watanabe, F., Nakatani, T., Yasui, K., Fuji, M., Komurasaki, T., Tsuzuki, H., Maekawa, R., Yoshioka, T., Kawada, K., Sugita, K; Ohtani, M.; *J. Med. Chem*, **1998**, *41*, 640-649.

81. Devel, L., Rogakos, V., David, A., Makaritis, A., Beau, F., Cuniasse, P., Yiotakis, A., Dive, V.; *J. Biol. Chem.* **2006**, *281*, 11152-111560.
82. Caton, J., Ryan, M.; *Pharmacol. Res.* 2011, *63*, 114-120.
83. Jiang, J., Thyagaran-Saju, A., Krchnak, V., Jedinak, A., Sandusky, G.E., Silva, D.; *PLoS One*, **2012**, *7*, e34283.
84. Riet, B.V., Wampler, G.L., Elford, H.L.; *J. Med. Chem.* **1979**, *22*, 589-592.
85. Macritchie, J.A., Silcock, A., Willis, C.L.; *Tetrahedron: Asymmetry*, **1997**, *8*, 3895-3902.
86. Yus, M., Najera, C., Foubelo, F.; *Tetrahedron*, **2003**, *59*, 6147-6212.
87. Eliel, E.L., Hartman, A., *J. Org. Chem.* **1972**, *37*, 505-506.
88. Wen, J., Bao, Y., Nie, Q., Liu, J., Yang, J., Wang, W., Jiang, T., Fan, Y., Li, K., Wang, J., Zhao, L., Liu, D.; *Bioorg. Med. Chem. Lett.* **2016**, *26*, 4372-4376.
89. Burkett, D. J., Wyatt, B. N., Mews, M., Bautista, A., Engel, R., Dockendorff, C., Donaldson, W. A., St. Maurice, M.; *Biorg. Med. Chem.* **2019**, *27*, 4041-4047.
90. Takai, T., Senda, H., Lee, H.; *Spectroscopy Lett.* **1998**, *31*, 379-395.
91. Lietzan, A. D., St. Maurice, M.; *J. Biol. Chem.* **2013**, *288*, 19915-19925.
92. Therrien, E., Englebienne, P., Arrowsmith, A.G., Mendoza-Sanchez, R., Corbeil, C. R., Weill, N., Campagna-Slater, V., Moitessier, N.; *J. Chem Inf Model*, **2012**, *52*, 210-224.
93. Luttenberg, S., Dat Ta, T., Heyden, J., Scherkenbeck, J.; *Eur. J. Org. Chem.* **2013**, 1824-1830.
94. Baati, R., Mioskowski, C., Kashinath, D., Kodepelly, S., Lu, B., Falck, J.R.; *Tetrahedron Lett*, **2009**, *50*, 402-405.

95. Sun, R., Han Y., Swanson, J. M. J., Tan, J. S., Rose, J. P., Voth, G.A.; *J. Chem. Phys.* **2018**, *149*, 072310.
96. Karlsson, J., Artursson, P.; *Int. J. Pharm.* **1991**, *71*, 55-64.
97. Irvine, J. D., Takahashia, K., Lockhart, J., Cheong, J. W., Tolan, H., Selick, E., Grove, J.R.; *J. Pharm. Sci.* **2001**, *14*, 271-280.
98. Hopkins, A.L., Keseru, G.M., Leeson, P.D., Rees, D.C., Reynolds, C.H.; *Nat. Rev. Drug Discovery*, **2014**, *13*, 105-121.
99. Zhao, Y.H., Le, J., Abraham, M.H., Hersey, A., Eddershaw, P.J., Luscombe, C.N., Butina, D., Beck, G., Sherborne, B., Cooper, I., Platts, J.A.; *J. Pharm. Sci.* **2002**, *90*, 749-784.
100. Yazdanian, M., Glynn, S.L., Wright, J.L., Hawi, A.; *J. Pharm. Res.* **1998**, *9*, 1490-1494.
101. Cherniuskiate, D., Rousseau, J., Sackus, A., Rollin, P., Tatibouet, A.; *Eur. J. Org. Chem.* **2011**, 2293-2300.
102. Kirby, G. W., Nazeer, M.; *J. Chem. Soc. Perkin Trans.* **1993**, 1398-1402.